Doctoral Thesis

First-Principles Calculations of Energy Materials

Chang Woo Myung

Department of Chemistry

Graduate School of UNIST

2019

First-Principles Calculations
of Energy Materials

Chang Woo Myung

Department of Chemistry

Graduate School of UNIST

ULSAN NATIONAL INSTITUTE OF
SCIENCE AND TECHNOLOGY

First-Principles Calculations of Energy Materials

A thesis/dissertation
submitted to the Graduate School of UNIST
in partial fulfillment of the
requirements for the degree of
Doctor of Philosophy

Chang Woo Myung

January/5/2019

Approved by

Kwang Soo Kim

Advisor

Kwang S. Kim

ULSAN NATIONAL INSTITUTE OF
SCIENCE AND TECHNOLOGY

First-Principles Calculations of Energy Materials

Chang Woo Myung

This certifies that the thesis/dissertation of Chang Woo Myung is approved.

January/5/2019

Kwang Soo Kim

Advisor: Kwang S. Kim

Geunsik Lee

Seung Kyu Min

Noejung Park

Jun Hee Lee

Abstract

Since the advent of civilization, carbon-based fuel, which harvests energy by oxidizing carbon, has been the main strategy for energy conversion. However, the harmful byproducts of the carbon oxidation reaction such as NO_x and CO_2 gas are inevitable and are becoming a serious problem threatening the ordinary life of the human being. Thus, low-cost, efficient, and eco-friendly energy conversion is one of the key future technologies for sustainable development. In this thesis, we discuss the first-principles calculations of energy conversion materials, including lead halide perovskite(LHP) solar cell, heterogeneous single atom catalysts (SAC), and graphene/Cu single photon source using the density functional theory(DFT), wave-function theory(WFT), and many-body theory. Also we derive the solution of the nonequilibrium steady state Anderson impurity model in real frequency using the pseudo-particle (slave-boson) method by including vertex terms beyond the first-order approximation.

Solar energy that converts the photon energy into the electric current has been considered as the alternative energy harvesting to carbon fuel. In the past five years, lead halide perovskite ABX_3 (A=Cs^+, $CH_3NH_3^+$(MA), $CHN_2H_4^+$(FA), $N_2H_5^+$(HZ); B=Pb^{2+}; X=Cl^-, Br^- or I^-) solar cells(PSCs) has shown great success with the power conversion efficiency(PCE) of 23.7 % rapidly reaching the Shockley–Queisser limit ($\sim 30\%$). The recent discovery of long life-time of hot-electrons may even enable LHP solar cells to overcome the Shockley–Queisser limit. Also LHPs in low dimensions (≤ 2) can be utilized as the light emitting diodes(LED) with the wide range of wavelengths. Recent experiments have achieved the high luminescence efficiency on a par with organic LED making LHPs promising as a versatile energy material. We uncover four intriguing results of theoretical calculations of LHPs: (i) Polaronic nature of lead halide PSCs and the role of A-site cation for polaron tuning, (ii) Rashba-Dresselhaus spin-orbit effect at LHP interface with electron transport layers, (iii) Conduction band alignment mechanism of $MAPbI_3$/La-doped $BaSnO_3$(LBSO) interface, and (iv) Proton-mediated band alignment mechanism in TiO_2/$MAPbI_3$.

Generally, the electrons in crystals experience a degree of deformation of a surrounding lattice in addition to the Bloch potential because of the large polarity of the ionic crystal giving rise to polaron. There has been a critical debate on the main source of electron-phonon coupling(e-ph) being either optical or acoustic phonon in LHPs. We show that the source of e-ph coupling in LHPs is the highest LO phonon and investigate the correlation between the polaron and A-site cations. We show that the coordination of A-site cation to halides is important to determine the polaron mobility of LHPs.

The spin-orbit coupling(SOC) field, which is odd function in k(momentum) and time reversal symmetric, at the interface of hetero-structures gives rise to the Rashba-Dresselhaus(RD) splitting of the degenerate bands. We study an elusive part of LHP/graphene and LHP/ETL interfaces using DFT and *ab initio* molecular dynamics(AIMD) simulations to account for RD

spin-orbit effect. We carry out the calculations for graphene/cubic-$CsPbI_3$(001) as a prospective interface for improving carrier transport and for TiO_2/cubic-$MAPbI_3$(001) which is a well-known ETL material for PSC devices.

Anatase and rutile TiO_2 has been the most widely used electron transport layer (ETL) material in lead halide PSC devices. However, the photo-degradation of TiO_2 by ultraviolet (UV) rays gradually deteriorates the device performance. To overcome this obstacle, the development of efficient and reliable next-generation ETL substances has emerged recently. Metal oxide materials such as SnO_2, ZnO, WO_3, $ZnSnO_4$ are drawing attention as the next-generation ETL. Thus, using DFT at the PBE0+spin–orbit coupling(SOC)+Grimme-D3 van der Waals level of theory, we study a recently discovered La-doped $BaSnO_3$, which has achieved 22 % PCE, and discuss the key factor for the optimal band alignment at the $MAPbI_3$/LBSO interface.

Organic cations such as MA in LHPs have the rotational degrees of freedom. However, we show that the rotational degrees of freedom of MA's dipole at the TiO_2/perovskite interface is significantly suppressed. We study the interface between rutile TiO_2 and cubic $MAPbI_3$ using DFT and AIMD simulations and show that proton-mediated electron transfer process exists because of the strong short hydrogen bonding, which is a drastically different picture compared to the bulk.

The developments of hydrogen-based energy conversion and storage are imperative for the efficient and environment-friendly future energy fuel. A theoretical understanding of the water splitting reaction (hydrogen evolution reaction(HER) at the cathode and oxygen evolution reaction(OER) at the anode) is therefore crucial for the design of artificial HER/OER catalysts. From the HER experiment of Pt-Graphitic tube-FeCo/Cu system, we provide a mechanism for the superb HER which showed extremely high turnover frequency(7.2/s), low overpotential(18 meV at 10 mA/cm^2), and small Tafel slope(24 mV·dec^{-1}) using ultra-low Pt loading. Though single Pt-C_2N_2 in graphitic tube has ideal free energy ($\Delta G \approx 0$) for HER, the conductivity is very low limiting the steady state mass transfer of electrons inside the cathode. We show that Pt single atoms in the presence of Pt clusters drastically improves the conductivity of the graphitic tubes and hence the activity of the Pt single atoms. We also study the core-level X-ray absorption spectrum of single atom catalyst systems using *ab initio* methods.

Nonequilibrium quantum mechanics is still a challenging area awaiting for a general theory like the imaginary-time method of equilibrium quantum mechanics. In a steady state, we need a general framework of nonequilibrium quantum mechanics instead of the real-time propagation which is system-dependent and is limited to high-energy regime(or ultra-fast process $\sim fs$). We derive an analytic solution of the nonequilibrium Anderson impurity model on Keldysh contour(steady state) by including vertex corrections(called one-crossing approximation) in frequency domain using pseudo-particle formalism. We derive the lesser(greater) pseudo-particle self-energy(empty, singly-occupied, doubly-occupied) and the lesser(greater) impurity Green's function to obtain the impurity spectral function and the DC current through the impurity. We can access to a low energy scale which had been formidable to the real-time propagation methods. The nonequilibrium solution exactly corresponds to the equilibrium solution at the equilibrium limit.

Contents

List of Figures

List of Tables

I Introduction

Solar energy is a very efficient and environment-friendly energy source for the energy harvesting, which was first introduced as the practical silicon solar cell in 1954.[1] Since the advent of silicon-based solar cells, various types of solar cells were discovered. Recently, inorganic-organic hybrid lead halide perovskite solar cells (PSCs) based on ABX_3 (A = Cs^+, $CH_3NH_3^+$ (MA), $CHN_2H_4^+$ (FA), $N_2H_5^+$ (HZ); B = Pb^{2+}; X = Cl^-, Br^- or I^-) are revealed and are considered as the most promising large-scale energy source achieving the power conversion efficiency (PCE) of 23.7 %.[2] PSCs possess many interesting physical properties, including giant dielectric constant,[3] hot-phonon bottleneck,[4] high harmonic generation, anharmonicity,[5] bright triplet emission,[6] free excitons,[7] Rashba effect,[8] defect tolerance,[9] and polaron state.[10] As the efficiency of inorganic/organic hybrid PSCs increases, design principles are urgently required for higher PCE.

Generally, the electrons in crystals experience a degree of deformation of a surrounding lattice in addition to the Bloch potential because of the large polarity of ionic bonds. Then, charge carriers are described by polaron quasiparticles owing to the coupling between electrons and lattice phonons. In the case of lead halide PSCs, there has been a critical debate on the main source of electron-phonon coupling (e-ph) either optical or acoustic. From the temperature dependence of the mobility $\mu \propto T^{-\frac{3}{2}}$ near the room temperature, the acoustic phonons were considered to be the main source of e-ph coupling.[11] On the other hand, in recent research, longitudinal optical (LO) phonons are provided as the main source of the polaron state.[12] Operating temperatures of cubic $MAPbI_3$ ($\sim$ 330 K) is above the Debye temperature of $\Theta_D \sim 175K$.[13] Therefore, it is natural that the high energy LO phonon modes are highly populated at operating temperatures of lead halide PSCs. Thus here, I further investigate the correlation between the polaron in LHP and A-site cation and show that the coordination of A-site cation to halides is important to determine the polaron mobility of LHP.

The spin-orbit coupling (SOC) field, which is odd function in k (momentum) and time reversal symmetric, at the interface of hetero-structures gives rise to the Rashba-Dresselhaus (RD) splitting of the degenerate bands. We can easily derive the effective low order perturbation of RD Hamiltonian and define the strength of the RD interaction by the constant $\alpha_{RD} = \frac{\Delta E}{2\Delta|k|}$ (eV·Å). Since the interaction of RD is common that many systems like non-centrosymmetric crystals, hetero-junctions, metal surfaces and graphene show considerable energy splitting. Recently, lead halide PSCs containing heavy elements like Pb and I can exhibit large RD coupling constants ($\alpha_{RD} \sim$ 1.6 eV ·Å) in 2D $(C_6H_5C_2H_4NH_3)_2PbI_4$ and $\alpha_{RD} \sim 2.75 - 3.75$ (eV·Å) is $MAPbBr_3$ and 3D $CsPbBr_3$ nanocrystals.[14, 15, 16] I studied an elusive part of LHP/graphene and LHP/ETL interfaces using the density functional theory and *ab initio* molecular dynamics (AIMD) simulations to account for RD spin-orbit effect. I carried out the calculations for graphene/cubic-$CsPbI_3$(001) as a prospective interface for improving carrier transport and for TiO_2/ cubic-$MAPbI_3$(001) as a well-known ETL material for PSC devices. Although we observed RD interactions at both interfaces, their mechanisms are different in intriguing ways.

Anatase and rutile TiO_2 has been the most widely used electron transport layer (ETL) material in lead halide PSC devices. However, the photo-degradation of TiO_2 by ultraviolet (UV) rays deteriorates the device performance gradually.[17] Direct optical measurements show that an electron barrier of ~ 0.1 eV is present at the $MAPbI_3/TiO_2$ interface, and such a large electron barrier can cause I-V hysteresis by the accumulation of iodine defects at $MAPbI_3/TiO_2$. To overcome these obstacles, the development of efficient and reliable next-generation ETL substances has emerged recently. Metal oxide materials such as SnO_2, ZnO, WO_3, $ZnSnO_4$ are drawing attention as the next-generation ETL.[18] Thus, using DFT at the PBE0 + spin–orbit coupling (SOC) + Grimme-D3 van der Waals level of theory, I studied recently discovered La-doping on $BaSnO_3$ ETL, which has achieved 22 % PCE,[19] and discuss the key factor for the optimal band alignment at the $MAPbI_3$/LBSO interface.

Effective low cost hydrogen production is imperative for the future energy industry. Thus, theoretical understanding of the water splitting process, hydrogen evolution reaction (HER) at the cathode and oxygen evolution reaction (OER) at the anode, is important. From the HER experiment with the Pt-Graphitic tube-FeCo/Cu system, I provided a mechanism for the superb HER which showed extremely high turnover frequency (7.2/s), low overpotential (18 meV at 10 mA/cm^2), and small tafel slope (24 mV dec^{-1}) using ultralow Pt loading.[20] Though single Pt-C2N2 in graphitic tube has ideal free energy ($\Delta G = 0$) for HER, the conductivity is very low, thus limiting the steady state mass transfer of electrons at the cathodes. Thus, we proposed a model which accounts for the mass transfer of cathodic electrons (or simply conductivity) in N-doped graphene cathode. I show that Pt single atoms in the presence of Pt clusters drastically improves the conductivity of the graphitic tubes and hence the activity of the Pt single atoms.

It is well known that the quantum mechanics lacks a complete description of nonequilibrium dynamics. The non-equilibrium dynamics of quantum mechanics is still uncharted territory. At this stage, the Keldysh (or Kadanoff-Baym) contour with Green's function method is the major theory to understand the nonequilibrium quantum mechanics. Here, I have derived an analytic solution of the nonequilibrium Anderson impurity model (AIM) on the Keldysh contour by including vertex self-energy terms in real frequency domain using the pseudo-particle formalism. Since now the derivation of nonequilibrium AIM in real frequency with higher order terms has been a formidable task because of its complexity. The real frequency solution can access to a low energy scale (up to Kondo scale) which is not possible for the real-time propagation. In the equilibrium limit which satisfies the fluctuation-dissipation theorem, the derived solution exactly corresponds to the equilibrium solution.[21]

Bibliography

[1] Chapin, D. M.; Fuller, C. S.; Pearson, G. L. A New Silicon p-n Junction Photocell for Converting Solar Radiation into Electrical Power. *Journal of Applied Physics* **1954**, *25*, 676–677.

[2] The National Center for Photovoltaics (NCPV). Retrieved from `https://www.nrel.gov/pv/assets/pdfs/pv-efficiency-chart.20181221.pdf`, 2018.

[3] Juarez-Perez, E. J.; Sanchez, R. S.; Badia, L.; Garcia-Belmonte, G.; Kang, Y. S.; Mora-Sero, I.; Bisquert, J. Photoinduced Giant Dielectric Constant in Lead Halide Perovskite Solar Cells. *Journal of Physical Chemistry Letters* **2014**, *5*, 2390–2394.

[4] Hopper, T. R.; Gorodetsky, A.; Frost, J. M.; Müller, C.; Lovrincic, R.; Bakulin, A. A. Ultrafast Intraband Spectroscopy of Hot-Carrier Cooling in Lead-Halide Perovskites. *ACS Energy Letters* **2018**, *3*, 2199–2205.

[5] Marronnier, A.; Roma, G.; Boyer-Richard, S.; Pedesseau, L.; Jancu, J. M.; Bonnassieux, Y.; Katan, C.; Stoumpos, C. C.; Kanatzidis, M. G.; Even, J. Anharmonicity and Disorder in the Black Phases of Cesium Lead Iodide Used for Stable Inorganic Perovskite Solar Cells. *ACS Nano* **2018**, *12*, 3477–3486.

[6] Becker, M. A.; Vaxenburg, R.; Nedelcu, G.; Sercel, P. C.; Shabaev, A.; Mehl, M. J.; Michopoulos, J. G.; Lambrakos, S. G.; Bernstein, N.; Lyons, J. L.; Stöferle, T.; Mahrt, R. F.; Kovalenko, M. V.; Norris, D. J.; Rainò, G.; Efros, A. L. Bright Triplet Excitons in Caesium Lead Halide Perovskites. *Nature* **2018**, *553*, 189–193.

[7] Miyata, A.; Mitioglu, A.; Plochocka, P.; Portugall, O.; Wang, J. T. W.; Stranks, S. D.; Snaith, H. J.; Nicholas, R. J. Direct Measurement of the Exciton Binding Energy and Effective Masses for Charge Carriers in Organic-Inorganic Tri-Halide Perovskites. *Nature Physics* **2015**, *11*, 582–587.

[8] Myung, C. W.; Javaid, S.; Kim, K. S.; Lee, G. Rashba-Dresselhaus Effect in Inorganic/Organic Lead Iodide Perovskite Interfaces. **2018**, *3*, 1294–1300.

[9] Kim, J.; Lee, S. H.; Lee, J. H.; Hong, K. H. The Role of Intrinsic Defects in Methylammonium Lead Iodide Perovskite. *Journal of Physical Chemistry Letters* **2014**, *5*, 1312–1317.

[10] Myung, C. W.; Yun, J.; Lee, G.; Kim, K. S. A New Perspective on the Role of A-Site Cations in Perovskite Solar Cells. *Advanced Energy Materials* **2018**, *8*, 1–7.

[11] Milot, R. L.; Eperon, G. E.; Snaith, H. J.; Johnston, M. B.; Herz, L. M. Temperature-Dependent Charge-Carrier Dynamics in $CH_3NH_3PbI_3$ Perovskite Thin Films. *Advanced Functional Materials* **2015**, *25*, 6218–6227.

[12] Wright, A. D.; Verdi, C.; Milot, R. L.; Eperon, G. E.; Pérez-Osorio, M. A.; Snaith, H. J.; Giustino, F.; Johnston, M. B.; Herz, L. M. Electron–Phonon Coupling in Hybrid Lead Halide Perovskites. *Nature Communications* **2016**, *7*.

[13] Feng, J. Mechanical Properties of Hybrid Organic-Inorganic $CH_3NH_3BX_3$ (B = Sn, Pb; X = Br, I) perovskites for solar cell absorbers. *APL Materials* **2014**, *2*.

[14] Zhai, Y.; Baniya, S.; Zhang, C.; Li, J.; Haney, P.; Sheng, C.-X.; Ehrenfreund, E.; Vardeny, Z. V. Giant Rashba Splitting in 2D Organic-Inorganic Halide Perovskites Measured by Transient Spectroscopies. *Science Advances* **2017**, *3*, e1700704.

[15] Niesner, D.; Wilhelm, M.; Levchuk, I.; Osvet, A.; Shrestha, S.; Batentschuk, M.; Brabec, C.; Fauster, T. Giant Rashba Splitting in $CH_3NH_3PbBr_3$ Organic-Inorganic Perovskite. *Physical Review Letters* **2016**, *117*, 1–6.

[16] Isarov, M.; Tan, L. Z.; Bodnarchuk, M. I.; Kovalenko, M. V.; Rappe, A. M.; Lifshitz, E. Rashba effect in a single colloidal CsPbBr3 perovskite nanocrystal detected by magneto-optical measurements. *Nano Letters* **2017**, *17*, 5020–5026.

[17] Leijtens, T.; Eperon, G. E.; Pathak, S.; Abate, A.; Lee, M. M.; Snaith, H. J. Overcoming Ultraviolet Light Instability of Sensitized TiO_2 with Meso-Superstructured Organometal Tri-Halide Perovskite Solar Cells. *Nature Communications* **2013**, *4*, 1–8.

[18] Shin, S. S.; Lee, S. J.; Seok, S. I. Exploring Wide Bandgap Metal Oxides for Perovskite Solar Cells. *APL Materials* **2019**, *7*, 022401.

[19] Shin, S. S.; Yeom, E. J.; Yang, W. S.; Hur, S.; Kim, M. G.; Im, J.; Seo, J.; Noh, J. H.; Seok, S. I. Colloidally Prepared La-Doped $BaSnO_3$ Electrodes for Efficient, Photostable Perovskite Solar Cells. *Science* **2017**, *356*, 167–171.

[20] Tiwari, J. N.; Sultan, S.; Myung, C. W.; Yoon, T.; Li, N.; Ha, M.; Harzandi, A. M.; Park, H. J.; Kim, D. Y.; Chandrasekaran, S. S.; Lee, W. G.; Vij, V.; Kang, H.; Shin, T. J.; Shin, H. S.; Lee, G.; Lee, Z.; Kim, K. S. Multicomponent Electrocatalyst with Ultralow Pt Loading and High Hydrogen Evolution Activity. *Nature Energy* **2018**, *3*, 773–782.

[21] Myung, C. W.; Haule, K.; Lee, G.; Kim, K. S. Nonequilibrium Anderson Impurity Model on Keldysh Contour : One-Crossing Approximation. **2018**, (in press).

II Lead halide perovskite solar cells

2.1 A new perspective on the role of A-site cation for steering Frohlich polaron and its experimental verification

As competition becomes more intensive toward high efficiency of lead halide perovskite solar cells (PSCs), a design method to minimize carrier transport loss aiming for higher PCE is urgently required. Here, we reveal the role of the A-site cations for the carrier transport, which was largely ignored up to date, to tune the coupling of Frohlich electronic-phonon (e-ph) interactions with longitudinal optical (LO) phonons. We found that Fröllich polaron interaction is controlled by the coordination between the proton (or lithium) and halogen ions. The design principle proposes a route to reduce the e-ph scattering by reducing the Born effective charge and by reducing the LO motion of Pb and I. This novel principle discloses some of promising organic cations, including hydrazinium cation ($NH_3NH_2^+$; HZ), Li^+-methylamine (Li^+-NH_2CH_3; LM), and hydroxyl-ammonium cation (NH_3OH^+; HA) which is comparable with the methylammonium cation.[1]

Based on our prediction, we can replace the organic A-site in the perovskite into N2H5+ (HZ) cation which can control the proton coordination to I. This prediction was experimentally demonstrated with an optimized perovskite device containing 2% N_2H_5Cl additive showing 85 % of the fill factor (FF) which is the maximum closest to the Shockley-Queisser limit. With HZ additive, additional PCE of 2.3% and FF of 14% are improved compared to $MAPbI_3$.[2]

2.1.1 A new perspective on the role of A-site cation for steering Frohlich polaron and its experimental verification

Little is known about the A-site cation's role on the polaron properties of lead halide PSCs until now. From the retrospective, it is important to find the A-site cation whose size is suitable for the semi-empirical factor, called Goldschmidt tolerance factor $t = \frac{(r_A+r_X)}{(\sqrt{2}(r_Pb+r_X))}$.[3] The size of the A-site cation also controls the rotation of the octahedron which is related with the band gap of the lead halide PSCs. One of the most widely used $MAPbI_3$'s instability is partially understood from the small ionic radius r_A with t 0.9 $<$ 1.0. Many researchers tried to circumvent the problem by adjusting the size of the A-site cation.

In polar semiconductors, a periodic dipole moment is formed by strong ionicity of the crystal. Since the dipole-dipole interaction decays $\sim \mathbf{r}^{-2}$, the interaction of long-range phonons ($\mathbf{q} \to 0$) diverges as $\sim \mathbf{q}^{-1}$.[4] Only the LO modes at the long-range limit contribute e-ph coupling to the band edge states. To reduce the e-ph interaction which interferes with the carrier transport of the semiconductor, the dipole (i.e. the Born effective charge and the vibrational eigenmode component) of a given unit cell has to be reduced.

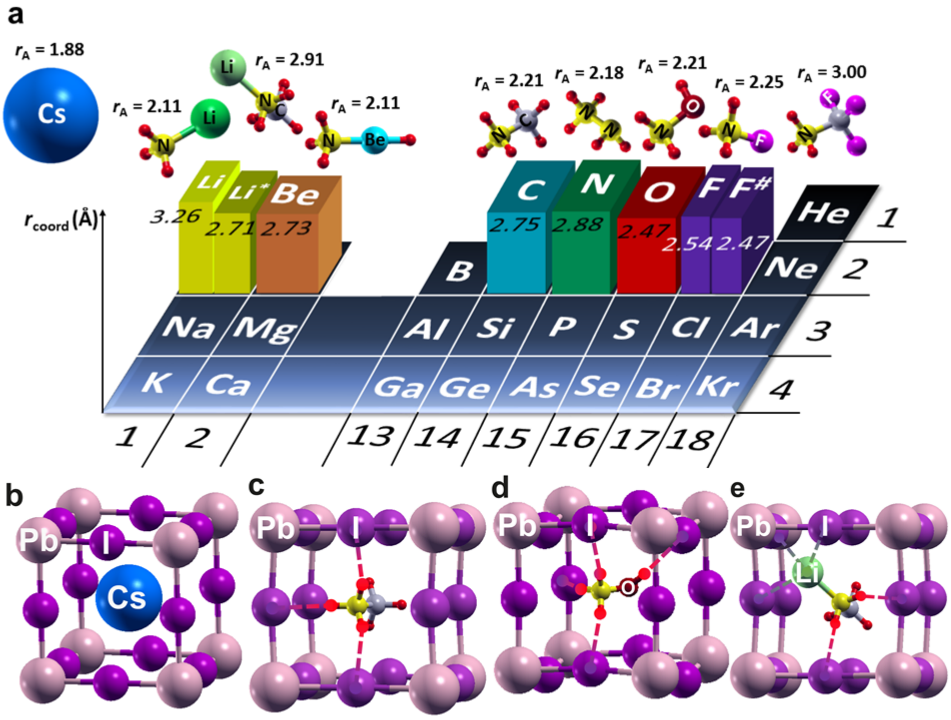

Figure 1: (a) Average of I^- coordination distance r_{coord} and the estimated ionic radius r_A for various A-site organic cations. Li* refers to $LiNH_2CH_3^+$ and F# refers to $NH_3CF_3^+$. $NH_3BH_2^+$ does not form a molecular bond according to our DFT calculations. All units are in Å. (b) Dodeca-coordination of Cs^+ (c) tri-coordination of MA (d) tetra-coodination of NH_3OH^+, HA (e) penta-coordination of $LiNH_2CH_3^+$, LM. Copyright 2018 Wiley.

A simple rule for the better charge carrier transport is to adjust the A-site cation close to I and increase the number of coordination site between cation and I. An optimal cation effectively reduces the e-ph coupling by decreasing the Z^*_κ of Pb and I ions and by decreasing the eigenmodes $\mathbf{e}(\mathbf{q})$ of Pb and I with the increased coordination number of cations. The time scale of the recently measured reorientation of the MA molecule in the pseudo-cubic cage is long enough ($\sim 14ps$) to participate in the lattice vibration of the Pb-I frame to form the polaron state. We have found that CH_3 can be converted into Li(NH_3Li^+), BeH, BH_2, NH_2 ($NH_3NH_2^+$: hydrazinium; HZ), OH (NH_3OH^+: hydroxyl-ammonium cation; HA), F (NH_3F^+ Ammonium cation, expressed in terms of fA, taking into account that FA is used to represent formamidinium cation) and we have calculated the average distance and ionic radius. HZ and HA are easily available from the lab. Though we found the spectra of fA, fA is difficult to synthesize. However, we calculated the above cations to understand the role of A-site cations on polaronic interactions. The HZ result is very similar to MA, so HZ's result is omitted here to reduce the complexity of comparison focusing on comparison of Cs, MA, HA, and fA. The HZ's result can be found in elsewhere. Using the DFT calculation, we can see that the average coordination distance of MA (2.75 Å) decreases to 2.47 Å for HA and 2.54 Å for fA (Figure 1a). The ionic hydrogen bonds of HA and fA (0.2 - 0.3 Å decreased with respect to MA) results in smaller Z^*_κ(Pb, I) than MA's.

Another way to achieve our goal is to fluorinate H atoms of CH_3 to form $NH_3CF_3^+$ (trifluoromethylammonium: TA) or to substitute $LiNH_2CH_3^+$ (lithium-methylamine: LM). LM is difficult to synthesize again, but its spectrum was indeed observed in the experiment. These molecules were also investigated to understand what kind of molecular form is useful to reduce e-ph coupling. Various configurations of A-site cations with surrounding I- ions are observed using DFT geometry optimization (Figures 1b-e). The inorganic Cs^+ is very weakly dodeca-coordinated by I^- and has a relatively large distance ($\sim$ 4.5 Å). Typical A-site cation MA forms three strong ionic hydrogen bonds between I and H, a tri-coordination (Figure 1c). HA forms an additional coordination between OH and I^- (Figure 1d). In addition, LM being with Li^+ instead of a proton can form noncovalent bonding to five I^-s (Figure 1e). Examples of these cations can actually manipulate the coordination number from tri-(Figure 1c), tetra-(Figure 1d) to penta-coordination (Figure 1e) with very strong bonding strength using different organic cations.

2.1.2 Effects by organic A-site cation *versus* inorganic A-site cation

Since the A site cation is not located the low energy spectrum of the electronic structure, it is expected to be hardly involved in carrier transport. However, it was revealed that selection of A-site cation is important because of the polar character of lead halide PSCs. We manifest this difference from the example of two well-known materials: the cubic $CsPbI_3$ and $MAPbI_3$. The phonon dispersion (Figs. 2a and b) shows large LO (longitudinal optical)-TO (transverse optics) splitting due to the large Born effective charge of Pb and I. Non-analytic dynamic matrix of ionic crystal appears from long-range macroscopic Coulomb interactions introducing the LO-TO splitting called Lynddane-Sachs-Teller (LST) relationship. Though LST is not exactly applicable for this model, the relationship may be a measure of the polarity of the crystal. Organic cations, including MA, reduce the LO-TO splitting and show that it can effectively lower the long-range Coulomb interactions.

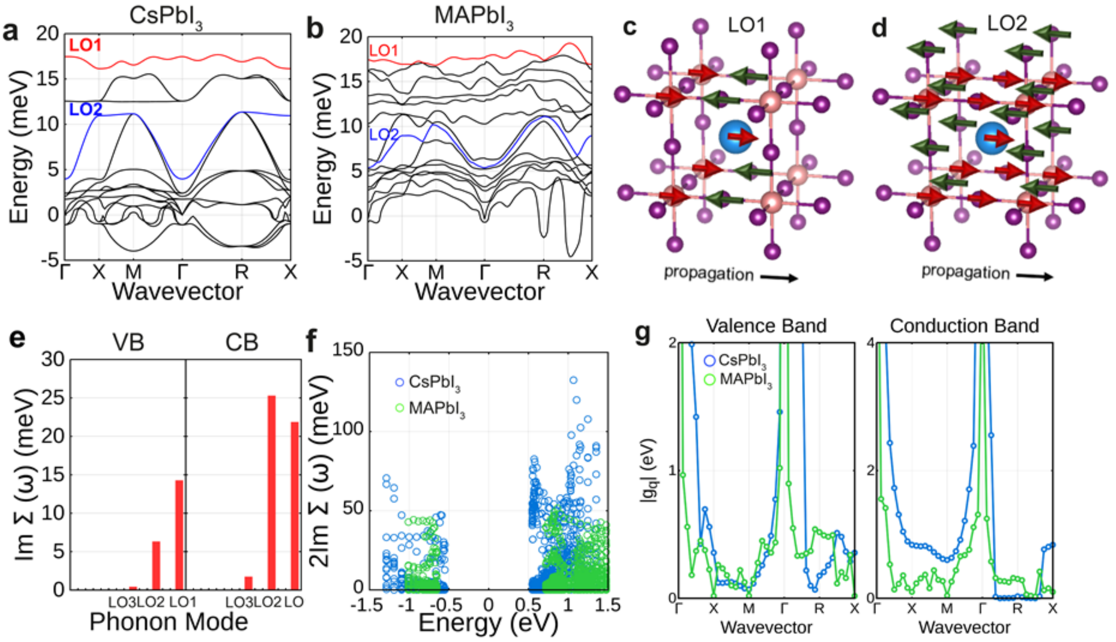

Figure 2: (a) $CsPbI_3$ and (b) $MAPbI_3$ with LO1 (red) and LO2 (blue). The schematic for the eigenmodes of (c) LO1 and (d) LO2 in $CsPbI_3$. (e) Electron-phonon self-energy of VB and CB at $\mathbf{R}(0.5, 0.5, 0.5)$ of BZ of LO1, LO2, and LO3. (f) Scattering rate τ^{-1} $(2\mathrm{Im}\{\Sigma(\mathbf{k},\omega)\})$ along (η,η,η) to R(0.5, 0.5, 0.5) and R(0.5, 0.5, 0.5) to (0.5, η, 0.5) with $0.45 < \eta < 0.5$ at 330 K for $CsPbI_3$ (blue) and $MAPbI_3$ (green). (g) Fröhlich e-ph coupling constant $g_{mn}(m = n)$ of $CsPbI_3$ (blue) and $MAPbI_3$ (green) for VB (left) and CB (right). Copyright 2018 Wiley.

The energy (E_{LO1}) of the highest LO mode (LO1) of $CsPbI_3$ (17.47 meV) is larger than $MAPbI_3$ (16.21 meV). A clear separation between heavy Cs^+ modes (which are mainly low energy modes $\sim$ 5 meV) and PbI_3 optical phonon modes ($>$ 5 meV) is observed for $CsPbI_3$ (Figure 2a). In $MAPbI_3$, the rotation and translation modes of MA are mixed with PbI_3 LO modes (Figure 2b). Lighter molecules such as MA interacting with I^- by anisotropic directional hydrogen bonds destroy the symmetry of the PbI_3 lattice and effectively suppresses the PbI_3 LO lattice oscillation by linear I$\cdots$HN halogen-hydrogen bonding perpendicular to the Pb^{2+}-I^--Pb^{2+} perovskite skeleton.

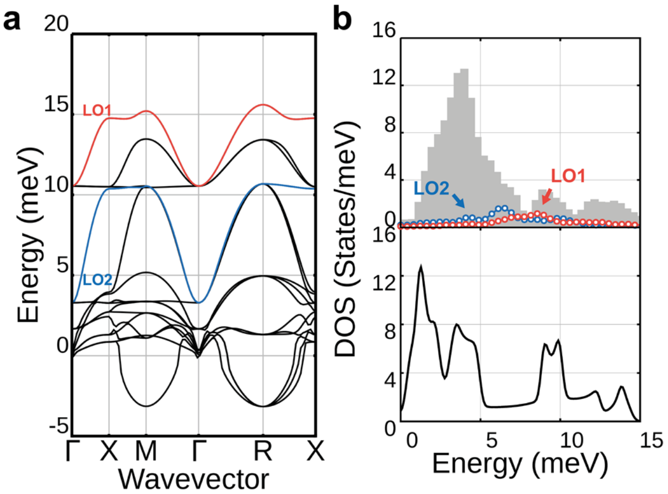

Figure 3: (a) Phonon dispersion of CsPbI3 using DFPT without long-range non-analytical correction with LO1 (red) and LO2 (blue). (b) Fourier transformed velocity autocorrelation (VAC) of cubic $(2\times2\times2)$ supercell from *ab initio* MD simulation for 10 *ps* at 600 K. 0K phonon DOS (black line); LO1 (red line); LO2 (blue line); projected DOS from the VAC of the MD (gray bar). Copyright 2018 Wiley.

The calculation of e-ph coupling for all modes suggests that most contributions of e-ph scattering in both $CsPbI_3$ and $MAPbI_3$ at the valence band (VB) and conduction band (CB) band edges are from the highest LO mode (LO1; red) and the second highest LO mode (LO2; blue) (Figs. 2a and 2b). Except for LO1 (Figure 2c) and LO2 (Figure 2d), the contribution of the other 13 modes is nearly negligible (Figure 2e). Therefore, observing these two predominant modes, it is easy to follow changes in e-ph coupling after substituting MA for other cations at the A-site. The e-ph scattering is much larger than that of $MAPbI_3$ (Figure 2f), because the polarization of Pb^{2+}-I^- bond is higher in $CsPbI_3$ and the contribution of PbI_3 LO oscillation in the eigenmode is large. Replacement of the cation Cs^+ with MA reduces e-ph coupling due to suppression of PbI_3 LO phonon mode. There are concordant results with our design principle that organic cations such as MA reduce the scattering rate compared to inorganic PSCs (Figure 2f). Fröllich e-ph interactions $g_{mn\mathbf{q}}(m = n)$ of LO1 and LO2 of $CsPbI_3$ (blue) and $MAPbI_3$ (green) shows that in addition to the overall decrease in the e-ph coupling of $MAPbI_3$, the long-range interactions $(q \to 0)$ are substantially quenched (Figure 2g). These overall observations point out that appropriately selected organic cations have better carrier mobility than inorganic counterpart.

Negative (imaginary) acoustic modes such as at **M**(tetragonal) and **R**(orthorhombic) indicate the instability of the cubic structure at 0 K. Since, we are interested in the longitudinal optical modes, our calculation is justified unless the LO spectrum significantly changes at high temperatures. The Fourier transformed velocity autocorrelation function (VAC) MD spectra from the molecular dynamics (MD) simulation at $\sim$ 600 K, which is higher than the critical temperature of the cubic phase, T_C ($\sim$ 583 K),[5] coincides with 0 K lattice phonon density of states (DOS). Thus, we confirm that LO1 and LO2 energy DOS do not change much (Figure 3a and b).

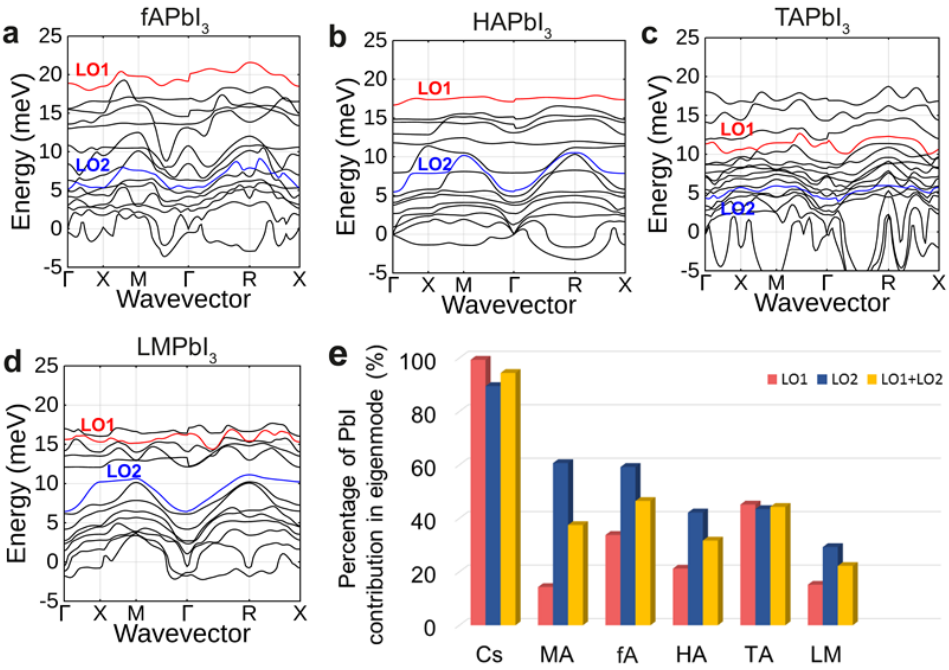

Figure 4: Phonon dispersion of (a) fAPbI$_3$ (b) HAPbI$_3$ (c) TAPbI$_3$ (d) LMPbI$_3$. (e) A histogram of the dynamic matrix components of LO eigenmodes of LO1 (red), LO2 (blue), and the average (yellow). The portion of the A site cationic component in the LO mode increases as the organic cations are introduced. The eigenmode contribution of A site cation of LO mode is Cs (5.6 %), MA (62.5 %), fA (53.5 %), HA (68.3 %), TA (55.7 %) and LM (77.8 %). The eigenmode component of Pb-I is absorbed by the organic cations. Copyright 2018 Wiley.

Therefore, we assume that the phonon spectra of the high energy LO modes are not seriously affected at high temperatures. We choose the most promising cations according to the coordinate number [MA(3) $<$ HA(4) $<$ LM(5)] and the coordinating distance of the A-site cation: [d(fA), d(TA), d(HA) $<$ d(MA)]. The Born effective charge Z^*_κ of the I atom adjusted by the organic cation decreases to $MA > LM > HA > fA > TA$. When being substituted with O, F or fluorinated, cations acting as buffers can reduce effective Pb-I dipole. In the case of fAPbI$_3$, the cation coordination can reduce Z^* by 40 % over non-coordinated one.

The coordination number is important because the Pb^{2+}-I LO eigenmode is absorbed by the translational organic cation modes through the coordination. Increasing the coordination number amounts to reduce $(\frac{\omega_{LO}}{\omega_{TO}})^2$ of HA (1.26) (Figure 4b) and LM (1.33) (Figure 4d) compared to MA (1.46) (Figure 2b and Table 1). LMPbI$_3$ shows a useful example showing how Pb-I eigenmodes of LO1 and LO2 are reduced as the number of coordination increases. For the LM cation (Figure 1e), the combination of LO mode with cation and degree of screening is maximized by halogen-hydrogen bond and directional linear $I\cdots LiNH_2$ halogen-lithium bonding. The tetra-coordinated HA cation absorbs more Pb-I LO mode than MA cation. (Figure 4e)

Table 1: Electronic and vibrational properties and the Goldschmidt tolerance factor t of cubic $APbI_3$ with Cs, MA, fA, HA, TA, and LM A-site cations.

	t	Z^*(Pb)	Z^*(I)	ϵ_∞	$E_{LO1}(meV)$	$(\omega_{LO}/\omega_{TO})^2$
$CsPbI_3$	0.85	4.99	-4.99	6.81	17.47	1.94
$MAPbI_3$	0.92	4.92	-5.58	7.86	16.21	1.46
$fAPbI_3$	0.93	4.70	-4.26	7.24	15.59	1.32
$HAPbI_3$	0.92	4.72	-4.62	7.22	16.65	1.26
$TAPbI_3$	1.09	4.71	-4.11	5.92	11.33	1.68
$LMPbI_3$	1.07	4.83	-5.30	7.10	15.61	1.33

2.1.3 Perovskite solar cells materials containing prospective organic cations

The overall discussion can be summarized in Figure 4. In VB and CB, we found that TAPbI3, which was considered to be a promised cation, contains a new LO motion between F and Pb-I. In this additional LO mode, the e-ph scattering is large. For VB, the scattering rates of HA and LM are comparable to the that of MA. However, it is interesting to note that the fA, which buffers the large polarizability between Pb and I, reduces the scattering rate to the half of that of MA (Figure 5a). For CB, it is clear that the scattering rates are reduced for fA, HA, and LM. In particular, LM drastically reduces e-ph scattering (Figure 5b) due to the maximum mixing between Pb-I LO mode and LM (Figure 4e). Electron self-energy of Rayleigh-Schrodinger perturbation theory for nondegenerate conduction band minimum at Γ of Brillouin Zone (BZ) is given by $\mathrm{Re}\{\Sigma(\mathbf{k},\omega)\} = -\alpha\hbar\omega_{LO}$ at 0 K, where α is polaron coupling constant. Though the relation is not exactly matched with our model, this still can provide some measure of polaron coupling. Therefore, the comparison of polaron coupling constants at 0 K [$\alpha(\mathrm{CsPbI_3}) > \alpha(\mathrm{MAPbI_3}) > \alpha(\mathrm{HAPbI_3}) > \alpha(\mathrm{LMPbI_3})$ (Figure 5c)] shows that the prospective organic cations are able to

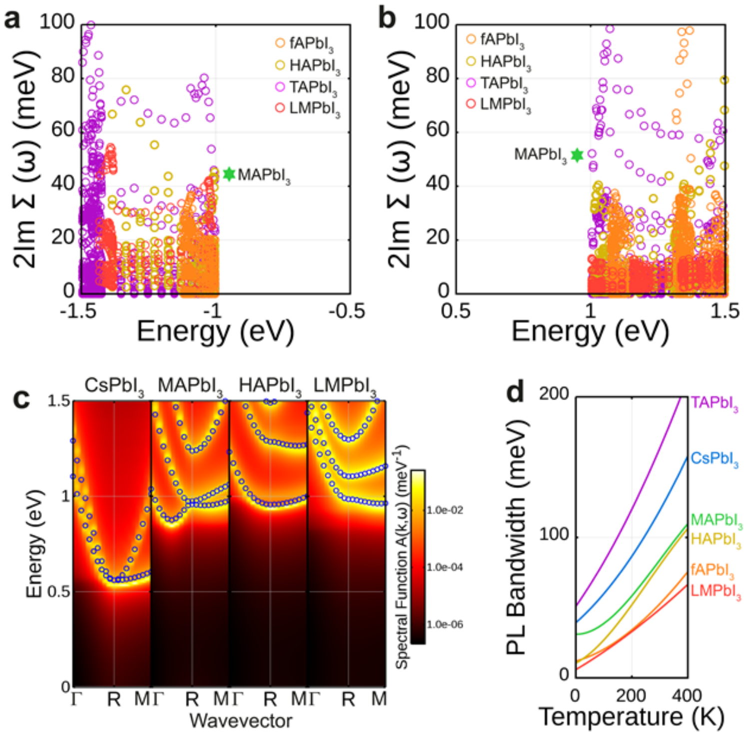

Figure 5: (a) Hole and (b) electron scattering rate $2\mathrm{Im}\{\Sigma(\mathbf{k},\omega\}$ of fAPbI$_3$(orange), HAPbI$_3$(yellow), TAPbI$_3$(purple), LMPbI$_3$(red), at band extrema of $\mathbf{R}$(0.5,0.5,0.5) to (0.5,η, 0.5) where $0.45 < \eta < 0.5$ at 330 K. Scattering rates for MAPbI$_3$ are green stars. (c) The electronic spectral function of CsPbI$_3$, MAPbI$_3$, HAPbI$_3$, and LMPbI$_3$ around $\mathbf{R}$(0.5, 0.5, 0.5) with the DFT Kohn-Sham energy (blue circles). (d) Photoluminescence bandwidth of CsPbI$_3$(blue), MAPbI$_3$ (green), HAPbI$_3$(yellow) and LMPbI$_3$(red), MAPbI$_3$(green), and fAPbI$_3$(orange). Copyright 2018 Wiley.

reduce the polaron coupling. We observe that from photoluminescence (PL) bandwidths as the function of temperatures (Figure 5d), HA and fA, which form strong coordination to I, and LM which makes a large coordination number to I are promising A-site organic cations for highly efficient PSCs. Finally, we estimate the mobility for the prospective materials at 330 K for electrons, $\mu_{TA}(61.85) < \mu_{Cs}(73.94) < \mu_{MA}(118.08) < \mu_{HA}(150.82) < \mu_{fA}(162.92) < \mu_{LM}(464.41)$, and for holes $\mu_{TA}(57.88) < \mu_{Cs}(98.11) < \mu_{HA}(102.22) < \mu_{MA}(108.70) < \mu_{LM}(110.25) < \mu_{fA}(226.77)$ from the mobility $\mu = \frac{e\tau}{m^*}$ $(cm^2V^{-1}s^{-1})$.

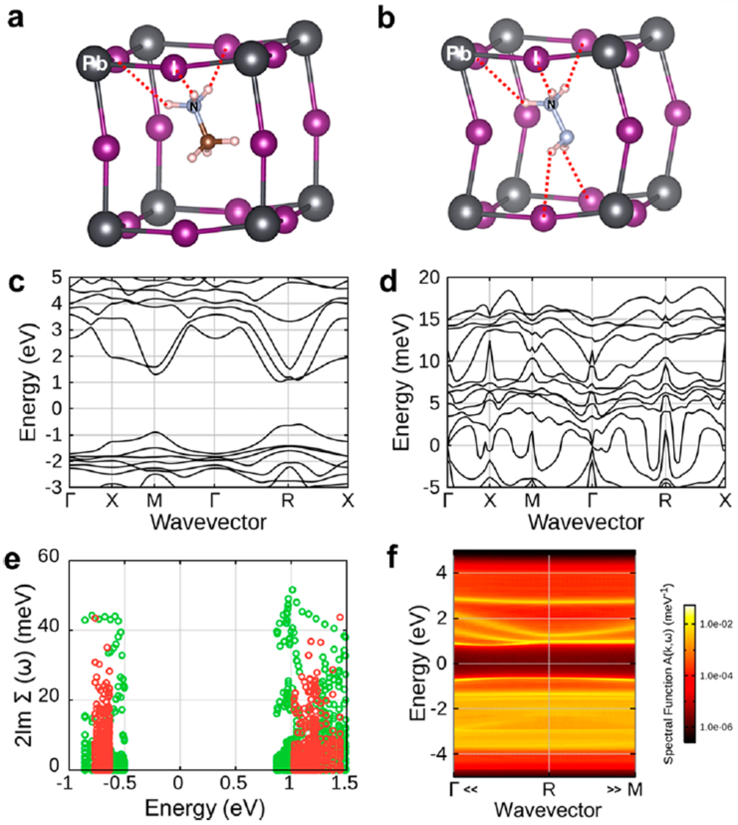

Figure 6: (a) MA and (b) HZ with Pb (gray) and I (purple) (c) The electronic band structure of cubic $HZPbI_3$. (d) The phonon dispersion of cubic $HZPbI_3$. (e) The imaginary part of the electron phonon self-energy of $MAPbI_3$ (green)[1] and $HZPbI_3$ (red). (f) The spectral function $A(\mathbf{k}, \omega)$. Copyright 2018 American Chemical Society.

2.1.4 Novel inorganic cation N_2H_5

DFT+many-body theory showed long-range LO phonon coupling is quenched by increasing the number of coordination to I^- ions by A-site organic cations.[1] Inorganic N_2H_5(HZ) forms five I-H-N hydrogen bonds at a distance of 2.5-2.9 Å (Figure 6 a, b). The contribution of ions (or vibrations) to static dielectric $\epsilon_{0,ionic}$ is reduced by 3 % substituting MA for HZ in the density functional perturbation theory calculation (Figure 6d). As a result, the Born effective charge of Pb and I are reduced by 8.5 % and 3 %, respectively. We have also calculated the imaginary part of the spectral function (Figure 6f) and the bandwidth (Figure 6e). The band width of the valence band edge decreased by 20 % and that of the conduction band decreased by 48 %. [2]

In order to investigate the characteristics of the PV device, an inverted p-i-n (p-type intrinsic n-type) plane perovskite solar cell was fabricated using ITO/PEDOT:PSS/perovskite layer/$PC_{61}BM$/Al electrode of pristine $MAPbI_3$ and with 2 %, 5 % and 10 % HZCl additives (Figure 7). Note that with 2 % of HZCl additive the PCE of the PV device shows the best performance under 100 $mWcm^{-2}$AM1.5G irradiation: 16.45 % PCE (2.3 % increase), J_{SC} 20.12 $mAcm^{-2}$, V_{OC} 0.96 V, and fill-factor (FF) 0.85, which is is close to the Shockley-Queisser limit.

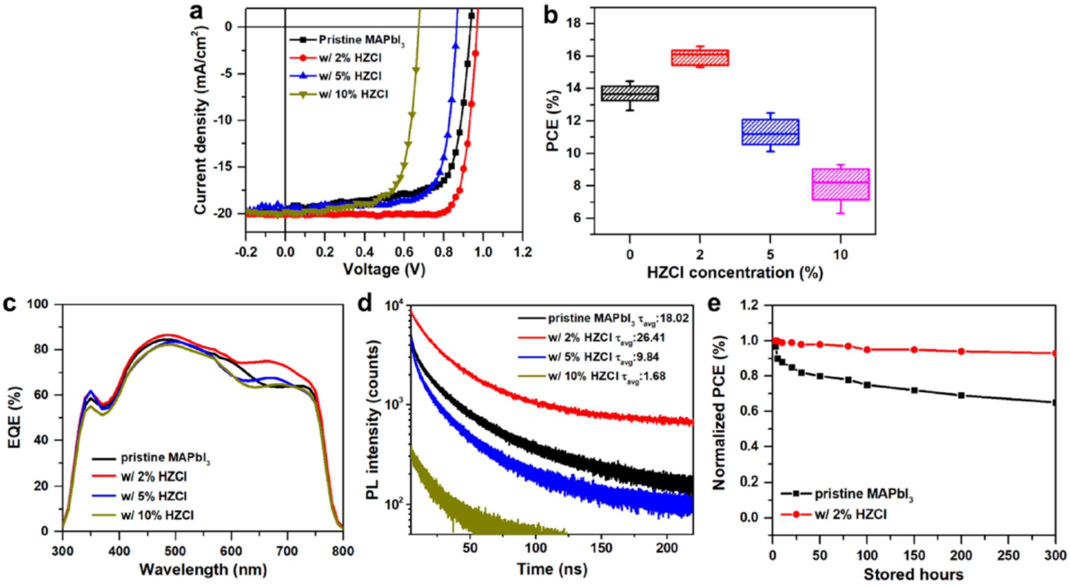

Figure 7: (a) Voltage-current (JV) characteristics of $MAPbI_3$ perovskite device with and without HZCl. (b) PCE of the $MAPbI_3$ perovskite device (c) External quantum efficiency (EQE). (d) Time correlated single photon counting (TCSPC). (e) Device stability of $MAPbI_3$ devices over 300 h. Copyright 2018 American Chemical Society.

The PL decay time of correlated single photon counting (PCSPC) is measured to prove superior carrier life-time with HZCl additive (Figure 7d). The decay time (τ_{avg}) of $MAPbI_3$ with 2 % HZCl additive is 26.41 ns compared to 8.06 ns of pristine $MAPBI_3$. Long τ_{avg} directly supports good charge dissociation and transport in the device.

2.1.5 Conclusion

The A-site cation has not been considered as a main factor of carrier transport, except for the role in the evaluation of structural tolerance of cubic perovskite. Here, we clarified the hidden role of A-site cation in lead halide PSCs in Fröllich polaron picture. From this point of view, we have discovered a design principle that selects appropriate cations for better carrier mobility to boost the efficiency of PSC. The key to steering charge transport is to choose organic cations that increases the strength of the interaction and the number of coordination to I. It is possible to quench the e-ph interactions by increasing the directional $I^- \cdots HN(O)$ halogen-hydrogen bonds or $I^- \cdots Li$ bonds. The vibration mode of the involved molecular cation causes the deterioration of the e-ph interaction. From the first-principles calculation, we calculated the polaron properties of lead iodide PSCs with various kinds of A-site cations.

Organic cations such as HA and LM appear to be very promising for light harvesting as compared to MA and inorganic Cs^+, which are most used at the moment. Most of the hole conductive material (HTM) contains Li^+ ions in lithium bis(trifluoromethylsulfonyl) imide (LiTFSI), so that the LM may form by diffusion of Li ions upon heating. In conclusion, we revealed a new perspective for the role of molecular A-site cations to reduce Fröhlich e-ph coupling of PbI_3 LO vibrations. The proposed design principle can help to find the new prospective A-site molecular cations to promote PCE of lead halide perovskites.

2.2 Rashba-Dresselhaus spin-orbit interactions in LHP interface with graphene and TiO_2

At the interface of non-centrosymmetric crystals or hetero-strucures, the spin-orbit coupling (SOC) field (odd in k (momentum) and time-reversed symmetric) causes spin splitting so called Rashba-Dresselhaus (RD) effect. The effective low order perturbation terms of RD interactions are derived based on the specified symmetry of the model. The lowest order Hamilton in $k\dot{p}$,[6]

$$\mathcal{H}_{RD}(\mathbf{k}) = \alpha_R(\mathbf{k}_x\sigma_y + \mathbf{k}_y\sigma_x) + \alpha_D(\mathbf{k}_x\sigma_x - \mathbf{k}_y\sigma_y) \tag{1}$$

$$\alpha_{RD} = \frac{\Delta E}{2\Delta\mathbf{k}} \tag{2}$$

Here, $\mathbf{k}$ is the momentum, $\sigma_{i=x,y,z}$ is the Pauli spin matrix and the strength of RD interaction is defined by the coupling constant $\alpha_{RD}(eV \cdot \text{Å})$ (Eq. 2). The interaction of RD is common and many systems such as noncentrosymmetric crystal, hetero-junction, metal surfaces, and even graphene exhibit considerable energy splitting. The RD depends on the systems: 0.067 $eV \cdot \text{Å}$ (InAlAs / InGaAs) or 4.0 $eV \cdot \text{Å}$ (Bi_2Se_3).[7, 8] Recently, PSC materials containing heavy elements such as Pb or I have been realized that it can exhibit large RD coupling constants: $\alpha_{RD} \sim 1.6$ ($eV \cdot \text{Å}$) in 2 D PSC $(C_6H_5C_2H_4NH_3)_2PbI_4$ and $\alpha_{RD} \sim 2.75 - 3.75 eV \cdot \text{Å}$ (in the original paper $\alpha_{RD} = \frac{2\Delta E}{\Delta\mathbf{k}}$ with $\alpha_R \sim 7 - 11$) in $MAPbBr_3$ and 3D $CsPbBr_3$ nanocrystals.[9, 10, 11] In past studies on PSC on RD SOC focused on inversion symmetric bulk with artificial conditions such as uniaxial pressure which caused ferroelectricity of PSC. Recent studies revealed the importance of RD effect in the exciton states of PSC.

On the other hand, an interesting aspect is realized in which dynamic Rashba splitting occurs in both centerosymmetric $I4/mcm$ simulated by Car-Parrinello molecular dynamics and non-centrosymmetric $I4cm$ tetragonal phases. It is suggested that the effect of RD may disappear in large ($> 8nm^3$) with large entropy of MA.[12, 13] Application to spin filter devices that cause spin precession in PSC is due to RD interaction. The technical effect of RD SOC is to change the direct band structure to indirect one, suppressing the carrier recombination and promoting the carrier accumulation in the barrier between PSC and charge transporting layers. Understanding the interfacial phenomena of solar cell devices is important, but research on the influence of RD interactions on solar cell performance at the interface of PSC has not been carried out yet.

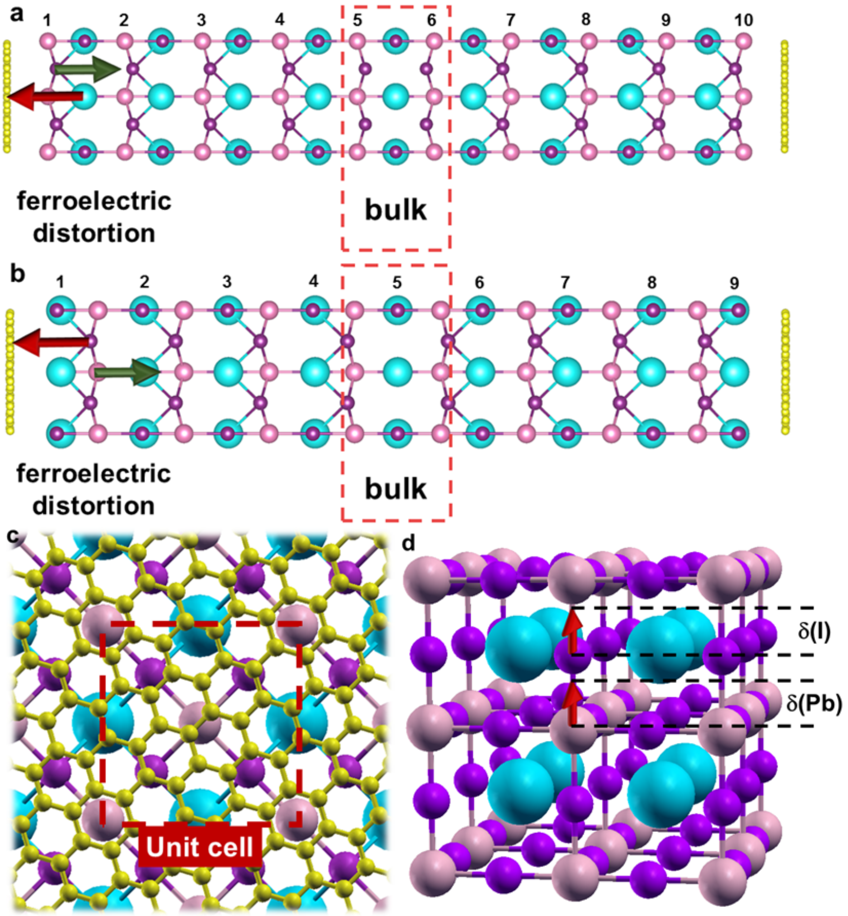

Figure 8: (a) PbI_2 termination and (b) CsI termination of cubic $CsPbI_3$ 10 layers of ($\sqrt{2}\times\sqrt{2}\times1$) interfacing with the graphene (yellow). (c) Schematic for the unit-cell from [001] view. (d) Each PbI_2 layer experiences ferroelectric distortion of Pb (red arrow) and I (green arrow). Copyright 2018 American Chemical Society.

2.2.1 Graphene/$CsPbI_3$ interface

The atomic displacements near the surface are only important [001]. The displacement of the ferroelectric becomes larger at the interface and becomes larger at the interface. Unless the bandgap is closed for overall ferroelectricity, the bulk (or inverse symmetry) layer, the fifth and sixth layers are very important to provide a reasonable band structure.

We created the graphene(Gr)/$CsPbI_3$(001)/graphene interface with the ($\sqrt{2}\times\sqrt{2}\times1$) PbI_2-(CsI-) terminated cubic $CsPbI_3$ with the lattice mismatch of $\sim$ 1.93 % (Figure 8a, b, and c). We have confirmed that the surface dipoles do not affect both the relaxed geometry and the corresponding electronic structure. As reported in the LDA+D2 calculation of the previous Gr/tetragonal-$MAPbI_3$, we observe the ferroelectric strain driven by the attractive force between the cation Pb^{2+} of the PbI_2 terminated slab and graphene. The measured distance of the PbI_2 layer and the graphene (Figure 8a) is 3.21 Å at the PBE+D3 level and is 3.28 Å at the PBE+Tkatchenko-Scheffler(TS) level (LDA+D2 is 3.45 Å).[14] In the case of CsI termination, the distance of the CsI layer graphene (Figure 8b) is $d_{PBE-TS} \sim 3.4$, which is slightly larger than the PbI_2. Despite ferroelectric distortion, the C_{4v} point symmetry of the cubic structure is preserved contrast to the TiO_2/$MAPbI_3$ interface which is described later. The direction of Pb and I displacements (Figure 8 d) are opposite in PbI_2- and CsI-termination. At PbI_2 termination, displacement is $\delta(\mathrm{Pb}) \sim +0.4$ and $\delta(I) \sim -0.6$. At the CsI termination, $\delta(Pb) \sim -0.5$ and $\delta(I) \sim +0.6$. The binding energy (BE) of graphene at PbI_2 termination is 20.5 meV/atom, which is 3.3 times larger than that at the CsI termination (Table 2). The PbI_2-(CsI-) terminated

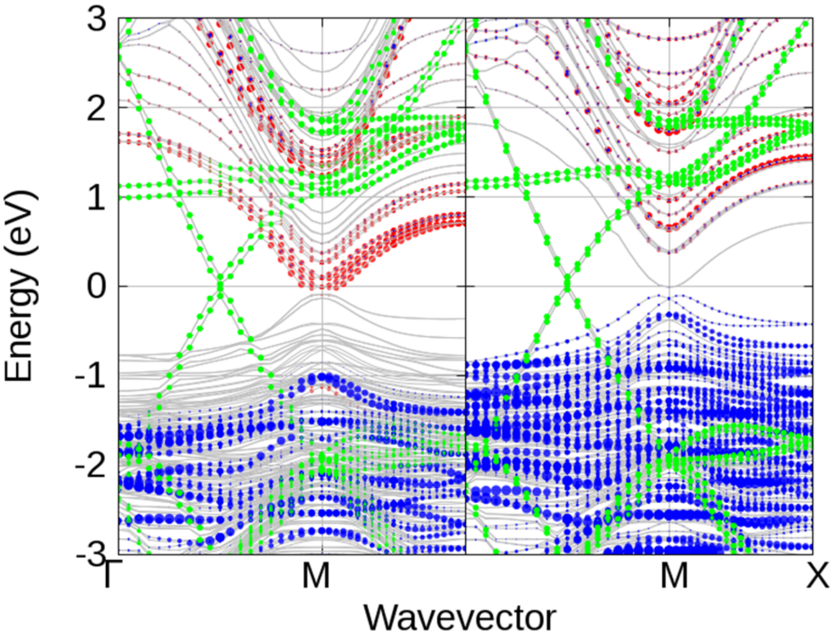

Figure 9: Electronic band structures of PbI_2-terminated (CsI-terminated) Gr/$CsPbI_3$(001)/Gr-(1 × 1) system; Pb (red), I (blue), and graphene (green). Copyright 2018 American Chemical Society.

Gr/$CsPbI_3$(001)/Gr electronic band structure using PBE+TS+SOC (Figure 9) shows some interesting features. Large Rashba SOC interaction gives rise to a splitting of the surface band in momentum k and energy E at both the conduction band (CB) and the valence band (VB). In the case of cube $Pm3m$ (centrosymmetric) $CsPbI_3$, strong SOC splits the conduction band into one $j = 1/2$ and one $j = 3/2$. The valence band has $s-$orbital character, so there is no effective splitting at the highest valence band. However, at the Gr/$CsPbI_3$ interface, the value band at the M of BZ experiences an asymmetric field on the xy plane and its eigenstate becomes $j = 1/2$ instead of $s = 1/2$. The energy barrier between $j_z = -1/2$ and $j_z = 1/2$ is sizable for CB [ΔE(PbI_2-termination) $\sim$ 280 meV]. This large barrier prevents electrons recombining directly with the VB extremum by overcoming the CB extreme barrier.

Gr/$CsPbI_3$(001)/Gr reveals the gap state which has a particular electronic structure compared to an ordinary semiconductor gap states (Figure 9). While the lowest empty surface state at the PbI_2 termination is CBM, the highest occupied surface state is 1 eV less than VBM. In-

Table 2: BE and α_{RD} for graphene- and TiO_2-interfaced PSCs depending on the terminations, PbI_2 and AI, where A is Cs or MA.

Interface	BE (meV/atom)	α_{RD}(CB) (eV·Å)	α_{RD}(VB) (eV·Å)
Gr/$CsPbI_3$/Gr (PbI_2)	20.54	0.42	1.17
Pristine $CsPbI_3$ (PbI_2)	-	0.18	1.00
Gr/$CsPbI_3$/Gr (CsI)	6.23	0.59	0.50
Pristine $CsPbI_3$ (CsI)	-	0.53	0.54
TiO_2/$MAPbI_3$ (PbI_2)	15.64	0.08	0.17
Pristine $MAPbI_3$ (PbI_2)	-	0.78	0.81
TiO_2/$MAPbI_3$ (MAI)	10.33	0.29	0.58
Pristine $MAPbI_3$ (MAI)	-	0.18	0.30

terestingly, the maximum value of VB is made of bulk states without band splitting because of its centrosymmetry. The surface state shows a trend opposite to the CsI termination. The origin of the unique energy level of Gr/$CsPbI_3$(001) can be explained by observing the displacement of ferroelectric distortion on the surface of $CsPbI_3$. It has been found that CsI and the PbI_2-terminated pristine $CsPbI_3$ (001) undergoes similar intrinsic ferroelectric displacements while the geometry relaxation as the hetero-interface. Comparing the relaxed and unrelaxed $CsPbI_3$ slabs, a significant change in energy levels of the surface state is observed. This natural ferroelectric surface distortion suggests the origin of the recent observation of the Rashba splitting of the $CsPbBr_3$ nanocrystals. However, the role of graphene is different for each termination. At the PbI_2 termination, graphene favors ferroelectric distortion and gives α_R =1.17 (CB) and α_R = 0.42 (VB). At CsI termination, it suppresses ferroelectric distortion and the RD effect is equal to or lower (Table 2), α_R = 0.18 (VB) and α_R =1.00 (CB).

2.2.2 $TiO_2/MAPbI_3$ interface

The Rashba effect is present in the $MAPbI_3$: MA^+ organic cation disrupts the inversion symmetry and deforms the PbI subunit. However, this effect is localized by disorientation of MA cations and α_{RD} was measured to vanish on a scale of about 3 nm in length. Previous studies of a tetragonal slab of $MAPbI_3$ showed that the surface reconstruction produced a significant RD effect and that its effect was more pronounced at the PbI_2 termination. We calculated the band structure of the rutile interface $TiO_2/MAPbI_3(001)$ of the PbI_2-(MAI-) termination (Figure 10a and b) and the original slab of cubic $MAPbI_3$ for comparison purpose. Although the bare rutile (001) is not stable, this facet is advantageous for the configuration of the device. As indicated in the $MAPbI_3$ tetragonal slabs, α_{RD} of CB and VB in the cubic $MAPbI_3$ slab are scaled as less than 2 (Table 2). In addition, our results show that the largest RD of the PbI_2-terminated slab, as evidenced by the distortions of the Pb-I bond along [001] $\theta_{Pb-I-Pb} \sim 155.5°$ (PbI_2-termination) and $\theta_{I-Pb-I} \sim 170.4°$ (MAI termination).

At the PbI_2 termination, bonding between $Pb\cdots O_2$ ($d \sim 2.44$) and $Ti\cdots I$ ($d \sim 2.9$) was observed. For MAI-termination, the degree of freedom of orientation of MA was significantly reduced at the $TiO_2/MAPbI_3$ interface due to the presence of short strong hydrogen bonding (SSHB) between H^+ of MA^+ and O^- of TiO_2.[15] In fact, the AIMD simulation shows that the O-H bond at the interface remains intact even at 330 K in cubic phase. In addition, the optimized MA orientation at the interface deforms the PbI sub-network by increasing the bond distance between Pb and the apical I by approximately 0.15 Å. Since the SSHB significantly reduces the MA degree of freedom at the interface, the Rashba effect at the $TiO_2/$ $MAPbI_3$ interface must be more robust than the bulk one of which is known to be local or sub-local. In addition, previous DFT/AIMD simulation studies on stable (101) and (001) anatase interfaces with PSC also confirmed the near-pinning effect of MA orientation at the interface. Therefore, it is universal for various $TiO_2/MAPbI_3$ interface configurations in which a robust RD effect by SSHB is expected.

The energy splitting in CB is quite significant (Figure 10c). This is expected because $MAPbI_3$'s CB is dominated by heavy Pb p states compared to the relatively lighter I at the valence state. On the other hand, at the PbI_2 termination interface, the surface is stabilized *via* PbO_2 and TiI bonds with BE $\sim$ 15.6 meV/atom and the RD effect is suppressed. We also observed the disappearance of a significant distortion along [001] ($\theta_{Pb-I-Pb} \sim 172.1°$). Therefore, $\alpha_{RD} \sim 0.08$ (VB) and ~ 0.17 (CB) at the PbI_2 termination interface are significantly reduced compared to the pristine slab (Table 2). In the MAI termination interface, the short strong hydrogen bonding improves the RD effect, which is ~ 0.29 (VBM) and 0.58 (CBM). Between VBM and CBM, there is also a shift in the momentum as shown by different δk for CBM and VBM, which suppresses recombination and extends the lifetime of the carriers. As in the case of $Gr/CsPbI_3$, the direct band-to-band recombination of $MAPbI_3$ is considerably attenuated at the interface with TiO_2. (Figure 10b) Direct optical measurement and photoemission studies indi-

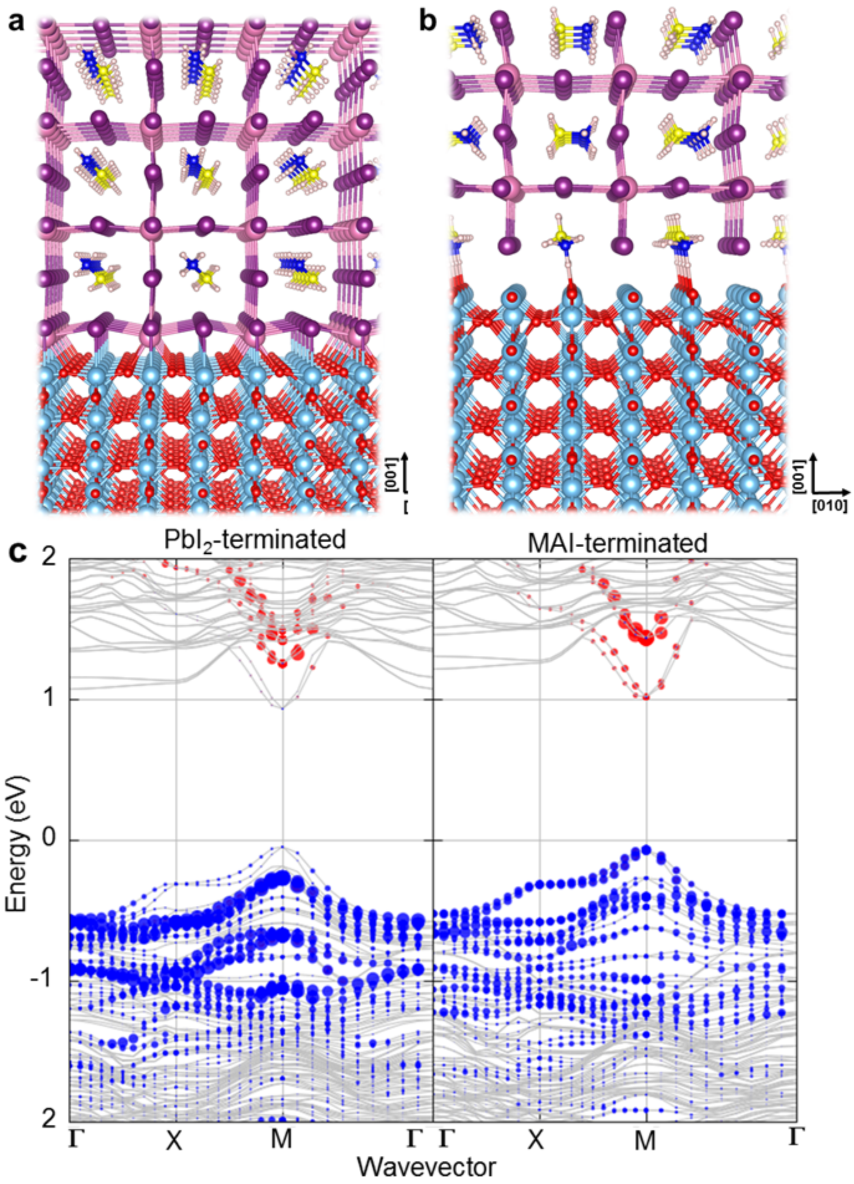

Figure 10: Geometry of (a) PbI_2-terminated (b) MAI-terminated TiO_2/cubic $MAPbI_3$-(001) interface with the presence of SSHB in the MAI_2 termination where Pb(bright red)-O (red) $\sim$ 2.44 Å Ti(light blue)-I $\sim$ 2.90 Å and H(light blue)-O(red) $\sim$ 1.47 Å. (c) The band structure of the optimized TiO_2/$MAPbI_3$ (001) interface with PBE+TS+SOC functional. The blue(red) circle represents the contribution of the surface I(Pb) atoms. Copyright 2018 American Chemical Society.

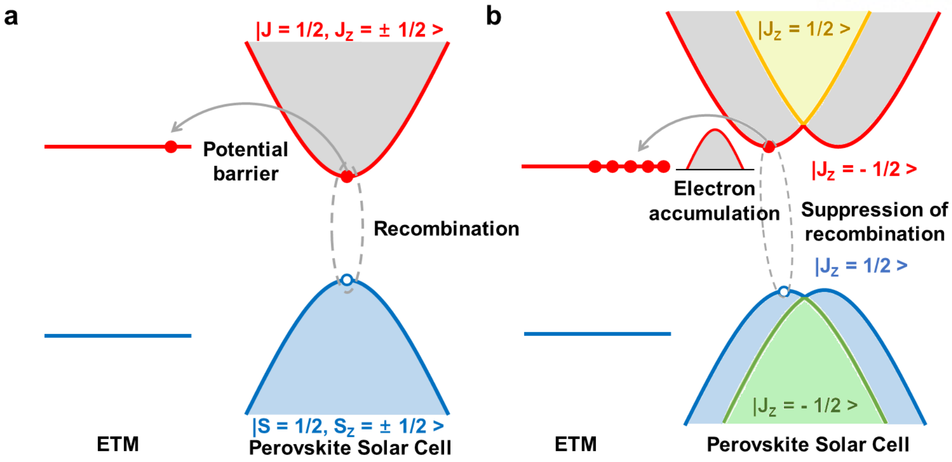

Figure 11: (a) Without the RD effect, the large potential barrier between the PSC and the ETM promotes the rapid electron(red dot)-hole(white dot) recombination process. (b) The RD effect coupled with the accumulation of electrons enables for electron carriers in PSC to overcome by the long lifetime. Copyright 2018 American Chemical Society.

cate that a significant electron transfer barrier of $\sim$ 0.4 eV may be present at the $TiO_2/MAPbI_3$ interface. If such a barrier exists, the process of electron transport is strongly inhibited and electrons should accumulate at the interface. If a charge recombination process is preferred, this should result in a significant reduction in device performance. However, the presence of the Rashba SOC at the interface (Figure 10 and Table 2) reduces such a recombination process (Figure **??**) until the potential barrier is overcame. Therefore, the presence of the Rashba effect at the interface is important to improve the electron transfer process at the $TiO_2/MAPbI_3$ interface.

In addition to the result of 0 K DFT, in order to clarify the influence of the thermal fluctuations, we examined RD using the NVT ensemble based on an AIMD simulation around 600 K (in the case of cubic $CsPbI_3$) and 330 K (in the case of cubic $MAPbI_3$). As the most important case, we studied the PbI_2 termination for $Gr/CsPbI_3/Gr$ and the $TiO_2/MAPbI_3$ termination. The results show that the thermal average of the RD splitting is comparable to the 0 K DFT result (Table 2). The thermal average of α_{RD} (600 K) of PbI_2-terminated $Gr/CsPbI_3$ is 0.46 ($\pm$ 0.15) $eV \cdot$ Å (VB) and 1.25 ($\pm$ 0.54) $eV \cdot$ Å (CB). α_{RD} (330 K) of MAI-terminated $TiO_2/MAPbI_3$, where MA alignment at the TiO_2 interface is fixed, is 0.26 ($\pm$ 0.07) $eV \cdot$ Å (VB) and 0.61 ($\pm$ 0.15) $eV \cdot$ Å . In particular, the configuration of the surface I does not deviate from the 0K configuration even at 330 K due to the fixed MA's orientation (Figure 3b). Therefore, VB has almost the same α_{RD} as 0K DFT and has a slight standard deviation of $\sim$ 0.07 $eV \cdot$ Å.

2.2.3 Conclusion

We show examples of two inorganic/organic perovskite solar cell interfaces, Gr/$CsPbI_3$ which is a promising interface for efficient carrier transport and water protecting layer and TiO_2/$MAPbI_3$ which is a popular electron transport layer interface. In CB [VB] of PbI_2-terminated Gr/$CsPbI_3$, a considerable Rashba SOC α_{RD} (0 K) $\sim$ 1.17 [0.42] $eV \cdot$ Å and α_{RD} (600 K) $\sim$ 1.25 [0.46] $eV \cdot$ Å. At the CB [VB] TiO_2/$MAPbI_3$ interface, there are significant RD interactions α_{RD} (0 K) $\sim$ 0.58 [0.29] $eV \cdot$ Å and α_{RD} (330 K) $\sim$ 0.61 [0.26] $eV \cdot$ Å. The placement of MA at the TiO_2 interface gives a strong and robust RD effect, even at high temperatures ($>$ 330 K) with small deviations. Because of the large SOC nature and the geometric complexity of the PSC, the interface with the other layers brings many phenomena. Successful manipulation of such interfaces could accelerate further improvements in the effectiveness of the PSC.

2.3 Band alignment mechanism of La-doped $BaSnO_3$/$MAPbI_3$ interface

TiO_2 is the most popular ETL material for PSC devices. TiO_2 anatase and rutile both provide high PCE. However, photocatalysis of TiO_2 induced by ultraviolet (UV) radiation causes degradation of the device and a gradual degradation of performance under prolonged UV exposure. Direct optical measurements indicate that there may be an electronic barrier of ~ 0.1 eV at the interface of $MAPbI_3$/TiO_2 and that these large electron barriers accumulate iodine defects in $MAPbI_3$/TiO_2. This can cause I-V hysteresis. In order to overcome these obstacles, the development of efficient and stable the next generation ETL materials has recently appeared. Materials based on metal oxides such as SnO_2, ZnO, WO_3 and $ZnSnO_4$ have attracted attention as a new generation of ETLs.

$BaSnO_3$ (BSO) is known as an indirect broadband semiconductor (for example > 3.1 eV) and has a high electric mobility of 21 to 300 cm^2Vs^{-1} which may have a polaron state.[16, 17] Recent measurements of BSO thin films have made it possible to achieve a conductivity of approximately 10^4Scm^{-1} or more at ambient temperature.[18] The band gap (E_g) of BSO can be easily adjusted by the chemical substitution of Pb, Bi, and La. From the experimental results of hard X-ray photoelectron spectroscopy, this band gap modulation is induced by the interaction between the doping cations and extra-free electrons in the conduction band. Therefore, rather than adjusting the band gap of the PSC by the substitution of cations or halides, BSO can be used to directly adjust the ETL's band gap to ensure optimal band alignment. This scenario is valid for the La-doped $BaSnO_3$ (LBSO) slab as well, as evidenced by the large difference in energy $\sim$ 2 and $4eV$ between the conduction band (Sn-s, O-p states) and La d-state. Since the crystallization temperature of LBSO is 1000°C or even higher, it is very difficult to deposit the LBSO film on a flexible glass substrate. However, recently a new LBSO thin film synthesis method at 500°C or less has been discovered. 5 $mol\%$ of photostable LBSO in the form of ETL ($MAPbI_3$/LBSO) has reached PCE of 22 % or more under illumination for 1000 hours.[19]

2.3.1 PBE0-SOC-D3 functional for bulk $MAPbI_3$ and LBSO

First, bulk cubic $MAPbI_3$ (Figure 12a) and cubic $BaSnO_3$ (Figure 12b) were prepared using the PBE0+SOC functional to accurately describe the experimental bandgap of MAPbI3 (1.5 - 1.6 eV) and BSO (3.1 - 3.5 eV). We observe that $E_{g,PBE0+SOC}(\mathrm{MAPbI_3}) = 1.59$ eV and $E_{g,PBE0+SOC}(\mathrm{BSO}) = 3.51$ (Figure 12a and Figure 12b), thus the PBE0+SOC is the optimal functional (Figure 12b and Figure 12b). It was found that for both materials HSE06+SOC underestimates the band gap, $E_{g,HSE06+SOC}(\mathrm{MAPbI_3}) = 1.03$ eV and $E_{g,HSE06+SOC}(\mathrm{BSO}) = 2.79$ eV. In addition, it can be seen that the BSO band gap is sensitive to the lattice constant $a(\mathrm{BSO})$ (Figure 12c). Therefore, we confirmed that using the experimental in-plane lattice constant $a(\mathrm{BSO}) = 4.09$ Å of the thin film $BaSnO_3$ well reproduce the experimental band gap. Though the conduction band energy level varies considerably by considering the SOC, the energy shift of the conduction band and the valence band in BSO is almost negligible by the inclusion of SOC, $\Delta E_g = 40$ meV.

The band level shift is only desirable in the conduction band, unless the hole carriers can be transported and recombined with electron carriers in the ETL material. In fact, we note that La doping on BSO shifts the energy of the conduction band and leaves the energy of the valence band intact (Figure 12c). For example, The band gap varies as $x = 0$ % (3.51 eV) $> x = 3.7$ % (2.91 eV) $> x = 7.4$ % (2.68 eV) $> x = 11.1$ % (2.55 eV) due to electrostatic interaction between La dopant and doped electrons.

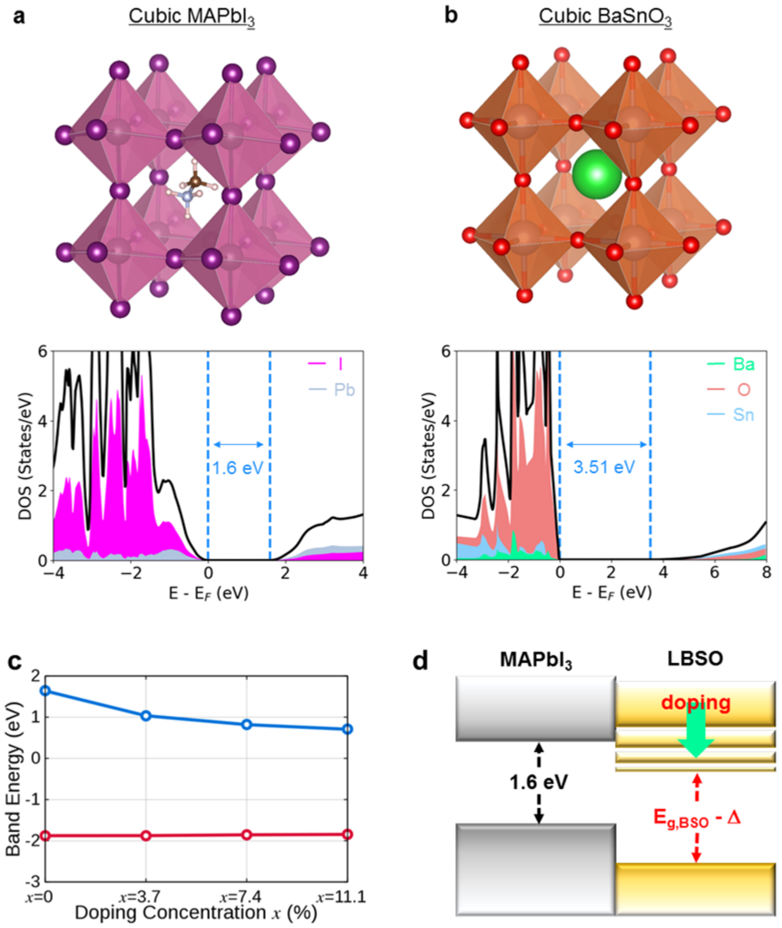

Figure 12: (a) Cubic $MAPbI_3$ perovskite structure and its PBE0+SOC density of states (DOS). (b) cubic $BaSnO_3$ crystal structure and PBE0+SOC DOS. (c) PBE0+SOC band gap change of LBSO with La-doping concentrations $x = 0.0$, 3.7, 7.4 and 11.1 %. The local potential of each system is set to E = 0 eV as a reference. (d) A diagram of band alignment between $MAPbI_3$ and $L_xB_{(1-x)}SO$. Copyright 2018 Royal Society of Chemistry.

2.3.2 LBSO/$MAPbI_3$ interface study

In addition to the renormalization of the band gap, we studied the different interface terminations between LBSO and $MAPbI_3$. Since the bandgap and the band alignment are strongly affected by the termination of the slab, it is essential to conduct calculations on various terminations for a complete understanding of the interface.

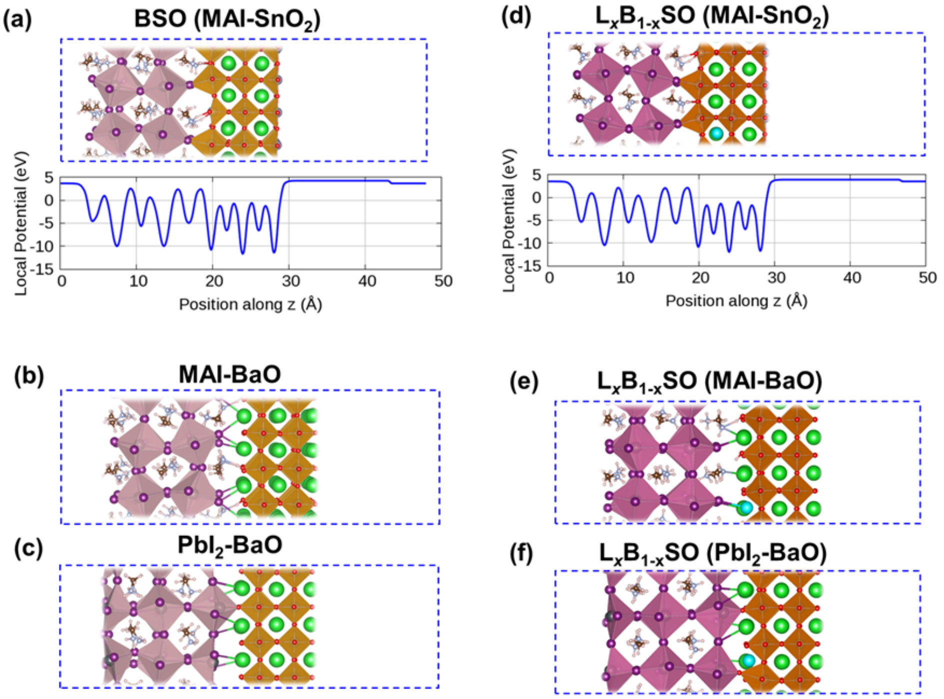

Figure 13: An example of hetero-structure of $L_xB_{(1-x)}SO/MAPbI_3$ ($x = 0.0$ and 3.7 %) (a), (d) MAI-SnO_2, (b), (e) MAI-BaO, (c), (f) PbI_2-BaO. [Pb (gray), I (purple), C (brown) N (sky blue), Sn (silver) O (red), Ba (green), La (cyan)]. Copyright 2018 Royal Society of Chemistry.

For $MAPbI_3$, experimental and DFT studies have shown that the MAI termination is thermodynamically more stable than the PbI_2 termination. However, in the PbI_2 rich condition, a $MAPbI_3$ surface terminated with PbI_2 can also be formed. In previous DFT studies, it has been found that the work function of the MAI is 1 eV lower than the work function of the PbI_2 termination, and that the termination of the $MAPbI_3$ slab plays an important role in the determining of the alignment of the conduction band. The BSO and $MAPbI_3$ interface has four possible interfacial morphologies. We have studied the minimal energy configuration of the interface and the corresponding binding energy E_b including MAI-terminated $MAPbI_3$ and SnO_2-terminated BSO (MAI-BaO) (Figure 13a), MAI-terminated $MAPbI_3$ and BaO-terminated BSO (MAI-BaO) (Figure 13b), and PbI_2-terminated $MAPbI_3$ and BaO-terminated BSO (PbI_2-BaO) (Figure 13c). At the PbI_2 - SnO_2 interface, the PbI_2 interface (in perovskite) becomes unstable and plumbic oxide PbO_2 is formed with the oxygen anion of the SnO_2 termination of BSO. Therefore, at the PbI_2-SnO_2 of LBSO/$MAPbI_3$, the perovskite types of two materials are transformed into lead oxide. It can be seen that this instability persists even when La is doped with BSO. The binding energies per unit cell of $MAPbI_3$/LBSO at all interfaces are large E_b(PbI_2-BaO) = 4.38 eV/unit-cell, E_b(MAI-BaO) = 5.15 eV/unit-cell E_b(MAI-SnO_2) = 4.49 eV/unit-cell, which are larger than the $MAPbI_3$/TiO_2 interface. A high binding energy shows strong hybridization between the interface atoms, and therefore LBSO is considered to have better electron injection property than other ETL materials.

For the MAI termination, the interaction between NH_3 of MA and the oxygen anion depends on the type of LBSO termination. At the SnO_2 termination, there is the short strong hydrogen bond (SSHB) between NH_3 and O, where the proton is shuttling back and forth between adjacent atoms. Since the existence of such strong hydrogen bonds (HB), the interface can further be stabilized and possibly influence the energy level between the interfaces. At the BaO termination, the proton transfer from NH_3 to the oxygen anion is observed. It was also found that a slight La (x = 3.7 %) doping for BSO had little effect on the optimized geometry. The optimized geometry for subsequent doping (x = 7.4, 11.0 %) is almost identical to that of the original case.

Depending on the termination of $MAPbI_3$ and BSO (PbI_2, MAI, SnO_2, and BaO) interface morphology, it will impact on the practical performance of the PSC. However, due to strong hybridization between adjacent interfaces, the original electron densities are rearranged and the expected large dependence on the termination will be eliminated. From the density of state (DOS) of LBSO/$MAPbI_3$ at the PBE level, a considerable hybridization of the interface atoms is observed whatever the type of termination. These hybridizations can also be formed between the conduction and valence states of each adjacent layer (i.e. Sn(BSO) and I($MAPbI_3$)) without affecting the band alignment. A decrease in the energy level of La is observed in the MAI-SnO_2 interface, which underlines that it is independent of the CBM energy level. Therefore, scenarios such as the charge transfer or the energy level shift by induced dipoles are not a dominant factor in explaining the energy level of LBSO/$MAPbI_3$.

2.3.3 Conduction band alignment of LBSO/$MAPbI_3$ with respect to La-doping

Considering that the hybridization is strong in $MAPbI_3$/LBSO, it is important to confirm if it affects the electronic state of La and the minimum of the conduction band (Sn-s state). The presence of hybridization between the two states results in a significant change in the properties of the conduction band and its energy level. For example, in conductive oxides such as Sn- or Ge-doped In_2O_3, dopant ions significantly alter the CBM state by orbital hybridization, resulting in complex bandgap modifications.[20] To confirm the mechanism by which the Coulomb interaction between the La^{3+} dopant and the free electron of the conduction band lowers the band edge energy, the partial density of the states (PDOS) was examined. This mechanism has already been validated explicitly from previous experiments and DFT calculations. We observed that the La d state does not hybridize with the Sn-s state at the interface, whatever the type of termination. At $x = 3.7$ %, the La-d state above the CBM of LBSO is $\sim$ 4 eV (MAI-SnO_2) and $\sim$ 2 eV above (MA-BaO and PbI_2-BaO). This is in agreement with the experiment of the K-edge x-ray absorption spectrum (XAS) in which the La dopant state only hybridizes to the O state, which is $\sim$4 eV higher than the conduction band.[21] The result is in agreement with the other concentration of La-dopings. Even when the La dopant is on the surface of the LBSO slab, we do not observe hybridization between the La and Sn states. Therefore, it is concluded that the downshift of the conduction band energy (renormalization of the band gap) is purely dictated by the electrostatic interaction between the La^{3+} dopant and Sn-s conduction band state.

Without doping, there are large electron barriers in three cases: 0.4 eV (MAI-SnO_2), 0.1 eV (MAI-BaO) and 0.45 eV (PbI_2-BaO). In the case of MAI-BaO, with doping $x = 3.7$ %, only the conduction band level of LBSO is shifted (Figure 14b and f) and the band alignment between $MAPbI_3$ and LBSO becomes favorable for electron transport to LBSO layer. The energy shift is more pronounced by subsequent La-doping at $x = 7.4$ and 11 % (Figure 14c-d and g-h).

For the three interfaces, the band alignment of the band edge state with respect to the La doping concentration x (%) is summarized in Figure 15. For comparison purposes, the system vacuum level has been set to 0 eV. In any case, an undesired alignment of the conduction band between $MAPbI_3$ and BSO can be overcome with a small amount of La-doping. Therefore, as a function of the La-doping x, the optimal La-doping range will be found in order to maximize the open-circuit voltage and the corresponding PCE of the device. Therefore, an additional experimental work will be required to study the optimal La-doping range for the maximum photovoltaic efficiency in PSCs. Related phenomena, such as I-V hysteresis and the accumulation of defects at the $MAPbI_3$/LBSO interface as a function of La-doping are also of interest.

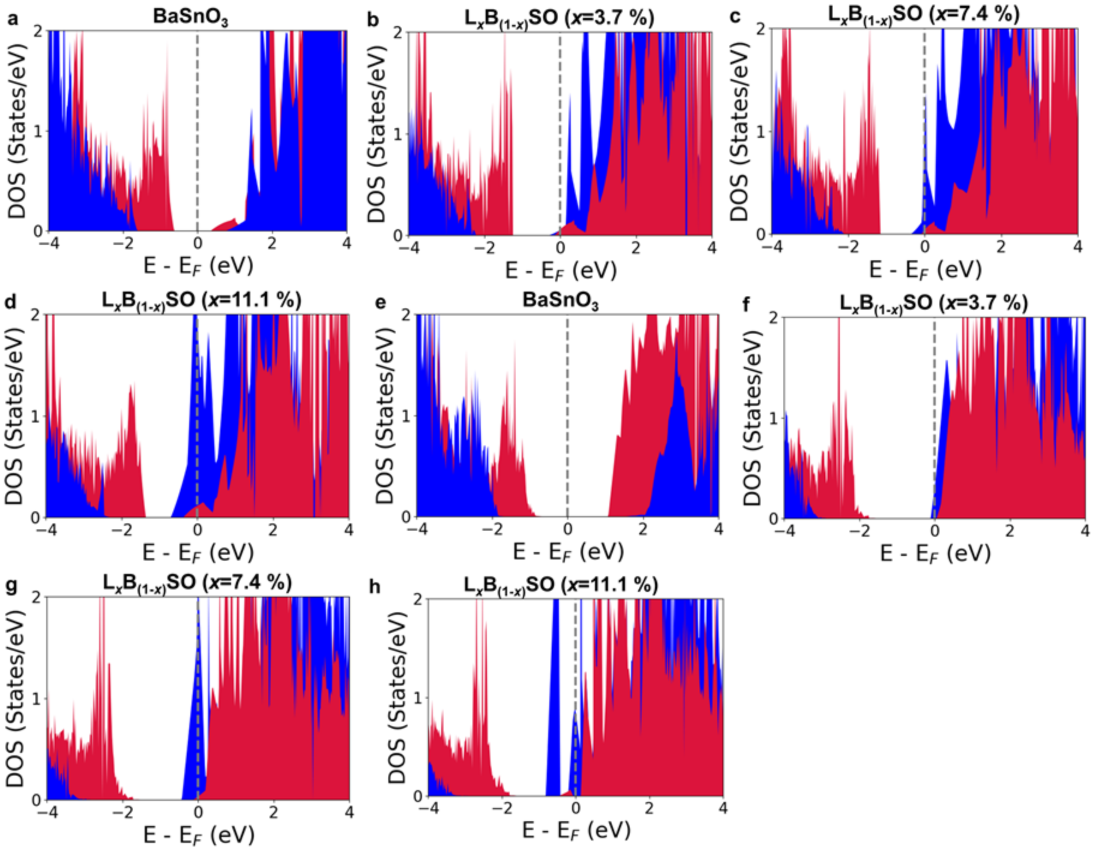

Figure 14: The partial state density (PDOS) of the MAI-SnO_2 terminated $La_xB_{(1-x)}SO_3$/$MAPbI_3$ (x = 0, 3.7, 7.4, 11.1 %) is calculated using PBE0+SOC+D3; (a) x = 0 % (b) x = 3.7 %, (c) x = 7.4 %, (d) x = 11.1 %. PbI_2-BaO terminated $La_xB_{(1-x)}SO_3$/$MAPbI_3$ with La-doping of (e) x = 0 % (f) x = 3.7 %, (g) x = 7.4 % (h) x = 11.1 %; Pb s, p (red) and Sn s, p (blue) states of the interface. Copyright 2018 Royal Society of Chemistry.

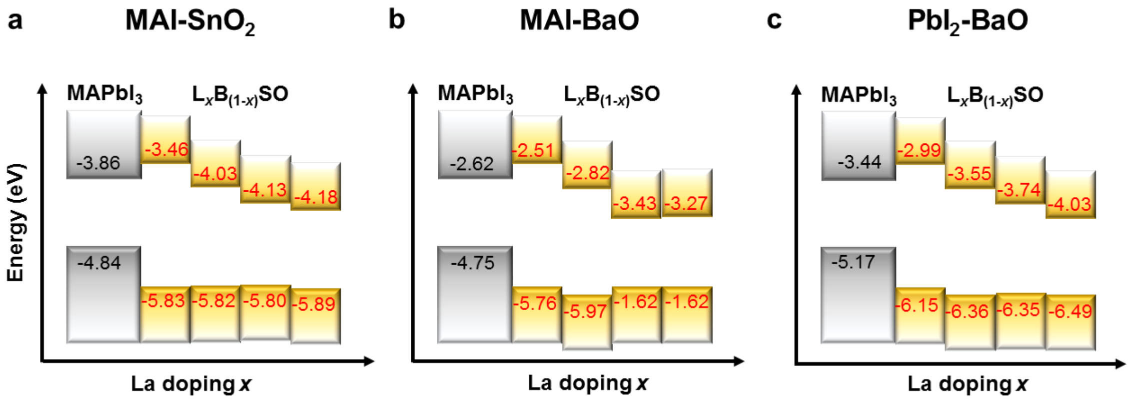

Figure 15: The band alignment of LBSO/$MAPbI_3$ in (a) MAI-SnO_2, (b) MAI-BaO, and (c) PbI_2-BaO with the PBE0+SOC+D3 Copyright 2018 Royal Society of Chemistry.

2.3.4 Conclusion

We investigated the interface between the La-doped $BaSnO_3$ ETL material and the cubic perovskite $MAPbI_3$ solar cell using DFT with (PBE0-corrected-)PBE+SOC+D3. We found that (001) $MAPbI_3$/LBSO forms an "all perovskite" stable interface with large binding energy. Depending on the type of terminations, the SSHB and proton transfer occurs. Since the LBSO can selectively adjust the energy of the conduction band by doping La, it is possible to control the band energy level only through the La-doping without the substitution of halide or organic cation of the PSC. This demonstrates the advantages of LBSO over other ETL materials, in addition to high photostability on UV light. We anticipate that the development of new ETL materials, including LBSO, will further improve the efficiency and stability of lead halide PSC devices.

2.4 Proton-mediated band alignment of TiO_2/$MAPbI_3$

Electron transport material and hole transport material are utilized for the LHP to facilitate the separation of charge (electrons and holes) at each interface in the solar cell device. It is well known that organic cations such as MA in the halide perovskite have the rotational degrees of freedom in the cubic phase, which is the real phase in actual operating conditions of the solar cell. In the bulk $MAPbI_3$, the rotational degrees of freedom of MA has a subtle effect on the electronic structure such as converting the direct band gap into indirect band gap character thus preventing charge recombination. However, the influence of the change in the MA dipole's direction of the TiO_2/perovskite interfacial dynamics has not been sufficiently resolved until now. In particular, it is not yet clear how the interaction with the TiO_2 surface affects the degree of freedom of rotation of MA molecules at the interface. In addition, although the MA state is sufficiently away from the band edge energy, the influence of the MA orientation on the interfacial electronic structure would not be negligible. So we have studied the interface between rutile TiO_2 and cubic $MAPbI_3$ using DFT and *ab initio* molecular dynamics (AIMD) simulations. In order to solve the problem of MA rotation, we use the edge [011], face [100], and the diagonal [111] MA configuration from the latest neutron scattering experiment result. We show that the structural rearrangement of MA at the interface is closely related to the electron transfer process taking place at the TiO2 / MAPbI3 interface unlike the bulk.

2.4.1 The short strong hydrogen bonding in $TiO_2/MAPbI_3$

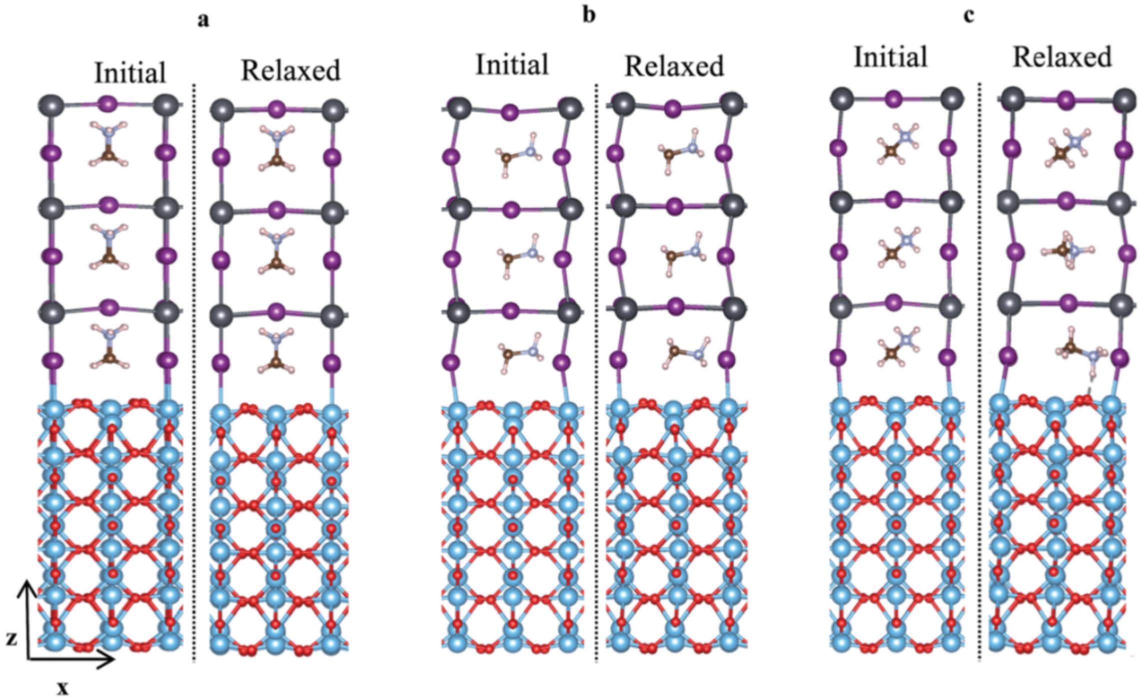

Figure 16: The $TiO_2/MAPbI_3$ interface with (a) edge [011], (b) face [100], and (c) diagonal [111] MA orientation; Ti (blue), Pb (black), I (purple), C (brown), N (light blue), H (white), and O (red). Copyright 2018 Royal Society of Chemistry.

With [011] orientation, the interface has the minimum binding energy suggesting its weak binding. The maximum binding energy for the interface is [111] orientation of MA. The interface of the [100] MA is only 0.18 eV stable than [011] orientation. This difference is much more pronounced for [111] than the comparison of the [100] and [011] interfaces. We note that these energy differences are much higher than the thermal energy thus we expect that the orientation degree of freedom which is present in the cubic bulk phase, is significantly reduced at the interface of TiO_2. Specifically, the C-N axis of the MA preferentially aligns in a way that the NH_3 group coordinates to the underlying TiO_2 by minimizing the $O\cdots H$ distance at the interface (Figure 16).

Hence, the [011] orientation being the NH_3 group completely away from the TiO_2 surface is energetically undesirable despite being a more favorable orientation in the bulk. In addition to the DFT results, we performed the AIMD calculations with the most stable interface structure (Figure 16c) to fully account for the MA dynamics in the cubic phase (330 K). Most importantly, we confirmed that $O\cdots H\cdots N$ hydrogen bonding remains throughout the simulation (the last 15 *ps* of 30 *ps* is used for equilibrium analysis). In contrast to the $MAPbI_3$ bulk, the hydrogen bonding is not fixed in a particular direction, indicating the presence of ordered MA in the $TiO_2/MAPbI_3$ interface (Figure 17).

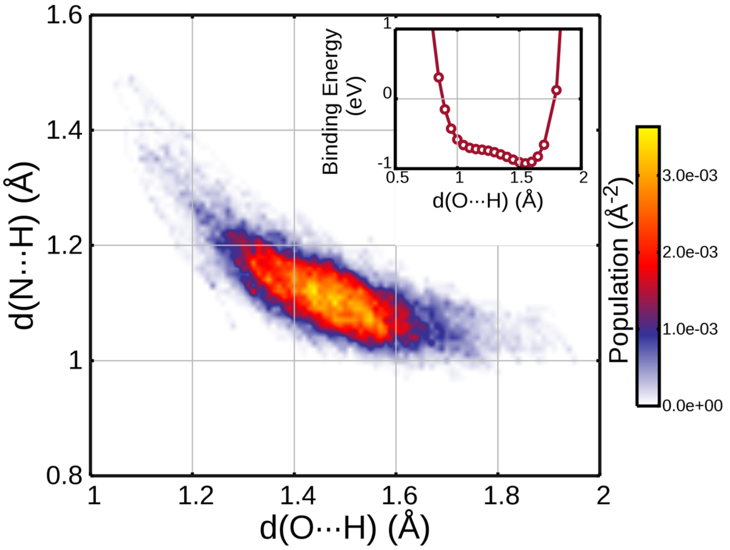

Figure 17: *Ab initio* 2D contour of length $d(\mathrm{O}\cdots\mathrm{H})$ and $d(\mathrm{N}\cdots\mathrm{H})$ in which the broad distribution of bond lengths are present with the average distance of $d(\mathrm{O}\cdots\mathrm{H})$ =1.47 Å and $d(\mathrm{N}\cdots\mathrm{H})$ = 1.15 Å. The binding energy (insertion) for the interaction between the TiO_2 surface and MA represents an anharmonic potential energy surface reflecting the hidden double well minima. Copyright 2018 Royal Society of Chemistry.

2.4.2 Band alignment of $TiO_2/MAPbI_3$

Figure 18 schematically highlights the effect of MA orientation-dependent electronic structure in the electron transfer process at the $TiO_2/MAPbI_3$ interface. The conduction band offset is calculated by HSE06 with the inclusion of the SOC correction. Generally, as a result of light absorption, the electrons are excited into the conduction band in the valence band of $MAPbI_3$. At the $TiO_2/MAPbI_3$ interface, electrons migrate from CB of $MAPbI_3$ to CBM of TiO_2. Thus, the electron transfer of TiO_2 in $MAPbI_3$ is energetically feasible only if the CBM of TiO_2 does not exist at much higher energy than $MAPbI_3$. For the [011] direction, $MAPbI_3$ CBM is significantly lower than TiO_2 (Figure 18a), so electron transfer processes are strongly inhibited by the presence of the energy barrier at the interface. On the other hand, in the case of the optimized structure obtained from the initial [111] orientation, CBM is composed of a mixture of TiO_2 and $MAPbI_3$. This suggests that there is practically no barrier at the interface promoting the electron transfer process (Figure 18c). Therefore, a significant reduction of the electron transport barrier is observed as a result of the MA orientation changing from [011] to [111]. As discussed earlier, the protons (H^+) in the NH_3^+ of MA of this structure is slightly donated to TiO_2 thus H^+ is actually shared by both TiO_2 and $MAPbI_3$. Then, CBM and VBM of TiO2 are lowered by the proximity of the proton (electropositive H). This gives rise to a relatively favorable energy level for the electron transfer process at the interface. Therefore, we emphasize the main qualitative findings of this study. The electron transport barrier at the interface depends on the MA direction. In particular, the barrier is greatly reduced due to the

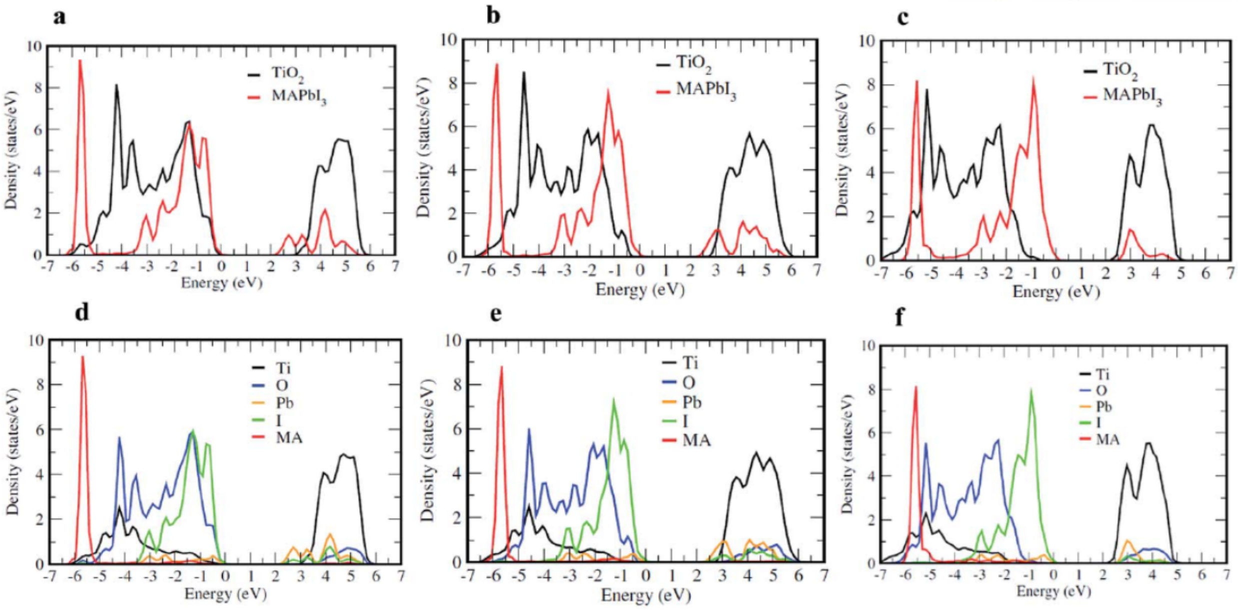

Figure 18: HSE06+SOC total and projected DOS of TiO2/MAPbI3 with (a), (d) face, (b), (e) edge, and (c), (f) diagonal MA orientation. Note the proximity effect of the proton that effectively lowers TiO_2 CB level is plainly observed as [011] → [100] → [111]. Copyright 2018 Royal Society of Chemistry.

optimal interface of the SSHB drive to promote the electron transfer process, and thus solar performance, relative to other energetically undesired orientation.

2.4.3 Conclusion

We found that the orientation degrees of freedom present in the bulk $MAPbI_3$ were significantly reduced at the interface and that the optimal interfacial geometry corresponded to the NH_3 of MA tilted toward surface oxygen through SSHB. More importantly, proton shuttle or SSHB in the optimal MA direction will have a significant impact on the interfacial electronic structure. The energetically optimal interface configuration greatly reduces the energy barrier at the $TiO_2/MAPbI_3$ interface and thus promotes the electron transfer process in the photovoltaic device.

Bibliography

[1] Myung, C. W.; Yun, J.; Lee, G.; Kim, K. S. A New Perspective on the Role of A-Site Cations in Perovskite Solar Cells. *Advanced Energy Materials* **2018**, *8*, 1–7.

[2] Yoon, T.; Kim, G.-H.; Myung, C. W.; Kajal, S.; Jeong, J.; Kim, J. W.; Kim, J. Y.; Kim, K. S. Ambient-Stable Cubic-Phase Hybrid Perovskite Reaching the Shockley–Queisser Fill Factor Limit via Inorganic Additive-Assisted Process. *ACS Applied Energy Materials* **2018**, acsaem.8b01364.

[3] Goldschmidt, V. M. Die Gesetze der Krystallochemie. *Naturwissenschaften* **1926**, *14*, 477–485.

[4] Giustino, F. Electron-Phonon Interactions from First Principles. *Rev. Mod. Phys.* **2017**, *89*, 015003.

[5] Hoffman, J. B.; Schleper, A. L.; Kamat, P. V. Transformation of Sintered $CsPbBr_3$ Nanocrystals to Cubic $CsPbI_3$ and Gradient $CsPbBr_xI_{3-x}$ through Halide Exchange. *Journal of the American Chemical Society* **2016**, *138*, 8603–8611.

[6] Manchon, A.; Koo, H. C.; Nitta, J.; Frolov, S. M.; Duine, R. A. New Perspectives for Rashba Spin–Orbit Coupling. *Nature Materials* **2015**, *14*, 871–882.

[7] Park, Y. H.; Kim, H.-j.; Chang, J.; Han, S. H.; Eom, J.; Choi, H.-j.; Cheol, H. Separation of Rashba and Dresselhaus Spin-Orbit Interactions using Crystal Direction Dependent Transport Measurements Separation of Rashba and Dresselhaus Spin-Orbit Interactions using Crystal Direction Dependent Transport Measurements. *Appl. Phys. Lett.* **2013**, *252407*, 2011–2016.

[8] King, P. D.; Hatch, R. C.; Bianchi, M.; Ovsyannikov, R.; Lupulescu, C.; Landolt, G.; Slomski, B.; Dil, J. H.; Guan, D.; Mi, J. L.; Rienks, E. D.; Fink, J.; Lindblad, A.; Svensson, S.; Bao, S.; Balakrishnan, G.; Iversen, B. B.; Osterwalder, J.; Eberhardt, W.; Baumberger, F.; Hofmann, P. Large Tunable Rashba Spin Splitting of a Two-Dimensional Electron Gas in Bi_2Se_3. *Physical Review Letters* **2011**, *107*, 1–5.

[9] Zhai, Y.; Baniya, S.; Zhang, C.; Li, J.; Haney, P.; Sheng, C.-X.; Ehrenfreund, E.; Vardeny, Z. V. Giant Rashba Splitting in 2D Organic-Inorganic Halide Perovskites Measured by Transient Spectroscopies. *Science Advances* **2017**, *3*, e1700704.

[10] Niesner, D.; Wilhelm, M.; Levchuk, I.; Osvet, A.; Shrestha, S.; Batentschuk, M.; Brabec, C.; Fauster, T. Giant Rashba Splitting in $CH_3NH_3PbBr_3$ Organic-Inorganic Perovskite. *Physical Review Letters* **2016**, *117*, 1–6.

[11] Isarov, M.; Tan, L. Z.; Bodnarchuk, M. I.; Kovalenko, M. V.; Rappe, A. M.; Lifshitz, E. Rashba effect in a single colloidal CsPbBr3 perovskite nanocrystal detected by magneto-optical measurements. *Nano Letters* **2017**, *17*, 5020–5026.

[12] Etienne, T.; Mosconi, E.; De Angelis, F. Dynamical Origin of the Rashba Effect in Organohalide Lead Perovskites: A Key to Suppressed Carrier Recombination in Perovskite Solar Cells? *Journal of Physical Chemistry Letters* **2016**, *7*, 1638–1645.

[13] Mosconi, E.; Etienne, T.; De Angelis, F. Rashba Band Splitting in Organohalide Lead Perovskites: Bulk and Surface Effects. *Journal of Physical Chemistry Letters* **2017**, *8*, 2247–2252.

[14] Volonakis, G.; Giustino, F. Ferroelectric Graphene–Perovskite Interfaces. *The Journal of Physical Chemistry Letters* **2015**, 2496–2502.

[15] Kim, K. S.; Oh, K. S.; Lee, J. Y. Catalytic Role of Enzymes: Short Strong H-Bond-Induced Partial Proton Shuttles and Charge Redistributions. *Proceedings of the National Academy of Sciences of the United States of America* **2000**, *97*, 6373–8.

[16] Lee, S.; Wang, H.; Gopal, P.; Shin, J.; Jaim, H. M.; Zhang, X.; Jeong, S. Y.; Usanmaz, D.; Curtarolo, S.; Fornari, M.; Buongiorno Nardelli, M.; Takeuchi, I. Systematic Band Gap Tuning of $BaSnO_3$ via Chemical Substitutions: The Role of Clustering in Mixed-Valence Perovskites. *Chemistry of Materials* **2017**, *29*, 9378–9385.

[17] Kim, H. J.; Kim, U.; Kim, T. H.; Kim, J.; Kim, H. M.; Jeon, B. G.; Lee, W. J.; Mun, H. S.; Hong, K. T.; Yu, J.; Char, K.; Kim, K. H. Physical Properties of Transparent Perovskite Oxides (Ba,La)SnO_3 with High Electrical Mobility at Room Temperature. *Physical Review B - Condensed Matter and Materials Physics* **2012**, *86*, 1–9.

[18] Prakash, A.; Xu, P.; Faghaninia, A.; Shukla, S.; Ager, J. W.; Lo, C. S.; Jalan, B. Wide bandgap $BaSnO_3$ films with Room Temperature Conductivity Exceeding 10^4 S·cm^{-1}. *Nature Communications* **2017**, *8*, 15167.

[19] Shin, S. S.; Yeom, E. J.; Yang, W. S.; Hur, S.; Kim, M. G.; Im, J.; Seo, J.; Noh, J. H.; Seok, S. I. Colloidally Prepared La-Doped $BaSnO_3$ Electrodes for Efficient, Photostable Perovskite Solar Cells. *Science* **2017**, *356*, 167–171.

[20] Walsh, A.; Da Silva, J. L.; Wei, S. H. Origins of Band-Gap Renormalization in Degenerately Doped Semiconductors. *Physical Review B - Condensed Matter and Materials Physics* **2008**, *78*, 1–5.

[21] Lebens-Higgins, Z.; Scanlon, D. O.; Paik, H.; Sallis, S.; Nie, Y.; Uchida, M.; Quackenbush, N. F.; Wahila, M. J.; Sterbinsky, G. E.; Arena, D. A.; Woicik, J. C.; Schlom, D. G.; Piper, L. F. Direct Observation of Electrostatically Driven Band Gap Renormalization in a

Degenerate Perovskite Transparent Conducting Oxide. *Physical Review Letters* **2016**, *116*, 1–5.

III Heterogeneous single atom catalysts for water splitting

Natural phenomena, including photosynthesis and metabolism of living organisms are mediated by catalytic reactions associated with electron/proton transfer. In recent years, artificial catalysts have been developed for photo-electrolysis/synthesis, energy materials/devices (batteries, fuel cells, water splitting reactions), mechanical devices, *etc.* These chemical reactions are basically electrochemical reactions involving electron/proton transfer.

In general, as the chemical reaction involves electron transfer, any medium involved in the reaction acts as an electrochemical catalyst. As a basic example of an electrochemical reaction, a water splitting is an important reaction to obtain hydrogen energy through water. In a electrochemical cell, the reaction which occurs at the cathode (Eq. 3) is the hydrogen evolution reaction (HER) and the reaction that occurs at the anode (Eq. 4) is the oxygen evolution reaction (OER). And both reactions occur in acid and basic electrolytes.[1]

$$\text{HER:} \qquad 2\text{H}^+ + 2\text{e}^- \rightarrow \text{H}_2. \tag{3}$$

$$\text{OER:} \qquad 2\text{H}_2\text{O} \rightarrow \text{O}_2 + 4\text{H}^+ + 4\text{e}^-. \tag{4}$$

The reactions can be further decomposed into several steps. For instance, in the acid electrolyte, HER is a two electron transfer reaction at the cathode. The first step takes place by discharging a proton in the solution to form an absorbed neutral hydrogen atom (H_{abs}), called the Volmer step (Eq. 5 and 6). The second step happens either through the Tafel reaction (Eq. 7) or the Heyrovsky reaction (Eq. 8) depending on catalysts' configuration, H_{abs} coverage, and electronic property. One of the deterministic factors for being either reaction is the coverage of H_{abs} on the cathode surface.

$$\text{Volmer (acid)}: \qquad \text{H}^+ + \text{e}^- \rightarrow \text{H}_{\text{abs}}. \tag{5}$$

$$\text{Volmer (basic)}: \qquad \text{H}_2\text{O} + \text{e}^- \rightarrow \text{H}_{\text{abs}} + OH^-. \tag{6}$$

$$\text{Tafel}: \qquad 2\text{H}_{\text{abs}} \rightarrow \text{H}_2. \tag{7}$$

$$\text{Heyrovsky}: \qquad \text{H}_{\text{abs}} + \text{H}^+ + \text{e}^- \rightarrow \text{H}_2. \tag{8}$$

In general, the OER is more complex than the HER because (i) it involves 4 electron transfer reactions (ii) transition metal oxide containing various dopants with the complex geometry (iii) polaron formation with strong carrier-lattice interaction.[2, 3] Also, it is considered to be the bottleneck for the entire water splitting process. For instance, in the acid, the four reaction steps are as follows,

$$1\text{(acid)}: \qquad * + \text{H}_2\text{O} \rightleftharpoons \text{OH}^* + \text{H}^+ + \text{e}^-. \tag{9}$$

$$2\text{(acid)}: \qquad \text{OH}^* \rightleftharpoons \text{O}^* + \text{H}^+ + \text{e}^-. \tag{10}$$

$$3\text{(acid)}: \qquad \text{O}^* + \text{H}_2\text{O} \rightleftharpoons \text{OOH}^* + \text{H}^+ + \text{e}^-. \tag{11}$$

$$4\text{(acid)}: \qquad \text{OOH}^* \rightleftharpoons * + \text{O}_2 + \text{H}^+ + \text{e}^-. \tag{12}$$

In the basic electrolyte,

$$1(\text{basic}): \quad * + \mathrm{OH}^- \rightleftharpoons \mathrm{OH}^* + \mathrm{e}^-. \tag{13}$$

$$2(\text{basic}): \quad \mathrm{OH}^* + \mathrm{OH}^- \rightleftharpoons \mathrm{O}^* + \mathrm{H_2O} + \mathrm{e}^-. \tag{14}$$

$$3(\text{basic}): \quad \mathrm{O}^* + \mathrm{OH}^- \rightleftharpoons \mathrm{OOH}^* + \mathrm{e}^-. \tag{15}$$

$$4(\text{basic}): \quad \mathrm{OOH}^* + \mathrm{OH}^- \rightleftharpoons * + \mathrm{O_2} + \mathrm{H_2O} + \mathrm{e}^-.. \tag{16}$$

, where $*$ refers to the active site and OH^* is the neutral OH absorbed onto the active site.

For efficient water splitting, a cathode material with faster turnover frequency and a low overpotential is required. In order to maximize the efficiency of the catalyst, it is necessary to use a precise quantum calculation method in order to enlarge the active surface by making the catalyst small in the form of nanoparticles or single atoms, and to design the ligand and template material for the optimal catalytic reaction. To describe the catalytic reaction, it is necessary to accurately calculate the geometry of the system, the thermodynamic/kinetic properties (free energy (ΔG), acid dissociation constant (pKa), reduction potential), and the electrical conductivity. Also to identify and elucidate the mechanism of the active sites for the desired reaction, an accurate first-principles (or *ab initio*) tool is required.

3.1 Mass transfer effect of cathodic electrons in Pt-N-Graphitic-tube-Fe/Co-Cu

Because mass transfer effect of cathodic electrons to the active site (in traditional electrochemistry language) or simply put the electronic conductivity (σ) of the cathode surface, is important for HER activity, we investigate it using both electrochemical impedance spectroscopy (EIS) and DFT calculations.[4] The resistance of each composite (Nyquist plot in Figure 19) reveals 4.0, 1.8, 2.1, 4.2, and 4.4 Ω, respectively, that GT-1, Pt-GT-1, Pt-GT-2, Pt-GT-4 , and Pt/C. Thus, Pt-GT-1 is much more conductive than Pt/C and fast electron transfer will help fast HER. The work function of the Pt (111) surface is 5.9 eV, the work function of pyridine type N-type doping graphene, graphene, Cu, Co and Fe is 4.5 to 5.0 eV. Thus, the Pt (111) surface tends to be negatively charged, making it possible for the H^+ cations to form H adsorbed on the Pt cathode. In addition, the Fe-Co/Cu component, which is highly conductive, plays an important role ($H^+ + e^- \rightarrow H^*$) in promoting the electron transfer process for recombination of H^+ in the electrolyte with electrons on the cathode.

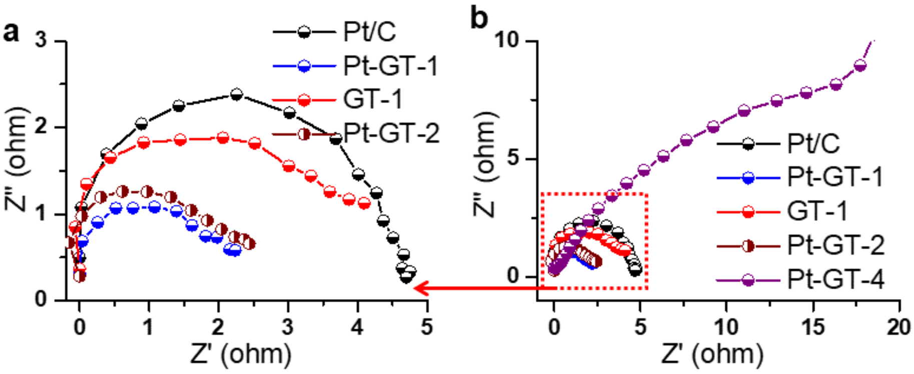

Figure 19: Nyquist plots in 0.1 M $HClO_4$ solution at the potential of -0.301 V (versus SCE) [resistivity ρ: Pt-GT-1 (Cu: Fe3Co7) =1.8 Ω < Pt-GT-2 (Cu: Fe7Co3) =2.1 Ω < GT-1 (Cu: Fe3Co7) =4.0 Ω ≈ Pt/C =4.4 Ω < Pt-Gt-4 (Fe_3Co_7 without Cu) =∼16Ω]. Copyright 2018 Nature Publishing Group.

As described above, the high electrical conductivity of Pt-GT-1 assists in the supply of rapid electron transfer between the electrode and the electrolyte. These negatively charged active sites readily capture H^+ in the electrolyte and rapidly transport electrons through the high conductivity catalyst at the cathode to form H adsorbed on the active site. To understand why the electrons are more active, we compare the conductivity of H-absorbed Pt-N_2C_2/GT, H-absorbed Pt(111) and their mixture using DFT-based Boltzmann's theory (Figure 20). The conductivity of metal H-Pt(111) is calculated to be ∼10 times higher at 298K than for H-(single Pt)-N_2C_2/GT, which has only one conduction channel (weakly hybridized Pt and N_2C_2 around the Fermi energy ($E_F = 0$). Then, the H of a single Pt atomic site with a low distribution and a low conductivity will lead to the Heyrovsky reaction (Tafel slope: ∼50 mV· dec^{-1} for 10 CV cycles deposition of Pt). In contrast, the Pt (111) surface with H is sufficient to form H_2 following the Tafel reaction (Tafel slope: ∼30 mV· dec^{-1}). Therefore, the Pt (111) surface

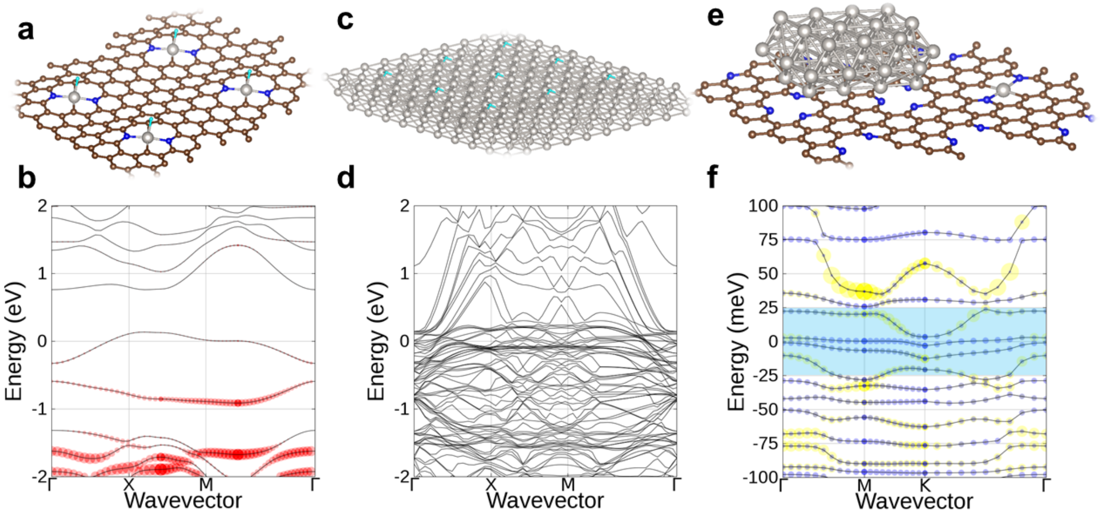

Figure 20: The geometry of (a) H-Pt-N_2C_2/GT, (c) of H-Pt (111), and (e) of H-Pt-N_2C_2/GT+Pt (111);C(brown), N(blue), and H(cyan). The band structure of (b) H-Pt-N_2C_2/GT with a single Pt (red) and GT (gray line) states hybridized, (d) of H-Pt (111) with many conduction channels in the vicinity of E_F, and (f) of H-Pt-N_2C_2/GT+Pt (111) where four channels are available at 298 K (within $|E| < 25$ meV); Pt (111) (blue) and GT (yellow) . We have used the scattering rate $\tau \sim 100\ fs$ for N-doped graphene and $\sim 2.8\ fs$ for Pt metal. The conductivity of H-Pt(111) and H-Pt-N_2C_2/GT+Pt (111) is 9.9 and 7.2 times higher than that of H-Pt-N_2C_2/GT. Copyright 2018 Nature Publishing Group.

shows a faster reaction than the Pt single atom. As more Pt atoms are provided, they grow from a single Pt atom into Pt cluster. The Pt-Pt distance between the Pt atoms and Pt clusters decreases and tends to promote the Tafel reaction. We observe that the number of conductive channels available energy at the room temperature (298 K), $|E - E_F| < 25meV$, is significantly increased by the presence of Pt clusters (conductivity seven times greater than the single Pt atom on GT). Therefore, H^+ in the electrolyte readily captures electrons at a single Pt atomic site (by increasing the conductivity) and forms H^* bound to the C and (single Pt) site, which is then easily separated (ΔG ∼ 0.04 eV) to bind the other H of the adjacent Pt (111) clusters. Therefore, we propose that the single Pt atom and the Pt(111) clusters have synergistic effect to boost the HER.

3.2 X-ray absorption spectroscopy for identification of heterogeneous single atom catalyst systems

Although there has been an explosive experimental progress in the development of single-atom catalyst (SAC) embedded in N-doped graphene supports for HER and ORR, the identification of detailed geometry configuration of SAC has been hampered by the poor resolution of electron microscopy. Core level X-ray absorption fine structure is a useful tool to investigate the composition of elements and identification of bonds between elements. The core excitation can be from 1*s* core electron (K-edge) or 2*p* core electron (especially for transition metals; L_1-, L_2-, and L_3-edge).[5] The K(L or M)-edge XPS provides detailed information for the covalency of ligands, geometry, and composition. For L-edge spectrum, because of strong spin-orbit coupling of core electrons, the time-dependent density function theory (TDDFT) fails.[6] On the other hands, the restricted open-shell configuration singles (ROCIS) can easily include SOC contribution thus appropriate for the high-spin transition metal.[7] Here, we perform TDDFT and DFT/ROCIS calculations to elucidate some of elusive nature of N-doped graphene SAC systems.

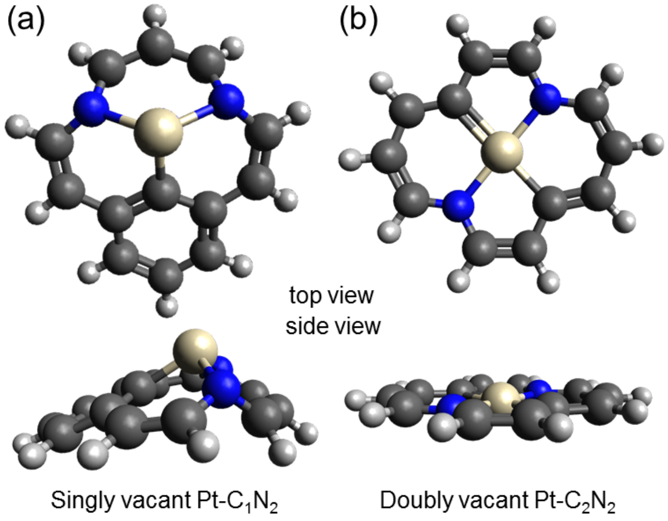

Figure 21: The PBE0-D3/ZORA-def2-TZVP optimized geometry of (a) singly vacant $Pt\text{-}N_2C_1$ and (b) doubly vacant $Pt\text{-}N_2C_2$. Pt, gray; C, black; N, blue; H, white.

As one of the examples of heterogeneous SAC, we investigate single Pt embedded N-doped graphene.[8] Although the planar coordination of Pt by carbon atoms both in single and double vacancies are not possible, the introduction of N in the double vacancy site enalbes the planar coordination because of the shortened C-N bonding around the Pt, which creates more space for the Pt atom to accomodate. The correct electronic structure of Pt-C-N is a nontrivial problem with various possible oxidation states and the noninnocent behavior of C and N ligands. In the case of neutral doubly vacant PtC_4, the simplified electronic configuration is

$(\mathrm{b}_{2u})^2(\mathrm{b}_{3u})^2(\mathrm{a}_u)^2(\mathrm{b}_{2g})^0$ and the LUMO is anti-bonding b_{2g} with Pt d_{xz}.

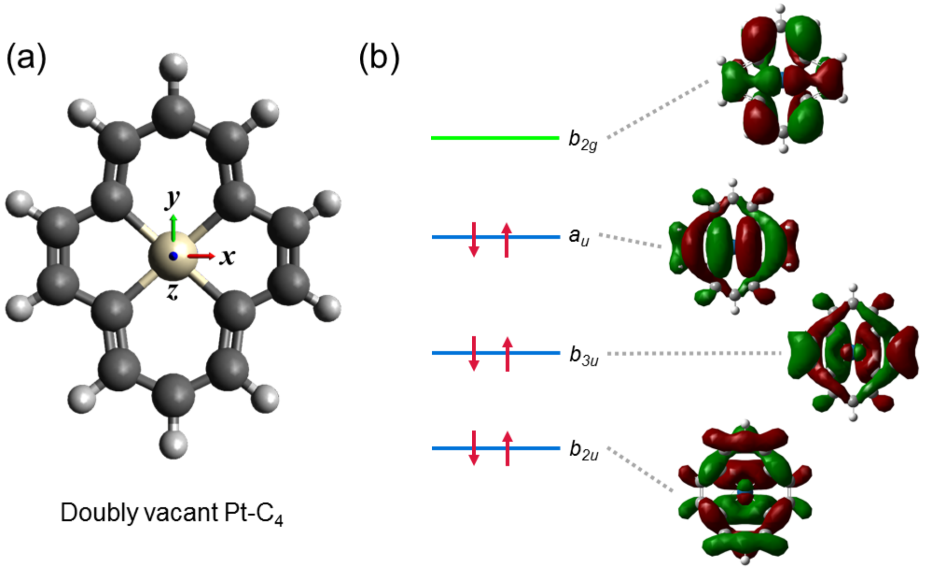

Figure 22: Simplified MO for neutral PtC_4 with spin singlet ground state.

The formation energy is favored as the amount of N-doping increases, which supports the presence of N-metal bondings observed in N-doped graphene SACs.[4] Moreover, we also found that the acidic condition lowers the formation energy of defects. Previous studies found that the $BH^{0.58}LYP$ functional matches well with the experimental C, N, and O K-edge XAS. We found that the $BH^{0.58}LYP$ functional reproduces C-1$s \rightarrow \pi^*$ and σ^* excitation and pyridinic-N (398.9 eV), pyridinic-oxide- (403.2 eV), and quaternary-N (401.4 eV) well.[8, 9] However, there exists a discrepancy for pyrrole which is rather overestimated compared to the experiment.

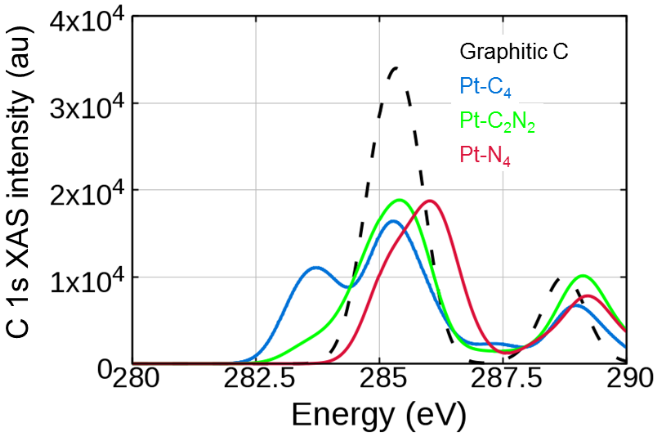

Figure 23: C 1s XAS of doubly vacant Pt with respect to the degree of N-doing at a single Pt site ($PtC_{(4-x)}$-N_x), where $x = 0$(PtC_4; blue), 2(PtC_2N_2; green), and 4(PtN_4; red) compared with the pristine graphitic carbon(dashed black). The core C 1s XAS blueshifts upon N-doping.

We observe that for both singly and doubly vacant PtC_xN_y Pt-C forms the anti-bonding state (dπ) and this state is lower than π^* state in energy. The core excitation of C-1s to Pt-C anti-bonding state lowers K-edge peak. On the other hand, Pt-N tends to blue-shift the K-edge peaks. From the decrease of C K-edge spectrum intensity, we deduce that N-doping tends to disrupt the covalency with the Pt atom.[8]

3.3 Conclusion

Although, heterogeneous single atom catalyst is an ideal platform for the low-cost and efficient water splitting, the reaction mechanism, detailed structure, and design principles are still elusive. We showed that at the atomic limit of the HER catalyst the mass transfer effect of cathodic electrons is an important factor. And this has been largely ignored by the community. Theoretical study of Pt-N-Graphitic-tube-Fe/Co-Cu system proved that its high catalytic activity is due to the synergistic effect of the single Pt atom ($\Delta G \simeq 0$) and Pt cluster (high σ) on N-doped graphitic tube. Also we studied the edge core-level spectroscopy of carbon-based single atom catalyst where transition metal M is coordinated to C and N as $\mathrm{MC}_{(3-x)}\mathrm{N}_x$ ($0 \leq x \leq 3$) or $\mathrm{MC}_{(4-x)}\mathrm{N}_x$ ($0 \leq x \leq 4$). We Used TDDFT and ROCIS for the K- or L-edge XAS spectrum to elucidate the correspondence between XAS and geometry. We expect that our study will provide a valuable reference for the experiment to identify the geometry of single atom catalyst systems.

Bibliography

[1] Vij, V.; Sultan, S.; Harzandi, A. M.; Meena, A.; Tiwari, J. N.; Lee, W. G.; Yoon, T.; Kim, K. S. Nickel-based electrocatalysts for energy-related applications: Oxygen reduction, oxygen evolution, and hydrogen evolution reactions. *ACS Catalysis* **2017**, *7*, 7196–7225.

[2] Lee, J. H.; Hevia, D. F.; Selloni, A. Incorporation of nonmetal impurities at the anatase TiO_2(001)-(1 × 4) surface. *Physical Review Letters* **2013**, *110*, 1–5.

[3] Di Valentin, C.; Selloni, A. Bulk and surface polarons in photoexcited anatase TiO2. *Journal of Physical Chemistry Letters* **2011**, *2*, 2223–2228.

[4] Tiwari, J. N.; Sultan, S.; Myung, C. W.; Yoon, T.; Li, N.; Ha, M.; Harzandi, A. M.; Park, H. J.; Kim, D. Y.; Chandrasekaran, S. S.; Lee, W. G.; Vij, V.; Kang, H.; Shin, T. J.; Shin, H. S.; Lee, G.; Lee, Z.; Kim, K. S. Multicomponent electrocatalyst with ultralow Pt loading and high hydrogen evolution activity. *Nature Energy* **2018**, *3*, 773–782.

[5] Rehr, J. J.; Albers, R. C. Theoretical approaches to x-ray absorption fine structure. *Rev. Mod. Phys.* **2000**, *72*, 621–654.

[6] Runge, E.; Gross, E. K. U. Density-Functional Theory for Time-Dependent Systems. *Phys. Rev. Lett.* **1984**, *52*, 997–1000.

[7] Roemelt, M.; Maganas, D.; DeBeer, S.; Neese, F. A combined DFT and restricted open-shell configuration interaction method including spin-orbit coupling: Application to transition metal L-edge X-ray absorption spectroscopy. *The Journal of Chemical Physics* **2013**, *138*, 204101.

[8] Myung, C. W.; Ha, M.; Kim, D. Y.; Rehr, J. J.; Kim, K. S. Theoretical Study of X-ray Absorption Spectroscopy of Heterogeneous Single Atom Catalysts. **2018**, (in press).

[9] Pels, J.; Kapteijn, F.; Moulijn, J.; Zhu, Q.; Thomas, K. Evolution of nitrogen functionalities in carbonaceous materials during pyrolysis. *Carbon* **1995**, *33*, 1641 – 1653.

IV Graphene/Cu single photon source

Graphene has been extensively studied because of its outstanding electronic properties.[1] However, since its bandgap is zero, graphene is not considered a useful optical material. This is because only inter-band transition is important as observed in noble metals.[2] Surprisingly, the exciton properties of metallic carbon nanotubes were predicted, and the emission enhancement was observed in the experiment.[3] They were explained by the fact that the excitonic effect is much enhanced for the one-dimensional metals.[4] No sharp luminescence has been observed for two-dimensional (2D) materials such as graphene. Although excitons of 2D semi-metallic graphene was predicted, the direct experimental observation was not reported apart from some evidences. Here, we explicitly show that graphene on a Cu surface, which is quasi-two-dimensional systems, can emit the excitonic photoluminescence (PL).[5]

4.1 Identification of strong and sharp excitonic peak from graphene on a Cu

A micro-photoluminescence (μ-PL) spectrum of a graphene sheet synthesized on a Cu(111) surface was measured at an arbitrary position (FIG. 1A). A strong and sharp PL peak near 3.161 eV (the lowest energy emission peak indicated by P) and many peaks around 3.18 eV (indicated by MP) were observed. PL is not visible in the range of 3.1 to 3.22 eV for the original Cu (111) surface and the cleaned Cu (111) surface of the CVD chamber (Fig. 1b). Unlike PL of graphene quantum dot (GQD) and graphene oxide (GO) exhibiting broad emission, a very sharp PL luminescence, which exhibits a half width (FWHM) < 3 meV, was measured. These emissions were not generally observed in graphene and GQD. Asymmetric P-peaks can decompose into two components by fitting the Gaussian function (Figure 24), where two bright lines are reconstructed. The lower energy peak may result from a phonon replica of a higher energy peak involving a phonon energy of $\sim$ 4 meV (described later). The experimental results are verified by the calculation of density function theory (DFT) and density functional perturbation theory (DFPT), *vide infra.* Apart from the above emissions, additional peaks were observed near 3.135 eV (indicated by P-1st) and 3.109 eV (indicated by P-2nd). These peaks are classified as the first and second phonon copy of P with phonon energy of $\sim$ 26 meV.

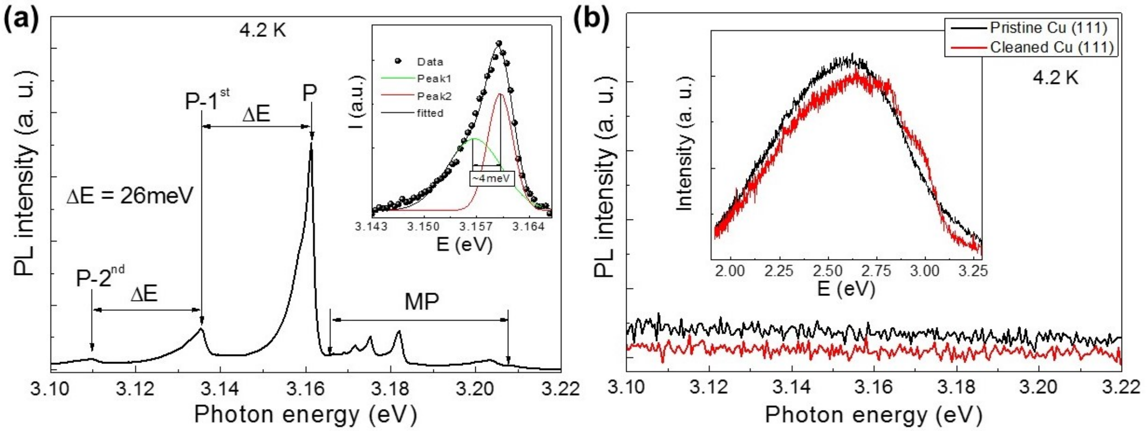

Figure 24: (a) μ-PL spectra of graphene on a Cu (111) measured at 4.2K. The inset shows a PL spectrum reconstructed by P emission using two Gaussian functions. (b) μ-PL spectra of clean Cu(111) surface The inset shows the broad μ-PL spectra. Copyright 2018 American Chemical Society.

4.2 Electronic structure of graphene/Cu

To understand the origin of these peaks, we performed DFT calculations. The geometry optimization of the various stackings show a weak interaction between graphene and Cu, $d > 3.0$ Å, consistent with the expected very weak interaction according to precise CCSD? calculations. Here we use the tophcp stacking configurations. The Dirac band (Figure 25) of graphene (black line) is n-doped (red dot) with a bandgap of 13.5meV DFT (similar to 20meV according to DFT+U).[6] Copper bands include a dispersive *sp* conduction band and a flat *d*-band (blue and green dots). Graphene interacts weakly with copper, but graphene π^* bands are largely perturbed with Cu p_x near **M** of Brillouin zone (BZ). This produces a van Hove singularity (vHs) with a flattened band near the midpoint of the (**M**+**K**) 1.1 eV above the fermi level creating the enhanced density of states (DOS).

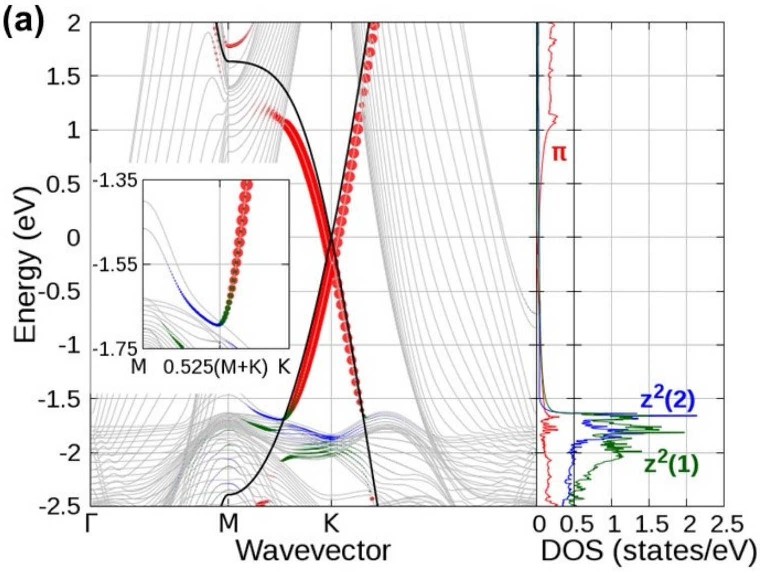

Figure 25: Band structure and projected DOS of graphene/Cu(111); C π-states (red), the 1st layer Cu(1)$d(z^2)$ (green), 2nd layer Cu(2)$d(z^2)$ (blue). Pristine graphene (black) Dirac cone for comparison. An enlarged band structure around 0.525(**M**+**K**) of BZ (inset). Copyright 2018 American Chemical Society.

At the valence band, the $d(z^2)$ band (near -1.6 eV) significantly hybridizes with the π band of graphene. The DOS enhancements for these electrons and holes are responsible for the sharp excitonic emission because of (i) a sizable hybridization between π^* and Cu $d(z^2)$ orbitals; (ii) optical selection rules; and (iii) no momentum change (direct transition).

4.3 Phonon replica of graphene/Cu PL and its sizable electron-phonon interactions in graphene/Cu

The possibility of lattice vibration causing asymmetric P-line and P-replica was investigated using DFPT for the phonon dispersion of graphene on 5 Cu (111) layers. The phonon dispersion (Figure 26a) shows well-known characteristics of graphene ZO and LO branches with phonon softening induced by interfacial mixing (charge transfer) of graphene π orbitals and metallic d orbitals. However, graphene LO mode is very small, the Raman G-band was almost identical to the original graphene one. Though the orbital hybridization of graphene and Cu causes a finite Γ-ZA energy, no ZA/ZO splitting in **K** is observed, thus the adsorption of graphene on the Cu substrate is not very significant. Because the phonon replica excitation energy is $\sim$ 10 meV, we investigated electron-phonon coupling for a low-energy mode with 9 Cu layers. This low energy mode is mostly occupied by Cu optical mode and graphene acoustic mode. The observed PL was assumed to be a direct transition. Graphene phonon DOS shows hybridization between the Cu substrate and the carbon atom of ZA mode near Γ of BZ and has a peak at 3.65 meV (Figure 26b). In addition, the electronic structure calculation shows a large energy change of π^* due to the modulation along the ZA mode. Large energy level shifts in DFT calculations represent large electron-phonon coupling. Therefore, we conclude that the high-density graphene-ZA mode creates an asymmetric P-line consisting of consecutive overlapping Gaussian peaks with 3.65 meV energy splitting. The coupling of the conduction band and the graphene Γ-ZA mode shows the origin of the linear increase in FWHM with temperatures. Meanwhile, the Cu layer atoms of the top layer of the first layer Cu(1) and the second layer Cu(2) in the low energy mode region (Figure 26) are related to the electronic structure of the system. The Cu(2) out-of-plane vibrational mode Γ-SV2[7] has an energy of 30 meV and is comparable to the energy change of 26 meV of P replication. Modulating the mode Γ-SV2 modifies the electron energy level of Cu(2) d_{z^2} by a significant amount. Thus, the P-1st and P-2nd are probably phonon emissions on the Cu surface. The thermal dependence of the emission line-width due to the exciton-phonon interaction is given by:

$$\Gamma(T) = \Gamma_0 + \sigma T + \gamma_{LO} e^{-\frac{E_{LO}}{k_B T}}, \tag{17}$$

where Γ_0 is a temperature independent broadening as T → 0 K, and for P emission, Γ_0 is 2.9 meV. The last two terms are related to homogeneous broadening due to exciton-phonon interaction, where σ is the coupling coefficient between the exciton and the acoustic phonon, and γ_{LO} is the coupling coefficient between the exciton and the longitudinal optical (LO) phonon. The fitting parameters of Eq. 8 give $\sigma = 313.6$ μV/K, which is much higher than values commonly reported for semiconductor materials with similar transition energies, such as InGaN quantum dots (QD) (1.7 μV/K), CdSe nano-sheets (9.8 μ eV/K), and GaN QD (0.8 μ V/K).[8, 9, 10] This means that the out-of-plane acoustic phonon is dominating over the optical phonon.

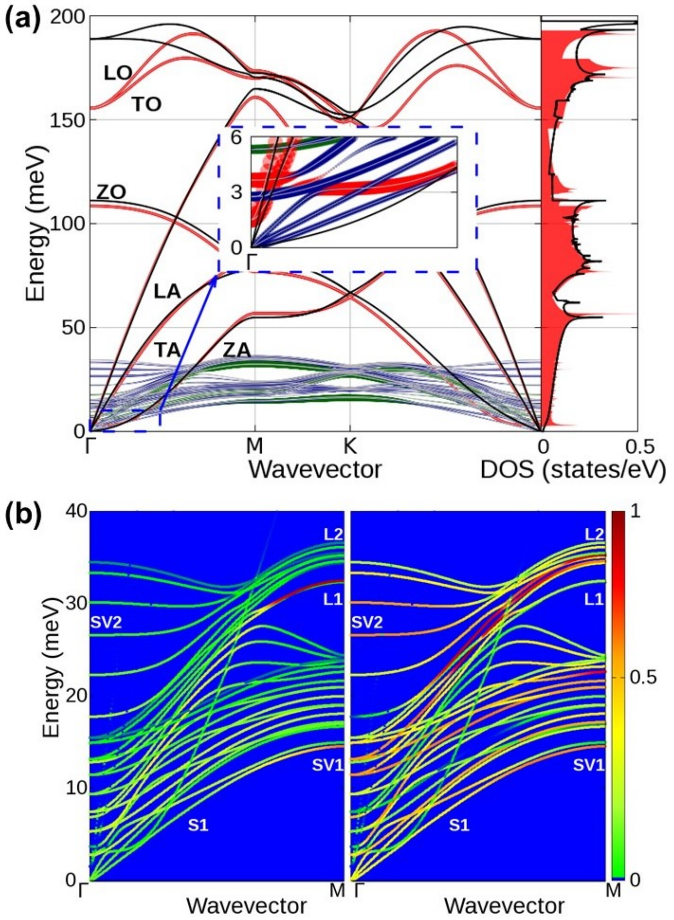

Figure 26: (a) Phonon dispersion of 5 layers of Cu(111)-graphene, graphene (red), the 1st Cu layer (green), 2nd layer Cu (blue), and pristine graphene (black) with the projection of dynamical matrix. The dotted blue box represents the low-energy mode associated with the electron-phonon coupling. (b) Phonon dispersion and phonon DOS in low energy graphene modes of 9 layer Cu (111) graphene. (c) Normalized dynamic matrix projected phonon dispersion of 9-layer Cu (111) graphene on the 1st (left) and 2nd (right) Cu layers near Γ. The surface Cu phonon is composed of the shear vertical (SV) and longitudinal (L) modes of the Cu atoms of the 1st and 2nd layer. Copyright 2018 American Chemical Society.

4.4 Conclusion

Exciton photoluminescence is reported in the graphene sheet grown on Cu surface. A strong and sharp bright PL was clearly observed near 3.16 eV (P) and near 3.18 eV (MP). This emission blue-shifts as the temperature increases, indicating a negative thermal coefficient of graphene. Orbital hybridization of graphene and a Cu surface d orbitals gives rise to a sharp vHs coupled to the large optical transition probability at the saddle point of $0.525(\mathbf{M}+\mathbf{K})$ of BZ. The strong electron-phonon coupling of graphene on Cu (111) is observed with temperature-dependent PL FWHM and DFT/DFPT calculations.

Bibliography

[1] Liu, M.; Yin, X.; Ulin-Avila, E.; Geng, B.; Zentgraf, T.; Ju, L.; Wang, F.; Zhang, X. A Graphene-Based Broadband Optical Modulator. *Nature* **2011**, *474*, 64–67.

[2] Mooradian, A. Photoluminescence of Metals. *Phys. Rev. Lett.* **1969**, *22*, 185–187.

[3] Spataru, C. D.; Ismail-Beigi, S.; Benedict, L. X.; Louie, S. G. Excitonic Effects and Optical Spectra of Single-Walled Carbon Nanotubes. *Phys. Rev. Lett.* **2004**, *92*, 077402.

[4] Brus, L. Size, Dimensionality, and Strong Electron Correlation in Nanoscience. *Accounts of Chemical Research* **2014**, *47*, 2951–2959.

[5] Park, Y.; Kim, Y.; Myung, C. W.; Taylor, R. A.; Chan, C. C.; Reid, B. P.; Puchtler, T. J.; Nicholas, R. J.; Singh, L. T.; Lee, G.; Hwang, C. C.; Park, C. Y.; Kim, K. S. Two-Dimensional Excitonic Photoluminescence in Graphene on a Cu Surface. *ACS Nano* **2017**, *11*, 3207–3212.

[6] Frank, T.; Gmitra, M.; Fabian, J. Theory of Electronic and Spin-Orbit Proximity Effects in Graphene on Cu(111). *Phys. Rev. B* **2016**, *93*, 155142.

[7] Benedek, G.; Bernasconi, M.; Chis, V.; Chulkov, E.; Echenique, P. M.; Hellsing, B.; Toennies, J. P. Theory of Surface Phonons at Metal Surfaces: Recent Advances. *Journal of Physics: Condensed Matter* **2010**, *22*, 084020.

[8] Zakharchenko, K. V.; Katsnelson, M. I.; Fasolino, A. Finite Temperature Lattice Properties of Graphene beyond the Quasiharmonic Approximation. *Phys. Rev. Lett.* **2009**, *102*, 046808.

[9] Achtstein, A. W.; Schliwa, A.; Prudnikau, A.; Hardzei, M.; Artemyev, M. V.; Thomsen, C.; Woggon, U. Electronic Structure and Exciton-Phonon Interaction in Two-Dimensional Colloidal CdSe Nanosheets. *Nano Letters* **2012**, *12*, 3151–3157.

[10] Amloy, S.; Yu, K. H.; Karlsson, K. F.; Farivar, R.; Andersson, T. G.; Holtz, P. O. Size Dependent Biexciton Binding Energies in GaN Quantum Dots. *Applied Physics Letters* **2011**, *99*, 251903.

V Derivation of nonequilibrium Anderson impurity model on the Keldysh contour with one crossing approximation

5.1 Green's functions on the Keldysh contour

We briefly discuss the property of the response and the correlation functions which are naturally connected to the concept of Green's function. In general, the response function of the system is defined

$$\chi^R_{AB}(\mathbf{r},t;\mathbf{r}',t') = \frac{i}{\hbar}\langle[B(\mathbf{r},t),A(\mathbf{r}',t')]\rangle\theta(t-t') \tag{18}$$

$$\chi''_{BA} = \frac{1}{2\hbar}\langle[B(\mathbf{r},t),A(\mathbf{r}',t')]\rangle \tag{19}$$

This definition leads to the Kramers-Kronig relation.

$$\chi^R_{AB}(\mathbf{r},t;\mathbf{r}',t') = 2i\chi''_{BA}\theta(t-t') \tag{20}$$

The symmetry of the χ''_{AB} is useful to find a simplified analytic property of the correlation functions. Under the time-reversal symmetry operator $\hat{K}$ (or the complex conjugate $*$), the position operator $\hat{O}$ is $\langle\hat{K}\hat{O}\hat{K}\rangle = \langle\hat{O}^{\dagger *}\rangle = \epsilon^t\,\langle\hat{O}^{\dagger}\rangle$ where the signature for the time-reversal $\epsilon^t = 1$. From the time-reversal symmetry $\chi''_{A_iA_j}(\omega) = \chi''_{A_jA_i}(\omega)$ and the Hermicity $\chi''_{A_iA_j}(\omega) = [\chi''_{A_jA_i}(\omega)]^*$,

$$\mathrm{Im}[\chi^R_{AB}(\omega)] = \chi''_{AB}(\omega) \tag{21}$$

And Eq. (21) will be used for the derivation of the impurity $\mathcal{G}^{imp}$ in Section 5.7.

Because of the breakdown of the Gell-Mann and Low theorem,[1] the usual diagrammatic treatment of the quantum field theory invented by R. P. Feynmann[2] is no longer applicable. Later, L. V. Keldysh[3] has popularized the deformed contour (or the Keldysh contour $\mathcal{C}_{\mathcal{K}}$) technique to remedy the problem by introducing an additional branch for time-integration of the diagram and by expanding the one-particle correlation function (or the Green's function, $\mathcal{G}$) in the matrix form (Eq. 32). On $\mathcal{C}_{\mathcal{K}}$, the one particle green's function $\mathcal{G}$ can be represented in the six types of $\mathcal{G}$ (Eq. 23-30). However, as becoming apparent in the later discussion, only three of them are independent and the rest are connected in the analytic form (Eq. 27-30) in the Keldysh contour.

The definition of $\mathcal{G}$ is related to the ordering of the creation(or anhalliation) operator $d_\sigma(d^\dagger_\sigma)$ on the contour. For a specific purpose, here in this thesis, d_σ refers to the impurity operator. A conventional definition of the time-ordered Green's function $\mathcal{G}^t$ which is typically useful for equilibrium solutions is

$$G^t_\sigma(\tau_1-\tau_2) = \langle\hat{T}d_\sigma(\tau_1)d^\dagger_\sigma(\tau_2)\rangle\,. \tag{22}$$

where τ is the imaginary time it and σ is the fermionic spin.

In the steady state, the time integration contour is $\mathcal{C_K}$, where $\mathcal{C}_K(-\infty,-\infty) = \mathcal{C}_1 + \mathcal{C}_2$ and the imaginary time formalism is no longer applicable, and the time variable becomes real quantity, $\tau_1 \to t_1$. Also note that the time variables should be ordered not only according to the time ordering, but also to the branch it sits. Or simply the ordering can be made along the contour direction (and this is the simplest way to define $\mathcal{G}$ through the whole chapter). Thus, depending on the branch ($\mathcal{C}_1$ or $\mathcal{C}_2$, which is later than $\mathcal{C}_1$) and corresponding order of the time variables, we can define four different Green's functions $\mathcal{G}(t_1, t_2)$. The lesser(or greater) $\mathcal{G}$ carries the information on the occupancy of the impurity. Here are the example of the four $\mathcal{G}$ for the fermions(+) and bosons(−).

$$\mathcal{G}^<(t_1 - t_2) = (\pm)i\left\langle d^\dagger(t_2)d(t_1)\right\rangle \qquad t_1 \in \mathcal{C}_1,\ t_2 \in \mathcal{C}_2 \tag{23}$$

$$\mathcal{G}^>(t_1 - t_2) = -i\left\langle d(t_1)d^\dagger(t_2)\right\rangle \qquad t_1 \in \mathcal{C}_2,\ t_2 \in \mathcal{C}_1 \tag{24}$$

$$\mathcal{G}^t(t_1 - t_2) = -i\big(\theta(t_1 - t_2)\left\langle d(t_1)d^\dagger(t_2)\right\rangle \mp \theta(t_2 - t_1)\left\langle d^\dagger(t_2)d(t_1)\right\rangle\big) \qquad t_1, t_2 \in \mathcal{C}_1 \tag{25}$$

$$\mathcal{G}^{\bar{t}}(t_1 - t_2) = -i\big(\theta(t_2 - t_1)\left\langle d(t_1)d^\dagger(t_2)\right\rangle \mp \theta(t_1 - t_2)\left\langle d^\dagger(t_2)d(t_1)\right\rangle\big) \qquad t_1, t_2 \in \mathcal{C}_2 \tag{26}$$

And we can easily relate the time-ordered(t), anti-time-ordered($\bar{\text{t}}$), greater(>), and lesser(<) $\mathcal{G}$ to the retarded and advanced $\mathcal{G}$,

$$\mathcal{G}^R = \quad \mathcal{G}_t - \mathcal{G}^< = \mathcal{G}^> - \mathcal{G}_{\bar{t}} \tag{27}$$

$$\mathcal{G}^A = \quad \mathcal{G}_t - \mathcal{G}^> = \mathcal{G}^< - \mathcal{G}_{\bar{t}} \tag{28}$$

$$\mathcal{G}^R(12) = \quad \theta(12)(\mathcal{G}^>(12) - \mathcal{G}^<(12)) \tag{29}$$

$$\mathcal{G}^A(12) = \quad \theta(21)(\mathcal{G}^<(12) - \mathcal{G}^>(12)) \tag{30}$$

where we simplified the time notation, $t_1, t_2 \to 1, 2$. Below table(Table 3) shows some physical meanings of $\mathcal{G}$. In the equilibrium, Green's functions are all dependent and fundamentally connected by a rigid relation called the fluctuation-dissipation relation (Eq. 31). The thermal fluctuations of a fermionic particle is the result of the dissipation weighted by its distribution.

Table 3: The definition and physical meaning of Green's functions $\mathcal{G}$.

$\mathcal{G}$	definition	physical meaning
$\mathcal{G}^<(t)$	$+i\langle d^\dagger(0)d(t)\rangle$	occupied state (static)/fluctuation
$\mathcal{G}^>(t)$	$-i\langle d(t)d^\dagger(0)\rangle$	unoccupied state (static)
$\mathcal{G}^R(t)$	$-i\theta(t)\langle\{d(t), d^\dagger(0)\}\rangle$	causal dynamic spectrum/dissipation
$\mathcal{G}^A(t)$	$+i\theta(-t)\langle\{d(t), d^\dagger(0)\}\rangle$	anti-causal dynamic spectrum

$$\mathcal{G}^>(\omega) = 2\hbar[f_{FD}(-\omega)]\mathrm{Im}\{\mathcal{G}^R(\omega)\} \tag{31}$$

The Dyson equation on the Keldysh contour is expressed as the product of (2×2) $\mathcal{G}$ and Σ matrices

$$\tilde{\mathcal{G}} = \begin{pmatrix} \mathcal{G}_t & -\mathcal{G}^{<} \\ \mathcal{G}^{>} & -\mathcal{G}_{\bar{t}} \end{pmatrix}, \tilde{\Sigma} = \begin{pmatrix} \Sigma_t & -\Sigma^{<} \\ \Sigma^{>} & -\Sigma_{\bar{t}} \end{pmatrix} \tag{32}$$

and

$$\tilde{\mathcal{G}}(x_1, x_2) = \tilde{\mathcal{G}}_0(x_1, x_2) + \int dx_3 \int dx_4 \tilde{\mathcal{G}}_0(x_1, x_3)\tilde{\Sigma}(x_3, x_4)\tilde{\mathcal{G}}(x_4, x_2) \tag{33}$$

Closed Dyson equations for each $\mathcal{G}$ in the frequency domain from the above matrix form (Eq. 32) is

$$G^R(\omega) = G_0^R(\omega)[1 + \Sigma^R(\omega)G^R(\omega)] \tag{34}$$

$$G^A(\omega) = G_0^A(\omega)[1 + \Sigma^A(\omega)G^A(\omega)] \tag{35}$$

$$G^{<}(\omega) = G^R(\omega)\Sigma^{<}(\omega)G^A(\omega) \tag{36}$$

$$G^{>}(\omega) = G^R(\omega)\Sigma^{>}(\omega)G^A(\omega) \tag{37}$$

The matrix form of $\mathcal{G}$ drastically simplifies the analytic continuation (or the Langreth theorem) on $\mathcal{C}_K$. We can consider the Dyson equation of correlation functions $A, B,$ and C on $\mathcal{C}_K$, $C(1,2) = \int_{\mathcal{C}} d\tau A(1,\tau)B(\tau,2)$, in the matrix product form and a simple matrix algebra yields the analytic continuation on the real time axis.

$$\begin{pmatrix} C_t & -C^{<} \\ C^{>} & -C_{\bar{t}} \end{pmatrix} = \begin{pmatrix} A_t & -A^{<} \\ A^{>} & -A_{\bar{t}} \end{pmatrix} \begin{pmatrix} B_t & -B^{<} \\ B^{>} & -B_{\bar{t}} \end{pmatrix} = \begin{pmatrix} A_t B_t - A^{<}B^{>} & -A_t B^{<} + A^{<}B_{\bar{t}} \\ A^{>}B_t - A_{\bar{t}}B^{>} & A_{\bar{t}}B_{\bar{t}} - A^{>}B^{<} \end{pmatrix}$$

As a result, we obtain the well-known the Langreth analytic continuation.

$$C^{<} = \int dt(A^R B^{<} + A^{<} B^A) \tag{38}$$

$$C^{>} = \int dt(A^R B^{>} + A^{>} B^A) \tag{39}$$

$$C^R = \int dt(A^R B^R) \tag{40}$$

5.2 Pseudoparticle formalism for the two-particle interactions and the non crossing approximation (NCA) of Anderson impurity model on the Keldysh contour

The essential result of the Abrikosov's trick is that the average of any local operator ($Q = 1$) that vanishes at $Q = 0$ subspace is proportional to the grand-canonical ($Q > 0$) average of the same operator[4]

$$\langle A\rangle_{Q=1} = \lim_{\lambda\to\infty} \frac{\langle A\rangle_\lambda}{\langle Q\rangle_\lambda}, \tag{41}$$

where $\langle A\rangle$ refers to the grand canonical ensemble average of the operator A as the chemical potential $\lambda \to \infty$. The partition function or the normalization factor for the observables is[5, 6]

$$\begin{aligned}\frac{Z_{Q=1}}{Z_{Q=0}} &= \frac{Z_{canonical}}{Z_{band}} &(42)\\ &= \lim_{\lambda\to\infty} e^{\beta\lambda}\langle Q\rangle_\lambda &(43)\\ &= \left\langle b^\dagger b\right\rangle_{Q=1} + \textstyle\sum_\sigma \left\langle f_\sigma^\dagger f_\sigma\right\rangle_{Q=1}. &(44)\end{aligned}$$

This can be expressed as different forms as[5, 7]

$$i\int_{-\infty}^{\infty} d\omega/2\pi e^{i\omega 0}[G_b^<(\omega) - \sum_\sigma G_{f\sigma}^<(\omega)] \tag{45}$$

or

$$-\frac{1}{\pi}\int_{-\infty}^{\infty} d\omega e^{-\beta\omega}\left\{Im[G_b^R(\omega)] + \sum_\sigma Im[G_{f\sigma}^R(\omega)]\right\} \tag{46}$$

To clear any confusions, we newly define quantities $a(\omega)_{b(f\sigma)}$.

$$\begin{aligned}\lim_{t'\to t}\left\langle b^\dagger(t')b(t)\right\rangle &= \int d\omega \frac{i}{2\pi}G_b^<(\omega) = \int d\omega a_b(\omega) &(47)\\ \lim_{t'\to t}\left\langle f_\sigma^\dagger(t')f_\sigma(t)\right\rangle &= \int d\omega \frac{-i}{2\pi}G_{f\sigma}^<(\omega) = \int d\omega a_{f\sigma}(\omega) &(48)\end{aligned}$$

One may deduce from the above equality that $\lim_{\lambda\to\infty} a(\omega, i\lambda) = \lim_{\lambda\to\infty} f(\omega+\lambda)A(\omega) = e^{-\beta\omega}(-\frac{1}{\pi})Im[G^R(\omega)]$, where $\mathcal{G}$ is a pseudo-particle Green's function. However one should notice that this relation is no longer valid out-of-equilibrium.

The Luttinger-Ward(LW) functional diagram (Figure 27) with the lowest approximation (so called non-crossing approximation; NCA) is,

$$\Phi_{NCA}[\mathcal{G}, \Delta] = C^{\alpha\alpha'}_{b_1b_2f_1f_2}\int_0^\beta d\tau \mathcal{G}_{b_2b_1}(\tau)\mathcal{G}_{f_2f_1}(\beta-\tau)\Delta_{\alpha'\alpha}(-\tau), \tag{49}$$

where $-G_{f_2f1}(-\tau) = G_{f_2f_1}(\beta-\tau)$, $\Delta(\omega)$ is the non-interacting bath(or hybridization function) and $C^{\alpha\alpha'}_{b_1b_2f_1f_2} = \sum_{(b_1,b_2),(f_1,f_2),(\alpha,\alpha')\in deg.}(F^{\alpha'})_{b_2f_1}(F^{\dagger\alpha})_{f_2b_1}$. Note at each vertex of the diagram is represented by coefficient F, where $(F^{\alpha'})_{b_2f_1} = \langle b_2| f_{\alpha'} |f_1\rangle$ and $(F^{\dagger\alpha})_{f_2b_1} = \langle f_2| f_\alpha^\dagger |b_1\rangle$.[8] From the LW theorem, the functional derivative of either the pseudo-particle $\mathcal{G}$ or the physical $\mathcal{G}$ of the LW functional yields the sum of all the self-energy terms that satisfy the conservation law.

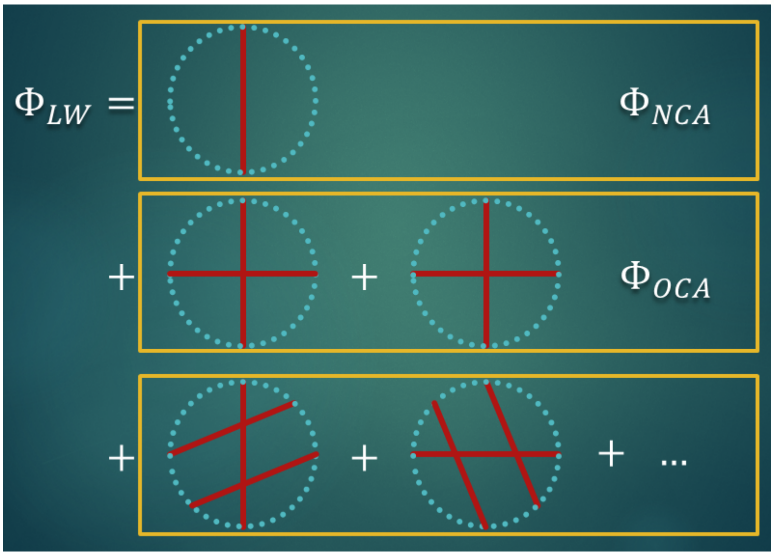

Figure 27: The Luttinger-Ward functional of the Anderson impurity model which contains non-crossing term (NCA), one-crossing term (OCA), and the higher contributions where the green dotted line is pseudo-particle $\mathcal{G}$ and the red line is the bath electron $\mathcal{G}$.

For example, the fermonic pseudo-particle self-energy is the functional derivative of $\Phi_{NCA}[\mathcal{G},\Delta]$ with $\mathcal{G}_{f_2 f_1}$.

$$\Sigma_{f_1 f_2} = \frac{\delta\Phi_{NCA}[\mathcal{G},\Delta]}{\mathcal{G}_{f_2 f_1}} \tag{50}$$

In nonequilibrium formalism, it is simpler to describe physical quantities by $\mathcal{G}^{<,>}(\omega)$. The pseudo-particle self-energies are given as the exactly same integral equation to the equilibrium solution, which is a fortunate coincidence (This is not the case for the OCA). Here, the chemical potential μ_η of left ($\eta = L$) and right ($\eta = R$) leads is given $\mu_L = \mu_0 + V/2$ and $\mu_R = \mu_0 - V/2$, where V is source-drain bias voltage. Here, the greater and retarded quantity only differs by multiple of a constant.

$$\overline{\Sigma}^{R,>}_{mn}(\omega) = \sum_{\eta=L,R}\sum_{\alpha,\beta,m',n'}\int d\xi f(\xi-\mu_\eta)\overline{G}^{R,>}_{m'n'}(\omega+\xi) \quad [F^{\beta}_{mm'}F^{\dagger\alpha}_{n'n}A_{\alpha\beta\eta}(\xi-\mu_\eta) + F^{\dagger\beta}_{mm'}F^{\alpha}_{n'n}A_{\alpha\beta\eta}(-\xi+\mu_\eta)]. \tag{51}$$

and

$$\overline{\Sigma}^{<}_{mn}(\omega) = \sum_{\eta=L,R}\sum_{\alpha,\beta,m',n'}\int d\xi[1-f(\xi-\mu_\eta)]\overline{G}^{<}_{m'n'}(\omega+\xi) \quad [F^{\beta}_{mm'}F^{\dagger\alpha}_{n'n}A_{\alpha\beta\eta}(\xi-\mu_\eta) + F^{\dagger\beta}_{mm'}F^{\alpha}_{n'n}A_{\alpha\beta\eta}(-\xi+\mu_\eta)]. \tag{52}$$

, where $A_{\alpha\beta\eta}(\omega) = -\frac{1}{2\pi i}[\Delta_{\alpha\beta\eta}(\omega+i0^+) - \Delta_{\alpha\beta\eta}(\omega+i0^-)]$ and $\Delta_{\alpha\beta\eta}(\omega) = \pi^2|V|^2\mathcal{N}_\eta(\omega)$. Here, a simple test is possible from the fact that if $\Delta_{\alpha\beta\eta}(\omega)$ is just a constant then the non-equilibrium NCA equations end up with the equilibrium NCA equation with the effective distribution function F_{eff},[7]

$$F_{eff}(\omega) = \frac{\Delta_L}{\Delta_R+\Delta_L}f(\omega-\mu_L) + \frac{\Delta_R}{\Delta_R+\Delta_L}f(\omega-\mu_R)$$

An interesting relation between the pseudo-particle quantities $\mathcal{G}^{>}(\Sigma^{>})$ and $\mathcal{G}^{R}(\Sigma^{R})$ emerges in the limit of $\lambda \to \infty$. $\mathcal{G}^R(t-t', i\lambda) = \theta(t-t')[\mathcal{G}^{>}(t-t', i\lambda) - \mathcal{G}^{<}(t-t', i\lambda)]$ leads to $2iIm[G^R(\omega, i\lambda)] = G^{>}(\omega, i\lambda) - G^{<}(\omega, i\lambda)$ from the famous Kramers-Kronig relation. In the limit of $\lambda \to \infty$,

$$2i\mathrm{Im}[\mathcal{G}^R(\omega)] = \mathcal{G}^{>}(\omega) \tag{53}$$

because $\mathcal{G}^{<}(\omega, i\lambda)$ is proportional to $e^{-\beta\lambda}$ which vanishes in the limit of $\lambda \to \infty$.[5]

The local Green's function can be derived in various ways such as the functional derivative of Φ_{LW} or the equation-of-motion of the Hamiltonian. Here we obtain the local Green's function using the functional derivative of the Luttinger-Ward functional Φ with respect to the bath $\mathcal{G}$, namely the hybridization function Δ. This would mean that the local Green's function satisfies the relation.

$$\mathcal{G}_{d\sigma}(\omega) = \frac{1}{V^2} \lim_{\lambda \to \infty} e^{\beta\lambda} \Sigma_{c\sigma,\mathcal{G}}(\omega, \lambda)$$

What introduces difficulty in obtaining the local $\mathcal{G}_d(\omega)$ is that it is in fact the two particle $\mathcal{G}$ in the pseudo-particle picture $\mathcal{G}^R_{d\sigma,i\lambda}(t-t') = -i\theta(t-t') \left\langle \{b^\dagger(t) f_\sigma(t) f^\dagger_\sigma(t') b(t')\} \right\rangle$. In the NCA limit, however, it is equivalent to the first order perturbation theory (like Hartree-Fock),

$$G_d(\omega) = \lim_{\lambda \to \infty} \frac{e^{\beta\lambda} \left\langle G^R_{d\sigma,i\lambda} \right\rangle}{e^{\beta\lambda} \langle Q \rangle}$$

Thus, the spectral function of the impurity or the retarded impurity Green's function is no longer identical to the equilibrium NCA impurity $\mathcal{G}$. In the equilibrium, the local spectral function is

$$A^{\alpha\alpha'}_{d\sigma}(\omega) = \frac{1}{e^{\beta\lambda}\langle Q \rangle} \sum_{b_1 b_2 f_1 f_2} \int d\xi e^{-\beta\xi}(1+e^{-\beta\omega})(F^{\alpha'})_{b_2 f_1}(F^{\dagger\alpha})_{f_2 b_1} Im[G_{b_1 b_2}(\xi)] Im[G_{f_1 f_2}(\xi+\omega)]$$

However, in nonequilibrium (steady state),

$$\begin{aligned} A^{\alpha\alpha'}_{d\sigma}(\omega) =& \frac{i}{2\pi^2} \frac{1}{e^{\beta\lambda}\langle Q \rangle} \sum_{b_1 b_2 f_1 f_2} \int d\xi (F^{\alpha'})_{b_2 f_1} (F^{\dagger\alpha})_{f_2 b_1} \\ & \left\{ Im[G_{b_1 b_2}(\xi)] G^{<}_{f_1 f_2}(\xi+\omega) - G^{<}_{b_1 b_2}(\xi) Im[G_{f_1 f_2}(\xi+\omega)] \right\} \\ =& \frac{1}{e^{\beta\lambda}\langle Q \rangle} \sum_{b_1 b_2 f_1 f_2} \int d\xi (F^{\alpha'})_{b_2 f_1} (F^{\dagger\alpha})_{f_2 b_1} \{ A_{b_1 b_2}(\xi) a_{f_1 f_2}(\xi+\omega) + a_{b_1 b_2}(\xi) A_{f_1 f_2}(\xi+\omega) \} \end{aligned} \tag{54}$$

where $e^{\beta\lambda}\langle Q \rangle = Z_{Q=1}/Z_{Q=0} = i\int_{-\infty}^{\infty} d\omega/2\pi e^{i\omega 0}[G^{<}_b(\omega) - \sum_\sigma G^{<}_{f\sigma}(\omega)]$. The self-consistency loop of the nonequilibrium NCA is then in closed form by Eq. 51, 52, 53, and 54. Note that a numerical trick due to the exponential factor $e^{-\beta\omega}$ of $\langle Q \rangle$ and the impurity $\mathcal{G}$ is not necessary anymore in the nonequilibrium NCA formalism.

We will generally derive all the quantities related to the current and conductance to overcome the general assumption of proportionate coupling of two leads $\Gamma^L = \lambda\Gamma^R$. The general form of current through the impurity from left(right) is

$$I^{\sigma}_{L(R)} = \mp\frac{e}{\hbar}\sum_{\alpha}\int d\omega \Gamma^{L(R)}(\omega)\left\{f_{L(R)}(\omega)A^{\alpha}_{d}(\omega) - a_d(\omega)\right\}, \tag{55}$$

where $\Gamma^{L(R)}(\omega) = 2\pi\rho(\omega)|V^{L(R)}(\omega)|^2$, $a_d(\omega) = -\frac{i}{2\pi}G^{<}(\omega)$, and $\rho(\omega)$ is DOS of conduction electrons. The lesser green's function of the impurity is

$$a_d(\omega) = \frac{1}{e^{\beta\lambda}\langle Q\rangle}\sum_{b_1 b_2 f_1 f_2}\int d\xi (F^{\alpha'})_{b_2 f_1}(F^{\dagger\alpha})_{f_2 b_1}\left\{A_{b_1 b_2}(\xi)a_{f_1 f_2}(\xi+\omega)\right\}. \tag{56}$$

The current through the impurity should conserve the current $I_d = I_L = I_R = \frac{(I_L+I_R)}{2}$, which was confirmed from our result.

The longitudinal spin susceptiblity(parallel to magnetic field) is given by two-particle correlation of $\chi(\omega) = \langle T_{\tau} d^{\dagger}_{\sigma}(\tau)\sigma_{\sigma\sigma'}d_{\sigma'}(\tau)d^{\dagger}_{\sigma}(0)\sigma_{\sigma\sigma'}d_{\sigma'}(0)\rangle$. In general, in Luttinger-Ward language, two-particle correlation function requires the vertex term for self-consistency, which is the second derivative of LW functional,

$$\Gamma_{12} = \frac{\delta\Phi_{LW}}{\delta G_1 \delta G_2}. \tag{57}$$

Interestingly, the vertex term of Φ_{NCA} vanishes, $\Gamma_{NCA} = 0$. Therefore, $\chi_{NCA}(\omega)$ does not contain any vertex correction and only consists of pseudo fermion propagators.

$$\chi_{NCA}(\omega) \propto Im[G_{f_2 f_1}(\xi)]Im[G_{f_1 f_2}(\xi+\omega) \tag{58}$$

However, it is well known that χ_{NCA} is not very accurate to the exact solution.

5.3 Exact derivation of one-crossing approximation (OCA) on the Keldysh contour

Although, the derivation of the one-crossing approximation (OCA) had been done on the real-time axis,[9] the derivation in the frequency domain is much more desirable. Since the Kondo effect appears around the Fermi level or the chemical potential of the each lead(left or right), one needs a rigorous low energy precision, which is not accessible for the real-time propagation(one needs a very long time limit result of the real-time solution and this will inevitably introduce a noise). An addition of the vertex corrections to the bubble NCA diagram corresponds to OCA. It is beneficial to account these vertex corrections that remedies shortcomings of NCA. Also, OCA gives quite accurate results compared to the exact limit such as quantum monte-carlo (QMC).

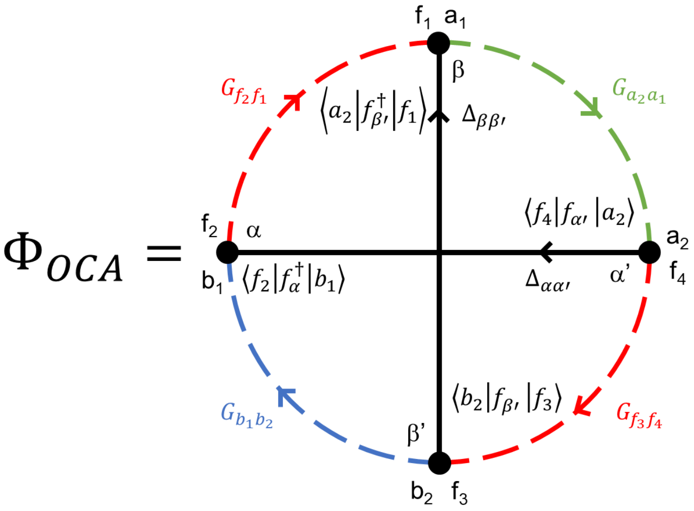

Figure 28: One-crossing approximation Luttinger-Ward functional.

We can use an advantage that the bath electron (the hybridization function) is noninteracting and belongs to the subspace of $\langle Q\rangle = 0$. The self-energy of bath vanishes as $\lambda \to \infty$ because the bath self-energy is proportional to $\langle Q\rangle = 1$. Therefore, we can observe the analytic relation,

$$g^{>}_{k\sigma}(\omega) = -e^{\beta\omega} g^{<}_{k\sigma}(\omega). \tag{59}$$

To confirm the derivation later in Section 5.8, we checked the equilibrium limit of the quantity by substituting nonequilibrium green's function to equilibrium counterpart according to the fluctuation-dissipation theorem. In equilibrium, green's functions, which are independently defined on the Keldysh contour, are now analytically connected. Therefore, we substitute for pseudo particle propagators,

$$G^{<}_{f(b)}(\omega) = \pm 2ie^{-\beta\omega} Im[G^{R}_{f(b)}(\omega)], \tag{60}$$

$$G^{>}_{f(b)}(\omega) = 2iIm[G^{R}_{f(b)}(\omega)], \tag{61}$$

and for the physical quantity (*i.e.* conduction band),

$$G^{<}_{\alpha}(\omega) = if(\omega)\big(-\frac{1}{\pi}Im[G^{R}_{\alpha}(\omega)]\big), \tag{62}$$

$$G^{>}_{\alpha}(\omega) = -if(-\omega)\big(-\frac{1}{\pi}Im[G^{R}_{\alpha}(\omega)]\big). \tag{63}$$

Here, we explicitly derive each OCA pseudo-particle self-energy and the impurity Green's function on the Keldysh contour. An important observation was made that the order of $e^{-\beta\lambda Q}$ should match between the terms. Unless in the limit of $\lambda \to \infty$, terms that are still proportional to $e^{-\beta\lambda Q}$ will vanish. Surprisingly, this greatly simplifies our derivation. Also, note that the either greater or lesser bath(or hybridization) function belongs to $Q = 0$ space. The pseudo-particle self-energies of empty boson, doubly occupied boson, singly occupied fermion, and the impurity Green's function are derived as follows.[10]

5.4 The empty bosonic self-energy Σ_b

From now on, we simplify our notation: $\tau_1(t_1) \to 1, \tau_2(t_2) \to 2$ *etc*, and ignore pseudo-particle notations $f_1, f_2, b_1, b_2, a_1, a_2$, and coefficients for a moment.

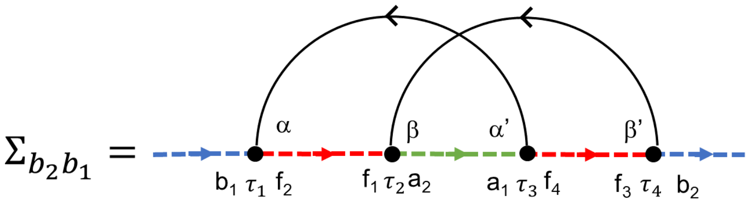

Figure 29: The Feynmann diagram of the empty bosonic self-energy at OCA.

The empty bosonic self-energy (Figure 29) is obtained by functional derivative, $\delta\Phi_{OCA}/\delta G_{b_1,b_2}$ as below (refer to Figure 28).

$$\Sigma_{b_2 b_1}(41) = \frac{\delta\Phi_{OCA}}{\delta G_{b_2,b_1}} \tag{64}$$

$$= \int d2 \int d3 G(21)G(32)G(13)G(43)G(24) \tag{65}$$

If the integration $\int d2 \int d3$ is along $\mathcal{C}_K$, then we need to deform the contour following Langreth method. (Figure 30a)

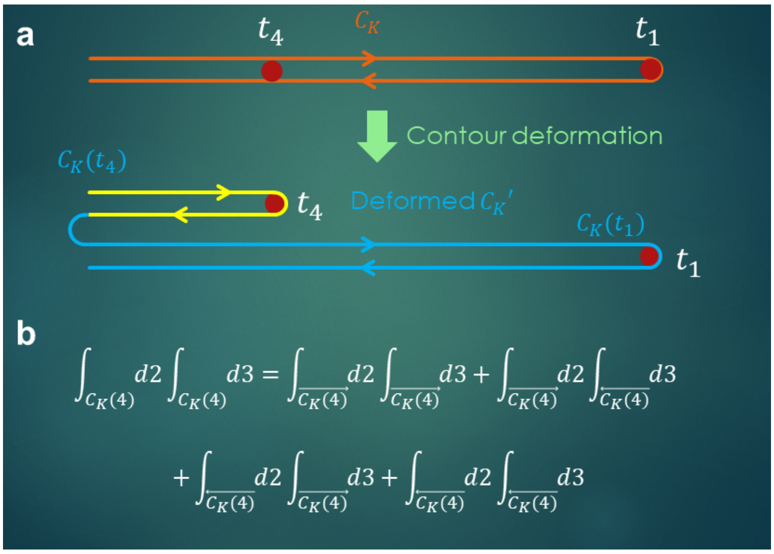

Figure 30: (a) The contour deformation of the Keldysh path. After the deformation, distinct four paths are obtained from $\mathcal{C}_K$. (b) The double integral of t_2, t_3 along the deformed contour is then decomposed of 16 double integrals. One of the example of four integrals out of 16 integrals is shown.

5.4.1 Lesser empty pseudoparticle self-energy $\Sigma^<_{b_2 b_1}(\omega)$

For $\Sigma^<_{b_2 b_1}(t_4 - t_1)$, by definition, t_4 is always lesser than t_1. By deforming the contour $\mathcal{C}_K$ (Figure 30a), it decomposes into two contours: $\mathcal{C}_K(t_4)$ and $\mathcal{C}_K(t_1)$. (Figure 30b). The time integration

$\int d\tau$ then becomes

$$\int d\tau_2 \int d\tau_3 \to (\int_{\mathcal{C}_K(t_4)} dt_2 + \int_{\mathcal{C}_K(t_1)} dt_2) \times (\int_{\mathcal{C}_K(t_4)} dt_3 + \int_{\mathcal{C}_K(t_1)} dt_3)$$

and the whole self-energy integration becomes

$$(\int_{\mathcal{C}_K(t_4)} d2 + \int_{\mathcal{C}_K(t_1)} d2) \times (\int_{\mathcal{C}_K(t_4)} d3 + \int_{\mathcal{C}_K(t_1)} d3) G(21)G(32)G(13)G(43)G(24). \tag{66}$$

Now we further break down the integral (Eq. 66). Depending on the contour, the ordering of time changes and corresponding $\mathcal{G}$ also changes too. *vide infra.*

$$(1) \quad \int_{\mathcal{C}_K(t_4)} d2 \int_{\mathcal{C}_K(t_4)} d3 \to t_2, t_3, t_4 < t_1.$$

$$(1.1) \int d2\overrightarrow{\mathcal{C}_K}(t_4) \int d3\overrightarrow{\mathcal{C}_K}(t_4):\ t_2, t_3 < t_4 < t_1, (1.2) \int d2\overrightarrow{\mathcal{C}_K}(t_4) \int d3\overleftarrow{\mathcal{C}_K}(t_4):\ t_2 < t_4 < t_3 < t_1,$$

$$(1.3) \int d2\overleftarrow{\mathcal{C}_K}(t_4) \int d3\overrightarrow{\mathcal{C}_K}(t_4):\ t_3 < t_4 < t_2 < t_1, (1.4) \int d2\overleftarrow{\mathcal{C}_K}(t_4) \int d3\overleftarrow{\mathcal{C}_K}(t_4):\ t_4 < t_2, t_3 < t_1.$$

$$(2) \int_{\mathcal{C}_K(t_4)} d2 \int_{\mathcal{C}_K(t_1)} d3 \to t_2, t_4 < t_1, t_3.$$

$$(2.1) \int d2\overrightarrow{\mathcal{C}_K}(t_4) \int d3\overrightarrow{\mathcal{C}_K}(t_1):\ t_2 < t_4 < t_3 < t_1 (2.2) \int d2\overrightarrow{\mathcal{C}_K}(t_4) \int d3\overleftarrow{\mathcal{C}_K}(t_1):\ t_2 < t_4 < t_1 < t_3,$$

$$(2.3) \int d2\overleftarrow{\mathcal{C}_K}(t_4) \int d3\overrightarrow{\mathcal{C}_K}(t_1):\ t_4 < t_2 < t_3 < t_1, (2.4) \int d2\overleftarrow{\mathcal{C}_K}(t_4) \int d3\overleftarrow{\mathcal{C}_K}(t_1):\ t_4 < t_2 < t_1 < t_3.$$

$$(3) \int_{\mathcal{C}_K(t_1)} d2 \int_{\mathcal{C}_K(t_4)} d3 \to t_3, t_4 < t_1, t_2.$$

$$(3.1) \int d2\overrightarrow{\mathcal{C}_K}(t_1) \int d3\overrightarrow{\mathcal{C}_K}(t_4):\ t_3 < t_4 < t_2 < t_1, (3.2) \int d2\overrightarrow{\mathcal{C}_K}(t_1) \int d3\overleftarrow{\mathcal{C}_K}(t_4):\ t_4 < t_3 < t_2 < t_1,$$

$$(3.3) \int d2\overleftarrow{\mathcal{C}_K}(t_1) \int d3\overrightarrow{\mathcal{C}_K}(t_4):\ t_3 < t_4 < t_1 < t_2, (3.4) \int d2\overleftarrow{\mathcal{C}_K}(t_1) \int d3\overleftarrow{\mathcal{C}_K}(t_4):\ t_4 < t_3 < t_1 < t_2.$$

$$(4) \int_{\mathcal{C}_K(t_1)} d2 \int_{\mathcal{C}_K(t_1)} d3 \to t_4 < t_1, t_2, t_3$$

$$(4.1) \int d2\overrightarrow{\mathcal{C}_K}(t_1) \int d3\overrightarrow{\mathcal{C}_K}(t_1):\ t_4 < t_2, t_3 < t_1, (4.2) \int d2\overrightarrow{\mathcal{C}_K}(t_1) \int d3\overleftarrow{\mathcal{C}_K}(t_1):\ t_4 < t_2 < t_1 < t_3,$$

$$(4.3) \int d2\overleftarrow{\mathcal{C}_K}(t_1) \int d3\overrightarrow{\mathcal{C}_K}(t_1):\ t_4 < t_3 < t_1 < t_2, (4.4) \int d2\overleftarrow{\mathcal{C}_K}(t_1) \int d3\overleftarrow{\mathcal{C}_K}(t_1):\ t_4 < t_1 < t_2, t_3.$$

It is important to remind that the pseudo-particle $\mathcal{G}, \Sigma$ is proportional to $\sim e^{-\beta\lambda Q}$ $(Q = 0, 1)$. Note that $\Sigma_b^<$ is $\sim e^{-\beta\lambda}$, removing terms that contain terms $e^{-\beta\lambda Q}$ $(Q > 2)$. Surviving terms

($\sim e^{-\beta\lambda Q}$; $Q = 1$) are in red.

$$
\begin{aligned}
\int_{-\infty}^{\infty}\int_{-\infty}^{\infty} d2d3\big(&\theta(42)\theta(43)G^{<}(21)G^{t}(32)G^{>}(13)G^{>}(43)G^{<}(24) \\
&-\theta(42)\theta(43)G^{<}(21)G^{>}(32)G^{>}(13)G^{<}(43)G^{<}(24) \\
&-\theta(42)\theta(43)G^{<}(21)G^{<}(32)G^{>}(13)G^{>}(43)G^{>}(24) \\
&+\theta(42)\theta(43)G^{<}(21)G^{\tilde{t}}(32)G^{>}(13)G^{<}(43)G^{>}(24) \\
&+\theta(42)\theta(13)G^{<}(21)G^{>}(32)G^{>}(13)G^{<}(43)G^{<}(24) \\
&-\theta(42)\theta(13)G^{<}(21)G^{>}(32)G^{>}(13)G^{<}(43)G^{>}(24) \\
&-\theta(42)\theta(13)G^{<}(21)G^{>}(32)G^{<}(13)G^{<}(43)G^{<}(24) \\
&+\theta(42)\theta(13)G^{<}(21)G^{>}(32)G^{<}(13)G^{<}(43)G^{>}(24) \\
&+\theta(12)\theta(43)G^{<}(21)G^{<}(32)G^{>}(13)G^{>}(43)G^{>}(24) \\
&-\theta(12)\theta(43)G^{<}(21)G^{<}(32)G^{>}(13)G^{<}(43)G^{>}(24) \\
&-\theta(12)\theta(43)G^{>}(21)G^{<}(32)G^{>}(13)G^{>}(43)G^{>}(24) \\
&+\theta(12)\theta(43)G^{>}(21)G^{<}(32)G^{>}(13)G^{<}(43)G^{>}(24) \\
&\theta(12)\theta(13)G^{<}(21)G^{t}(32)G^{>}(13)G^{<}(43)G^{>}(24) \\
&-\theta(12)\theta(13)G^{<}(21)G^{>}(32)G^{<}(13)G^{<}(43)G^{>}(24) \\
&-\theta(12)\theta(13)G^{>}(21)G^{<}(32)G^{>}(13)G^{<}(43)G^{>}(24) \\
&+\theta(12)\theta(13)G^{>}(21)G^{\tilde{t}}(32)G^{<}(13)G^{<}(43)G^{>}(24)\big).
\end{aligned}
\tag{67}
$$

There are still crucial observations for the derivation. First, in the pseudo-particle method, because $G^{<}$ vanish in large λ limit,

$$G^{R}(21) = \theta(21)G^{>}(21) \tag{68}$$

$$G^{A}(21) = -\theta(12)G^{>}(21) \tag{69}$$

$$G^{R}(21) = G^{t}(21) \tag{70}$$

$$G^{A}(21) = -G^{\tilde{t}}(21). \tag{71}$$

Second, a seemingly nonvanishing term $\theta(t_4 - t_2)$ or $\theta(t_1 - t_3)$ from the above Eq. 68, can naturally be disappeared. For instance,

$$
\begin{aligned}
&\int_{-\infty}^{\infty}\int_{-\infty}^{\infty} d2d3\theta(42)\theta(43)G^{<}(21)G^{t}(32)G^{>}(13)G^{>}(43)G^{<}(24) \\
= &\int_{-\infty}^{\infty}\int_{-\infty}^{\infty} d2d3\theta(42)\theta(43)\theta(32)G^{<}(21)G^{>}(32)G^{>}(13)G^{>}(43)G^{<}(24).
\end{aligned}
$$

And on the $\int d2\overrightarrow{\mathcal{C}_K}(t_4)\int d3\overrightarrow{\mathcal{C}_K}(t_4)$ contour, the time notation t_3 is always lesser than t_4. Thus, $\theta(t_4 - t_2)\theta(t_3 - t_2) = \theta(t_3 - t_2)$, given that $t_3 < t_4$.

$$
\begin{aligned}
\Sigma^{<}_{b_2b_1}(t_4, t_1) = \int_{-\infty}^{\infty}\int_{-\infty}^{\infty} dt_2dt_3 \quad & G^{<}_{f_1f_2}(t_2, t_1)G^{R}_{a_1a_2}(t_3, t_2)G^{>}_{\alpha\alpha'}(t_1, t_3)G^{R}_{f_3f_4}(t_4, t_3)G^{<}_{\beta\beta'}(t_2, t_4) \\
+ \quad & G^{A}_{f_1f_2}(t_2, t_1)G^{<}_{a_1a_2}(t_3, t_2)G^{>}_{\alpha\alpha'}(t_1, t_3)G^{R}_{f_3f_4}(t_4, t_3)G^{>}_{\beta\beta'}(t_2, t_4) \\
+ \quad & G^{A}_{f_1f_2}(t_2, t_1)G^{A}_{a_1a_2}(t_3, t_2)G^{<}_{\alpha\alpha'}(t_1, t_3)G^{<}_{f_3f_4}(t_4, t_3)G^{>}_{\beta\beta'}(t_2, t_4).
\end{aligned}
$$

and in frequency space,

$$\begin{aligned}\Sigma^{<}_{b_2b_1}(\omega) = &\int dy G^{<}_{\beta\beta'}(y) G^{R}_{f_3f_4}(y+\omega) \int dx G^{>}_{\alpha\alpha'}(x) G^{<}_{f_1f_2}(x+\omega) G^{R}_{a_1a_2}(x+y+\omega) \\ + &\int dy G^{>}_{\beta\beta'}(y) G^{R}_{f_3f_4}(y+\omega) \int dx G^{>}_{\alpha\alpha'}(x) G^{A}_{f_1f_2}(x+\omega) G^{<}_{a_1a_2}(x+y+\omega) \\ + &\int dy G^{>}_{\beta\beta'}(y) G^{<}_{f_3f_4}(y+\omega) \int dx G^{<}_{\alpha\alpha'}(x) G^{A}_{f_1f_2}(x+\omega) G^{A}_{a_1a_2}(x+y+\omega). \qquad (72)\end{aligned}$$

where the non-equilibrium NCA term is marked in red.[5]

5.4.2 Greater empty pseudoparticle self-energy $\Sigma^{>}_{b_2b_1}(\omega)$

Here, t_4 is always later than t_1 contrary to Section 5.4.1. We therefore need another contour that fullfills this condition (Figure 31). Also note that the greater $\Sigma^{>}_{b_2b_1}(\omega)$ is $\sim O(1)$ so that the terms $\geq O(e^{-\beta\lambda})$ will vanish at $\lambda \to \infty$. The derivations are following.

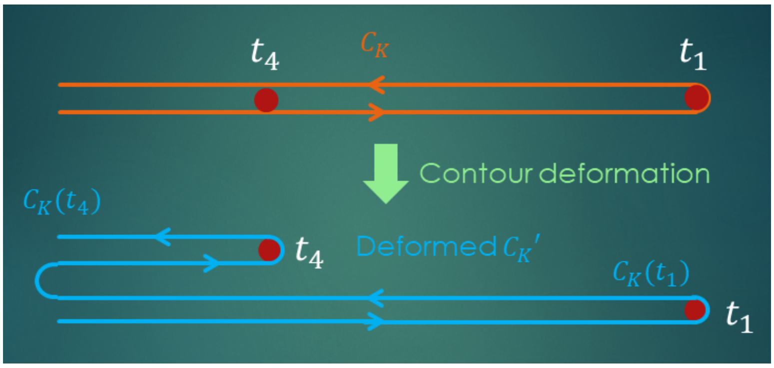

Figure 31: The contour deformation of the Keldysh path, which satisfies the condition $t_4 > t_1$.

$$(1) \int_{\mathcal{C}_K(t_1)} d2 \int_{\mathcal{C}_K(t_1)} d3 \to t_1, t_2, t_3 < t_4$$

$$(1.1) \int d2\overrightarrow{\mathcal{C}_K}(t_1) \int d3\overrightarrow{\mathcal{C}_K}(t_1):\ t_2, t_3 < t_1 < t_4, (1.2) \int d2\overrightarrow{\mathcal{C}_K}(t_1) \int d3\overleftarrow{\mathcal{C}_K}(t_1):\ t_2 < t_1 < t_3 < t_4,$$

$$(1.3) \int d2\overleftarrow{\mathcal{C}_K}(t_1) \int d3\overrightarrow{\mathcal{C}_K}(t_1):\ t_3 < t_1 < t_2 < t_4, (1.4) \int d2\overleftarrow{\mathcal{C}_K}(t_1) \int d3\overleftarrow{\mathcal{C}_K}(t_1):\ t_1 < t_2, t_3 < t_4.$$

$$(2) \int_{\mathcal{C}_K(t_1)} d2 \int_{\mathcal{C}_K(t_4)} d3 \to t_1, t_2 < t_3, t_4$$

$$(2.1) \int d2\overrightarrow{\mathcal{C}_K}(t_1) \int d3\overrightarrow{\mathcal{C}_K}(t_4):\ t_2 < t_1 < t_3 < t_4, (2.2) \int d2\overrightarrow{\mathcal{C}_K}(t_1) \int d3\overleftarrow{\mathcal{C}_K}(t_4):\ t_2 < t_1 < t_4 < t_3,$$

$$(2.3) \int d2\overleftarrow{\mathcal{C}_K}(t_1) \int d3\overrightarrow{\mathcal{C}_K}(t_4):\ t_1 < t_2 < t_3 < t_4, (2.4) \int d2\overleftarrow{\mathcal{C}_K}(t_1) \int d3\overleftarrow{\mathcal{C}_K}(t_4):\ t_1 < t_2 < t_4 < t_3.$$

$$(3) \int_{\mathcal{C}_K(t_4)} d2 \int_{\mathcal{C}_K(t_1)} d3 \to t_1, t_3 < t_2, t_4$$

$$(3.1) \int d2\overrightarrow{\mathcal{C}_K}(t_4) \int d3\overrightarrow{\mathcal{C}_K}(t_1):\ t_3 < t_1 < t_2 < t_4, (3.2) \int d2\overrightarrow{\mathcal{C}_K}(t_4) \int d3\overleftarrow{\mathcal{C}_K}(t_1):\ t_1 < t_3 < t_2 < t_4,$$

$$(3.3) \int d2\overleftarrow{\mathcal{C}_K}(t_4) \int d3\overrightarrow{\mathcal{C}_K}(t_1):\ t_3 < t_1 < t_4 < t_2, (3.4) \int d2\overleftarrow{\mathcal{C}_K}(t_4) \int d3\overleftarrow{\mathcal{C}_K}(t_1):\ t_1 < t_3 < t_4 < t_2.$$

$$(4)\int_{\mathcal{C}_K(t_4)} d2 \int_{\mathcal{C}_K(t_4)} d3 \rightarrow t_1 < t_2, t_3, t_4$$

$$(4.1)\ \int d2\overrightarrow{\mathcal{C}_K}(t_4)\int d3\overrightarrow{\mathcal{C}_K}(t_4):\ t_1 < t_2, t_3 < t_4, (4.2)\ \int d2\overrightarrow{\mathcal{C}_K}(t_4)\int d3\overleftarrow{\mathcal{C}_K}(t_4):\ t_1 < t_2 < t_4 < t_3,$$
$$(4.3)\ \int d2\overleftarrow{\mathcal{C}_K}(t_4)\int d3\overrightarrow{\mathcal{C}_K}(t_4):\ t_1 < t_3 < t_4 < t_2, (4.4)\ \int d2\overleftarrow{\mathcal{C}_K}(t_4)\int d3\overleftarrow{\mathcal{C}_K}(t_4):\ t_1 < t_4 < t_2, t_3.$$

$$\begin{aligned}\int_{-\infty}^{\infty}\int_{-\infty}^{\infty} d2d3\big(&\theta(12)\theta(13)G^{<}(21)G^{t}(32)G^{>}(13)G^{>}(43)G^{<}(24)\\
&-\theta(12)\theta(13)G^{<}(21)G^{>}(32)G^{<}(13)G^{>}(43)G^{<}(24)\\
&-\theta(12)\theta(13)G^{>}(21)G^{<}(32)G^{>}(13)G^{>}(43)G^{<}(24)\\
&+\theta(12)\theta(13)G^{>}(21)G^{\tilde{t}}(32)G^{<}(13)G^{>}(43)G^{<}(24)\\
&+\theta(12)\theta(43)G^{<}(21)G^{>}(32)G^{<}(13)G^{>}(43)G^{<}(24)\\
&-\theta(12)\theta(43)G^{>}(21)G^{>}(32)G^{<}(13)G^{<}(43)G^{<}(24)\\
&-\theta(12)\theta(43)G^{>}(21)G^{>}(32)G^{<}(13)G^{>}(43)G^{<}(24)\\
&+\theta(12)\theta(43)G^{>}(21)G^{>}(32)G^{<}(13)G^{<}(43)G^{<}(24)\\
&+\theta(42)\theta(13)G^{>}(21)G^{<}(32)G^{>}(13)G^{>}(43)G^{<}(24)\\
&-\theta(42)\theta(13)G^{>}(21)G^{<}(32)G^{<}(13)G^{>}(43)G^{<}(24)\\
&-\theta(42)\theta(13)G^{>}(21)G^{<}(32)G^{>}(13)G^{>}(43)G^{>}(24)\\
&+\theta(42)\theta(13)G^{>}(21)G^{<}(32)G^{<}(13)G^{>}(43)G^{>}(24)\\
&+\theta(42)\theta(43)G^{>}(21)G^{t}(32)G^{<}(13)G^{>}(43)G^{<}(24)\\
&-\theta(42)\theta(43)G^{>}(21)G^{>}(32)G^{<}(13)G^{<}(43)G^{<}(24)\\
&-\theta(42)\theta(43)G^{>}(21)G^{<}(32)G^{<}(13)G^{>}(43)G^{>}(24)\\
&+\theta(42)\theta(43)G^{>}(21)G^{\tilde{t}}(32)G^{<}(13)G^{<}(43)G^{>}(24)\big).\end{aligned}$$

The final result is

$$\begin{aligned}\Sigma^{>}_{b_2b_1}(t_4,t_1) = \int_{-\infty}^{\infty}\int_{-\infty}^{\infty} dt_2dt_3 \quad & G^{A}_{f_1f_2}(t_2,t_1)G^{A}_{a_1a_2}(t_3,t_2)G^{<}_{\alpha\alpha'}(t_1,t_3)G^{>}_{f_3f_4}(t_4,t_3)G^{<}_{\beta\beta'}(t_2,t_4)\\
&+G^{A}_{f_1f_2}(t_2,t_1)G^{>}_{a_1a_2}(t_3,t_2)G^{<}_{\alpha\alpha'}(t_1,t_3)G^{R}_{f_3f_4}(t_4,t_3)G^{<}_{\beta\beta'}(t_2,t_4)\\
&+G^{>}_{f_1f_2}(t_2,t_1)G^{R}_{a_1a_2}(t_3,t_2)G^{<}_{\alpha\alpha'}(t_1,t_3)G^{R}_{f_3f_4}(t_4,t_3)G^{<}_{\beta\beta'}(t_2,t_4).\end{aligned} \tag{73}$$

and in frequency space,

$$\begin{aligned}\Sigma^{>}_{b_2b_1}(\omega) = \quad & \int dyG^{<}_{\beta\beta'}(y)G^{>}_{f_3f_4}(y+\omega)\int dxG^{<}_{\alpha\alpha'}(x)G^{A}_{f_1f_2}(x+\omega)G^{A}_{a_1a_2}(x+y+\omega)\\
&+\int dyG^{<}_{\beta\beta'}(y)G^{R}_{f_3f_4}(y+\omega)\int dxG^{<}_{\alpha\alpha'}(x)G^{A}_{f_1f_2}(x+\omega)G^{>}_{a_1a_2}(x+y+\omega)\\
&+\int dyG^{<}_{\beta\beta'}(y)G^{R}_{f_3f_4}(y+\omega)\int dxG^{<}_{\alpha\alpha'}(x)G^{>}_{f_1f_2}(x+\omega)G^{R}_{a_1a_2}(x+y+\omega).\end{aligned} \tag{74}$$

5.5 The sinlgly-occupied fermionic self-energy, $\Sigma_f(\omega)$

The singly occupied fermionic self-energy (Figure 32) is obtained by the functional derivative, $\delta\Phi_{OCA}/\delta G_{f_1,f_2}$ as below (refer to Figure 28).

$$\begin{aligned} \Sigma_{f_2,f_1}(41) &= \frac{\delta\Phi_{OCA}}{\delta G_{f_1,f_2}} && (75)\\ &= \int d2 \int d3 G(21)G(32)G(13)G(43)G(42) && (76) \end{aligned}$$

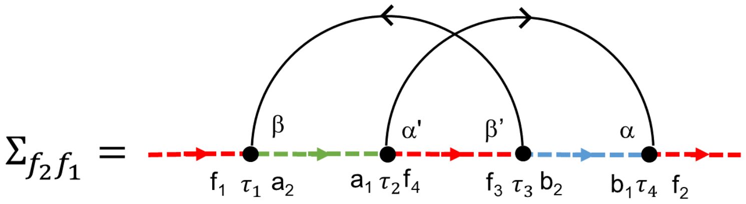

Figure 32: The Feynmann diagram of the singley occupied fermionic self-energy at OCA.

5.5.1 Lesser singly-occupied pseudoparticle self-energy $\Sigma^<_{f_2 f_1}(\omega)$

The same contour is taken as in Section 5.4.1, therefore, for $\Sigma^<_f(\omega)$,

$$\begin{aligned} \int_{-\infty}^{\infty}\int_{-\infty}^{\infty} d2d3\big(&\theta(42)\theta(43)G^<(21)G^t(32)G^>(13)G^>(43)G^>(42) && (77)\\
&-\theta(42)\theta(43)G^<(21)G^>(32)G^>(13)G^<(43)G^>(42)\\
&-\theta(42)\theta(43)G^<(21)G^<(32)G^>(13)G^>(43)G^<(42)\\
&+\theta(42)\theta(43)G^<(21)G^{\tilde t}(32)G^>(13)G^<(43)G^<(42)\\
&+\theta(42)\theta(13)G^<(21)G^>(32)G^>(13)G^<(43)G^>(42)\\
&-\theta(42)\theta(13)G^<(21)G^>(32)G^<(13)G^<(43)G^>(42)\\
&-\theta(42)\theta(13)G^<(21)G^>(32)G^>(13)G^<(43)G^<(42)\\
&+\theta(42)\theta(13)G^<(21)G^>(32)G^<(13)G^<(43)G^<(42)\\
&+\theta(12)\theta(43)G^<(21)G^<(32)G^>(13)G^>(43)G^<(42)\\
&-\theta(12)\theta(43)G^<(21)G^<(32)G^>(13)G^<(43)G^<(42)\\
&-\theta(12)\theta(43)G^>(21)G^<(32)G^>(13)G^>(43)G^<(42)\\
&+\theta(12)\theta(43)G^>(21)G^<(32)G^>(13)G^<(43)G^<(42)\\
&+\theta(12)\theta(13)G^<(21)G^t(32)G^>(13)G^<(43)G^<(42)\\
&-\theta(12)\theta(13)G^<(21)G^>(32)G^<(13)G^<(43)G^<(42)\\
&-\theta(12)\theta(13)G^>(21)G^<(32)G^>(13)G^<(43)G^<(42)\\
&+\theta(12)\theta(13)G^>(21)G^{\tilde t}(32)G^<(13)G^<(43)G^<(42)\big). \end{aligned}$$

Only counting the terms $\sim O(e^{-\beta\lambda})$,

$$\begin{aligned}\Sigma^{<}_{f_2 f_1}(t_4,t_1) = \int_{-\infty}^{\infty}\int_{-\infty}^{\infty} dt_2 dt_3 \quad & G^{<}_{a_1a_2}(t_2,t_1)G^{R}_{f_3f_4}(t_3,t_2)G^{>}_{\beta\beta'}(t_1,t_3)G^{R}_{b_1b_2}(t_4,t_3)G^{>}_{\alpha\alpha'}(t_4,t_2) \\ & +G^{A}_{a_1a_2}(t_2,t_1)G^{<}_{f_3f_4}(t_3,t_2)G^{>}_{\beta\beta'}(t_1,t_3)G^{R}_{b_1b_2}(t_4,t_3)G^{<}_{\alpha\alpha'}(t_4,t_2) \\ & +G^{A}_{a_1a_2}(t_2,t_1)G^{A}_{f_3f_4}(t_3,t_2)G^{<}_{\beta\beta'}(t_1,t_3)G^{<}_{b_1b_2}(t_4,t_3)G^{<}_{\alpha\alpha'}(t_4,t_2).\end{aligned}\tag{78}$$

and in the frequency space,

$$\begin{aligned}\Sigma^{<}_{f_2 f_1}(\omega) = \int dy \quad & G^{>}_{\alpha\alpha'}(y)G^{R}_{b_1b_2}(\omega-y)\int dx G^{>}_{\beta\beta'}(x)G^{<}_{a_1a_2}(x+\omega)G^{R}_{f_3f_4}(x-y+\omega) \\ + \quad & G^{<}_{\alpha\alpha'}(y)G^{R}_{b_1b_2}(\omega-y)\int dx G^{>}_{\beta\beta'}(x)G^{A}_{a_1a_2}(x+\omega)G^{<}_{f_3f_4}(x-y+\omega) \\ + \quad & G^{<}_{\alpha\alpha'}(y)G^{<}_{b_1b_2}(\omega-y)\int dx G^{<}_{\beta\beta'}(x)G^{A}_{a_1a_2}(x+\omega)G^{A}_{f_3f_4}(x-y+\omega).\end{aligned}\tag{79}$$

5.5.2 Greater singly-occupied pseudoparticle self-energy $\Sigma^{>}_{f_2 f_1}(\omega)$

The same contour is taken as in Section 5.4.2, therefore, for $\Sigma^{>}_{f}(\omega)$,

$$\begin{aligned}\int_{-\infty}^{\infty}\int_{-\infty}^{\infty} d2d3\big(&\theta(12)\theta(13)G^{<}(21)G^{t}(32)G^{>}(13)G^{>}(43)G^{>}(42) \\ &-\theta(12)\theta(13)G^{<}(21)G^{>}(32)G^{<}(13)G^{>}(43)G^{>}(42) \\ &-\theta(12)\theta(13)G^{>}(21)G^{<}(32)G^{>}(13)G^{>}(43)G^{>}(42) \\ &+\theta(12)\theta(13)G^{>}(21)G^{\tilde{t}}(32)G^{<}(13)G^{>}(43)G^{>}(42) \\ &+\theta(12)\theta(43)G^{<}(21)G^{>}(32)G^{<}(13)G^{>}(43)G^{>}(42) \\ &-\theta(12)\theta(43)G^{>}(21)G^{>}(32)G^{<}(13)G^{<}(43)G^{>}(42) \\ &-\theta(12)\theta(43)G^{>}(21)G^{>}(32)G^{<}(13)G^{>}(43)G^{>}(42) \\ &+\theta(12)\theta(43)G^{>}(21)G^{>}(32)G^{<}(13)G^{<}(43)G^{>}(42) \\ &+\theta(42)\theta(13)G^{>}(21)G^{<}(32)G^{>}(13)G^{>}(43)G^{>}(42) \\ &-\theta(42)\theta(13)G^{>}(21)G^{<}(32)G^{<}(13)G^{>}(43)G^{>}(42) \\ &-\theta(42)\theta(13)G^{>}(21)G^{<}(32)G^{>}(13)G^{>}(43)G^{<}(42) \\ &+\theta(42)\theta(13)G^{>}(21)G^{<}(32)G^{<}(13)G^{>}(43)G^{<}(42) \\ &+\theta(42)\theta(43)G^{>}(21)G^{t}(32)G^{<}(13)G^{>}(43)G^{>}(42) \\ &-\theta(42)\theta(43)G^{>}(21)G^{>}(32)G^{<}(13)G^{<}(43)G^{>}(42) \\ &-\theta(42)\theta(43)G^{>}(21)G^{<}(32)G^{<}(13)G^{>}(43)G^{<}(42) \\ &+\theta(42)\theta(43)G^{>}(21)G^{\tilde{t}}(32)G^{<}(13)G^{<}(43)G^{<}(42)\big).\end{aligned}$$

only surviving terms are

$$\begin{aligned}\Sigma^{>}_{f_2 f_1}(t_4,t_1) = \int_{-\infty}^{\infty}\int_{-\infty}^{\infty} dt_2 dt_3 \quad & G^{A}_{a_1a_2}(t_2,t_1)G^{A}_{f_3f_4}(t_3,t_2)G^{<}_{\beta\beta'}(t_1,t_3)G^{>}_{b_1b_2}(t_4,t_3)G^{>}_{\alpha\alpha'}(t_4,t_2) \\ & +G^{A}_{a_1a_2}(t_2,t_1)G^{>}_{f_3f_4}(t_3,t_2)G^{<}_{\beta\beta'}(t_1,t_3)G^{R}_{b_1b_2}(t_4,t_3)G^{>}_{\alpha\alpha'}(t_4,t_2) \\ & +G^{>}_{a_1a_2}(t_2,t_1)G^{R}_{f_3f_4}(t_3,t_2)G^{<}_{\beta\beta'}(t_1,t_3)G^{R}_{b_1b_2}(t_4,t_3)G^{>}_{\alpha\alpha'}(t_4,t_2).\end{aligned}\tag{80}$$

and in the frequency space,

$$\begin{aligned}\Sigma^{>}_{f_2f_1}(\omega) = \int dy \quad & G^{>}_{\alpha'\alpha}(y)G^{>}_{b_1b_2}(\omega-y)\int dx G^{<}_{\beta\beta'}(x)G^{A}_{a_1a_2}(x+\omega)G^{A}_{f_3f_4}(x-y+\omega) \\ + \quad & G^{>}_{\alpha'\alpha}(y)G^{R}_{b_1b_2}(\omega-y)\int dx G^{<}_{\beta\beta'}(x)G^{A}_{a_1a_2}(x+\omega)G^{>}_{f_3f_4}(x-y+\omega) \\ + \quad & G^{>}_{\alpha'\alpha}(y)G^{R}_{b_1b_2}(\omega-y)\int dx G^{<}_{\beta\beta'}(x)G^{>}_{a_1a_2}(x+\omega)G^{R}_{f_3f_4}(x-y+\omega).\end{aligned} \tag{81}$$

5.6 Doubly-occupied bosonic self-energy, Σ_a

The doubly-occupied bosonic self-energy (Figure 33) is obtained by the functional derivative, $\delta\Phi_{OCA}/\delta G_{a_1a_2}$ as below (refer to Figure 28).

$$\begin{aligned}\Sigma_{a_2a_1}(41) &= \frac{\delta\Phi_{OCA}}{\delta G_{a_1a_2}} && (82)\\ &= \int d2\int d3G(21)G(32)G(31)G(43)G(42) && (83)\end{aligned}$$

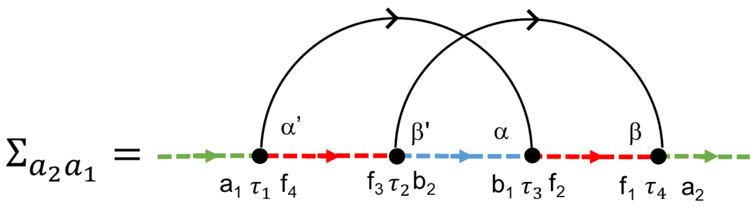

Figure 33: The Feynmann diagram of the doubly-occupied bosonic self-energy at OCA.

5.6.1 Lesser doubly-occupied pseudoparticle self-energy $\Sigma^<_{a_2a_1}(\omega)$

In the course of the derivation, we notice that only bath $\mathcal{G}$ (or hybridization) has a different time-ordering for each pseudo-particle self-energy.

$$\begin{aligned}\int_{-\infty}^{\infty}\int_{-\infty}^{\infty} d2d3\Big(&\theta(42)\theta(43)G^<(21)G^t(32)G^<(31)G^>(43)G^>(42) && (84)\\ &-\theta(42)\theta(43)G^<(21)G^>(32)G^<(31)G^<(43)G^>(42)\\ &-\theta(42)\theta(43)G^<(21)G^<(32)G^<(31)G^>(43)G^<(42)\\ &+\theta(42)\theta(43)G^<(21)G^{\tilde{t}}(32)G^<(31)G^<(43)G^<(42)\\ &+\theta(42)\theta(13)G^<(21)G^>(32)G^<(31)G^<(43)G^>(42)\\ &-\theta(42)\theta(13)G^<(21)G^>(32)G^<(31)G^<(43)G^<(42)\\ &-\theta(42)\theta(13)G^<(21)G^>(32)G^>(31)G^<(43)G^>(42)\\ &+\theta(42)\theta(13)G^<(21)G^>(32)G^>(31)G^<(43)G^<(42)\\ &+\theta(12)\theta(43)G^<(21)G^<(32)G^<(31)G^>(43)G^<(42)\\ &-\theta(12)\theta(43)G^<(21)G^<(32)G^<(31)G^<(43)G^<(42)\\ &-\theta(12)\theta(43)G^>(21)G^<(32)G^<(31)G^>(43)G^<(42)\\ &+\theta(12)\theta(43)G^>(21)G^<(32)G^<(31)G^<(43)G^<(42)\\ &\theta(12)\theta(13)G^<(21)G^t(32)G^<(31)G^<(43)G^<(42)\\ &-\theta(12)\theta(13)G^<(21)G^>(32)G^>(31)G^<(43)G^<(42)\\ &-\theta(12)\theta(13)G^>(21)G^<(32)G^<(31)G^<(43)G^<(42)\\ &+\theta(12)\theta(13)G^>(21)G^{\tilde{t}}(32)G^>(31)G^<(43)G^<(42)\Big).\end{aligned}$$

The time integration is

$$\begin{aligned}\Sigma^{<}_{a_2a_1}(t_4,t_1) = \int_{-\infty}^{\infty}\int_{-\infty}^{\infty} dt_2dt_3\big(&\quad G^{<}_{f_3f_4}(t_2,t_1)G^{R}_{b_1b_2}(t_3,t_2)G^{<}_{\alpha\alpha'}(t_3,t_1)G^{R}_{f_1f_2}(t_4,t_3)G^{>}_{\beta\beta'}(t_4,t_2) \\ &+ \quad G^{A}_{f_3f_4}(t_2,t_1)G^{<}_{b_1b_2}(t_3,t_2)G^{<}_{\alpha\alpha'}(t_3,t_1)G^{R}_{f_1f_2}(t_4,t_3)G^{<}_{\beta\beta'}(t_4,t_2) \\ &- \quad G^{A}_{f_3f_4}(t_2,t_1)G^{A}_{b_1b_2}(t_3,t_2)G^{>}_{\alpha\alpha'}(t_3,t_1)G^{<}_{f_1f_2}(t_4,t_3)G^{<}_{\beta\beta'}(t_4,t_2)\big).\end{aligned} \tag{85}$$

and in frequency space,

$$\begin{aligned}\Sigma^{<}_{a_2a_1}(\omega) = &\quad \int dyG^{>}_{\beta\beta'}(y)G^{R}_{f_1f_2}(\omega-y)\int dxG^{<}_{\alpha\alpha'}(x)G^{<}_{f_3f_4}(\omega-x)G^{R}_{b_1b_2}(\omega-x-y) \\ &+ \quad \int dyG^{<}_{\beta\beta'}(y)G^{R}_{f_1f_2}(\omega-y)\int dxG^{<}_{\alpha\alpha'}(x)G^{A}_{f_3f_4}(\omega-x)G^{<}_{b_1b_2}(\omega-x-y) \\ &+ \quad \int dyG^{<}_{\beta\beta'}(y)G^{<}_{f_1f_2}(\omega-y)\int dxG^{>}_{\alpha\alpha'}(x)G^{A}_{f_3f_4}(\omega-x)G^{A}_{b_1b_2}(\omega-x-y).\end{aligned} \tag{86}$$

5.6.2 Greater doubly-occupied pseudoparticle self-energy $\Sigma^{>}_{a_2a_1}(\omega)$

Follwing the same procedue,

$$\begin{aligned}\int_{-\infty}^{\infty}\int_{-\infty}^{\infty} d2d3\big(&\theta(12)\theta(13)G^{<}(21)G^{t}(32)G^{<}(31)G^{>}(43)G^{>}(42) \\ &-\theta(12)\theta(13)G^{<}(21)G^{>}(32)G^{>}(31)G^{>}(43)G^{>}(42) \\ &-\theta(12)\theta(13)G^{>}(21)G^{<}(32)G^{<}(31)G^{>}(43)G^{>}(42) \\ &+\theta(12)\theta(13)G^{>}(21)G^{\tilde{t}}(32)G^{>}(31)G^{>}(43)G^{>}(42) \\ &+\theta(12)\theta(43)G^{<}(21)G^{>}(32)G^{>}(31)G^{>}(43)G^{>}(42) \\ &-\theta(12)\theta(43)G^{>}(21)G^{>}(32)G^{>}(31)G^{<}(43)G^{>}(42) \\ &-\theta(12)\theta(43)G^{>}(21)G^{>}(32)G^{>}(31)G^{>}(43)G^{>}(42) \\ &+\theta(12)\theta(43)G^{>}(21)G^{>}(32)G^{>}(31)G^{<}(43)G^{>}(42) \\ &+\theta(42)\theta(13)G^{>}(21)G^{<}(32)G^{<}(31)G^{>}(43)G^{>}(42) \\ &-\theta(42)\theta(13)G^{>}(21)G^{<}(32)G^{>}(31)G^{>}(43)G^{>}(42) \\ &-\theta(42)\theta(13)G^{>}(21)G^{<}(32)G^{<}(31)G^{>}(43)G^{<}(42) \\ &+\theta(42)\theta(13)G^{>}(21)G^{<}(32)G^{>}(31)G^{>}(43)G^{<}(42) \\ &+\theta(42)\theta(43)G^{>}(21)G^{t}(32)G^{>}(31)G^{>}(43)G^{>}(42) \\ &-\theta(42)\theta(43)G^{>}(21)G^{>}(32)G^{>}(31)G^{<}(43)G^{>}(42) \\ &-\theta(42)\theta(43)G^{>}(21)G^{<}(32)G^{>}(31)G^{>}(43)G^{<}(42) \\ &+\theta(42)\theta(43)G^{>}(21)G^{\tilde{t}}(32)G^{>}(31)G^{<}(43)G^{<}(42)\big).\end{aligned}$$

The surviving terms are

$$\begin{aligned}\Sigma^{>}_{a_2a_1}(t_4,t_1) = \int_{-\infty}^{\infty}\int_{-\infty}^{\infty} dt_2dt_3\big(&\quad G^{A}_{f_3f_4}(t_2,t_1)G^{A}_{b_1b_2}(t_3,t_2)G^{>}_{\alpha\alpha'}(t_3,t_1)G^{>}_{f_1f_2}(t_4,t_3)G^{>}_{\beta\beta'}(t_4,t_2) \\ &+ \quad G^{A}_{f_3f_4}(t_2,t_1)G^{>}_{b_1b_2}(t_3,t_2)G^{>}_{\alpha\alpha'}(t_3,t_1)G^{R}_{f_1f_2}(t_4,t_3)G^{>}_{\beta\beta'}(t_4,t_2) \\ &+ \quad G^{>}_{f_3f_4}(t_2,t_1)G^{R}_{b_1b_2}(t_3,t_2)G^{>}_{\alpha\alpha'}(t_3,t_1)G^{R}_{f_1f_2}(t_4,t_3)G^{>}_{\beta\beta'}(t_4,t_2)\big).\end{aligned} \tag{87}$$

and in the frequency space,

$$\begin{aligned}\Sigma^{>}_{a_2a_1}(\omega) = & \int dyG^{>}_{\beta\beta'}(y)G^{>}_{f_1f_2}(\omega-y)\int dxG^{>}_{\alpha\alpha'}(x)G^{A}_{f_3f_4}(\omega-x)G^{A}_{b_1b_2}(\omega-x-y) \\ + & \int dyG^{>}_{\beta\beta'}(y)G^{R}_{f_1f_2}(\omega-y)\int dxG^{>}_{\alpha\alpha'}(x)G^{A}_{f_3f_4}(\omega-x)G^{>}_{b_1b_2}(\omega-x-y) \\ + & \int dyG^{>}_{\beta\beta'}(y)G^{R}_{f_1f_2}(\omega-y)\int dxG^{>}_{\alpha\alpha'}(x)G^{>}_{f_3f_4}(\omega-x)G^{R}_{b_1b_2}(\omega-x-y).\end{aligned} \tag{88}$$

5.7 The impurity spectral function $A^{imp}_{\beta'\beta}$

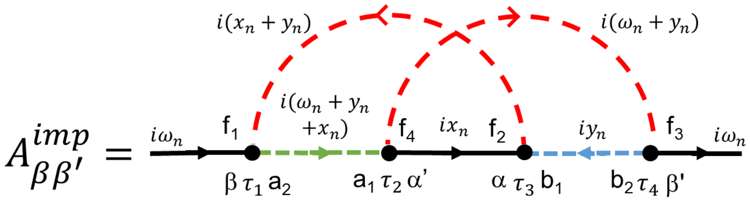

Figure 34: The Feynmann diagram of the impurity Green's function at OCA, where $i\omega_n$, ix_n, and iy_n are the matsubara frequency indices.

The final step is to calculate the physical impurity spectral function, $A_{imp}(\omega)$, which in turn allows us to calculate the steady state current through the impurity. The physical quantity in pseudo-particle approach should belong to $Q = 1$ space, *i.e.* $G^R, G^{<,>}$ *etc.* From the definition of retarded green's function,

$$G^R_{imp}(t) = i\theta(t)(G^>_{imp}(t) - G^<_{imp}(t)), \tag{89}$$

The important observation is that $\mathcal{G}$ satisfies the hermicity and time-reversal symmetry (Eq. 21) that Eq. (89) under Fourier transform becomes

$$A^{imp}(\omega) = \frac{i}{2\pi}\big(G^{imp,>}(\omega) - G^{imp,<}(\omega)\big). \tag{90}$$

Therefore we need to explicitly calculate the two correlation functions, $G^>_{imp}(\omega)$ and $G^<_{imp}(\omega)$.

5.7.1 Lesser impurity Green's function $G^{imp,<}_{\beta'\beta}(\omega)$

The real physical quantity $G^{imp,<}_{\beta'\beta}$ is $\sim O(e^{-\beta\lambda})$.

$$
\begin{aligned}
\int_{-\infty}^{\infty}\int_{-\infty}^{\infty} d2d3\big(&\theta(42)\theta(43)G^{<}(21)G^{t}(32)G^{>}(13)G^{<}(34)G^{>}(42)\\
&-\theta(42)\theta(43)G^{<}(21)G^{>}(32)G^{>}(13)G^{>}(34)G^{>}(42)\\
&-\theta(42)\theta(43)G^{<}(21)G^{<}(32)G^{>}(13)G^{<}(34)G^{<}(42)\\
&+\theta(42)\theta(43)G^{<}(21)G^{\tilde{t}}(32)G^{>}(13)G^{>}(34)G^{<}(42)\\
&+\theta(42)\theta(13)G^{<}(21)G^{>}(32)G^{>}(13)G^{>}(34)G^{>}(42)\\
&-\theta(42)\theta(13)G^{<}(21)G^{>}(32)G^{<}(13)G^{>}(34)G^{>}(42)\\
&-\theta(42)\theta(13)G^{<}(21)G^{>}(32)G^{>}(13)G^{>}(34)G^{<}(42)\\
&+\theta(42)\theta(13)G^{<}(21)G^{>}(32)G^{<}(13)G^{>}(34)G^{<}(42)\\
&+\theta(12)\theta(43)G^{<}(21)G^{<}(32)G^{>}(13)G^{<}(34)G^{<}(42)\\
&-\theta(12)\theta(43)G^{<}(21)G^{<}(32)G^{>}(13)G^{>}(34)G^{<}(42)\\
&-\theta(12)\theta(43)G^{>}(21)G^{<}(32)G^{>}(13)G^{<}(34)G^{<}(42)\\
&+\theta(12)\theta(43)G^{>}(21)G^{<}(32)G^{>}(13)G^{>}(34)G^{<}(42)\\
&+\theta(12)\theta(13)G^{<}(21)G^{t}(32)G^{>}(13)G^{>}(34)G^{<}(42)\\
&-\theta(12)\theta(13)G^{<}(21)G^{>}(32)G^{<}(13)G^{>}(34)G^{<}(42)\\
&-\theta(12)\theta(13)G^{>}(21)G^{<}(32)G^{>}(13)G^{>}(34)G^{<}(42)\\
&+\theta(12)\theta(13)G^{>}(21)G^{\tilde{t}}(32)G^{<}(13)G^{>}(34)G^{<}(42)\big).
\end{aligned}
$$

$$
\begin{aligned}
G^{imp,<}_{\beta'\beta}(t_4,t_1) = \int_{-\infty}^{\infty}\int_{-\infty}^{\infty} dt_2dt_3\big(\quad & G^{<}_{a_1a_2}(t_2,t_1)G^{>}_{\alpha\alpha'}(t_3,t_2)G^{>}_{f_1f_2}(t_1,t_3)G^{A}_{b_1b_2}(t_3,t_4)G^{R}_{f_3f_4}(t_4,t_2)\\
+ \quad & G^{<}_{a_1a_2}(t_2,t_1)G^{>}_{\alpha\alpha'}(t_3,t_2)G^{R}_{f_1f_2}(t_1,t_3)G^{>}_{b_1b_2}(t_3,t_4)G^{R}_{f_3f_4}(t_4,t_2)\\
+ \quad & G^{A}_{a_1a_2}(t_2,t_1)G^{<}_{\alpha\alpha'}(t_3,t_2)G^{>}_{f_1f_2}(t_1,t_3)G^{A}_{b_1b_2}(t_3,t_4)G^{<}_{f_3f_4}(t_4,t_2)\\
+ \quad & G^{A}_{a_1a_2}(t_2,t_1)G^{<}_{\alpha\alpha'}(t_3,t_2)G^{R}_{f_1f_2}(t_1,t_3)G^{>}_{b_1b_2}(t_3,t_4)G^{<}_{f_3f_4}(t_4,t_2)\big).
\end{aligned}
$$

and in the frequency space,

$$
\begin{aligned}
G^{imp,<}_{\beta'\beta}(\omega) = \quad & \int dy G^{A}_{b_1b_2}(y)G^{R}_{f_3f_4}(y+\omega)\int dx G^{>}_{\alpha\alpha'}(x)G^{>}_{f_1f_2}(x+y)G^{<}_{a_1a_2}(x+y+\omega)\\
+ \quad & \int dy G^{>}_{b_1b_2}(y)G^{R}_{f_3f_4}(y+\omega)\int dx G^{>}_{\alpha\alpha'}(x)G^{R}_{f_1f_2}(x+y)G^{<}_{a_1a_2}(x+y+\omega)\\
+ \quad & \int dy G^{A}_{b_1b_2}(y)G^{<}_{f_3f_4}(y+\omega)\int dx G^{<}_{\alpha\alpha'}(x)G^{>}_{f_1f_2}(x+y)G^{A}_{a_1a_2}(x+y+\omega)\\
+ \quad & \int dy G^{>}_{b_1b_2}(y)G^{<}_{f_3f_4}(y+\omega)\int dx G^{<}_{\alpha\alpha'}(x)G^{R}_{f_1f_2}(x+y)G^{A}_{a_1a_2}(x+y+\omega). \qquad (91)
\end{aligned}
$$

5.7.2 Greater impurity Green's function $G^{imp,>}_{\beta'\beta}(\omega)$

The real physical quantity $G^{imp,>}_{\beta'\beta}$ is $\sim O(e^{-\beta\lambda})$.

$$
\begin{aligned}
\int_{-\infty}^{\infty}\int_{-\infty}^{\infty} d2d3\big(&\theta(12)\theta(13)G^{<}(21)G^{t}(32)G^{>}(13)G^{<}(34)G^{>}(42)\\
&-\theta(12)\theta(13)G^{<}(21)G^{>}(32)G^{<}(13)G^{<}(34)G^{>}(42)\\
&-\theta(12)\theta(13)G^{>}(21)G^{<}(32)G^{>}(13)G^{<}(34)G^{>}(42)\\
&+\theta(12)\theta(13)G^{>}(21)G^{\tilde{t}}(32)G^{<}(13)G^{<}(34)G^{>}(42)\\
&+\theta(12)\theta(43)G^{<}(21)G^{>}(32)G^{<}(13)G^{<}(34)G^{>}(42)\\
&-\theta(12)\theta(43)G^{<}(21)G^{>}(32)G^{<}(13)G^{>}(34)G^{>}(42)\\
&-\theta(12)\theta(43)G^{>}(21)G^{>}(32)G^{<}(13)G^{<}(34)G^{>}(42)\\
&+\theta(12)\theta(43)G^{>}(21)G^{>}(32)G^{<}(13)G^{>}(34)G^{>}(42)\\
&+\theta(42)\theta(13)G^{>}(21)G^{<}(32)G^{>}(13)G^{<}(34)G^{>}(42)\\
&-\theta(42)\theta(13)G^{>}(21)G^{<}(32)G^{<}(13)G^{<}(34)G^{>}(42)\\
&-\theta(42)\theta(13)G^{>}(21)G^{<}(32)G^{>}(13)G^{<}(34)G^{<}(42)\\
&+\theta(42)\theta(13)G^{>}(21)G^{<}(32)G^{<}(13)G^{<}(34)G^{<}(42)\\
&+\theta(42)\theta(43)G^{>}(21)G^{t}(32)G^{<}(13)G^{<}(34)G^{>}(42)\\
&-\theta(42)\theta(43)G^{>}(21)G^{>}(32)G^{<}(13)G^{>}(34)G^{>}(42)\\
&-\theta(42)\theta(43)G^{>}(21)G^{<}(32)G^{<}(13)G^{<}(34)G^{<}(42)\\
&+\theta(42)\theta(43)G^{>}(21)G^{\tilde{t}}(32)G^{<}(13)G^{>}(34)G^{<}(42)\big).
\end{aligned}
$$

only surviving terms are

$$
\begin{aligned}
G^{imp,>}_{\beta'\beta}(t_4,t_1)=\int_{-\infty}^{\infty}\int_{-\infty}^{\infty} dt_2dt_3\big(\quad & G^{A}_{a_1a_2}(t_2,t_1)G^{<}_{\alpha\alpha'}(t_3,t_2)G^{R}_{f_1f_2}(t_1,t_3)G^{<}_{b_1b_2}(t_3,t_4)G^{>}_{f_3f_4}(t_4,t_2)\\
+\quad & G^{A}_{a_1a_2}(t_2,t_1)G^{>}_{\alpha\alpha'}(t_3,t_2)G^{<}_{f_1f_2}(t_1,t_3)G^{A}_{b_1b_2}(t_3,t_4)G^{>}_{f_3f_4}(t_4,t_2)\\
+\quad & G^{>}_{a_1a_2}(t_2,t_1)G^{<}_{\alpha\alpha'}(t_3,t_2)G^{R}_{f_1f_2}(t_1,t_3)G^{<}_{b_1b_2}(t_3,t_4)G^{R}_{f_3f_4}(t_4,t_2)\\
+\quad & G^{>}_{a_1a_2}(t_2,t_1)G^{>}_{\alpha\alpha'}(t_3,t_2)G^{<}_{f_1f_2}(t_1,t_3)G^{A}_{b_1b_2}(t_3,t_4)G^{R}_{f_3f_4}(t_4,t_2)\big).
\end{aligned}
$$

and in frequency space,

$$
\begin{aligned}
G^{imp,>}_{\beta'\beta}(\omega)=\; & \int dyG^{<}_{b_1b_2}(y)G^{>}_{f_3f_4}(y+\omega)\int dxG^{<}_{\alpha\alpha'}(x)G^{R}_{f_1f_2}(x+y)G^{A}_{a_1a_2}(x+y+\omega)\\
+\; & \int dyG^{A}_{b_1b_2}(y)G^{>}_{f_3f_4}(y+\omega)\int dxG^{>}_{\alpha\alpha'}(x)G^{<}_{f_1f_2}(x+y)G^{A}_{a_1a_2}(x+y+\omega)\\
+\; & \int dyG^{<}_{b_1b_2}(y)G^{R}_{f_3f_4}(y+\omega)\int dxG^{<}_{\alpha\alpha'}(x)G^{R}_{f_1f_2}(x+y)G^{>}_{a_1a_2}(x+y+\omega)\\
+\; & \int dyG^{A}_{b_1b_2}(y)G^{R}_{f_3f_4}(y+\omega)\int dxG^{>}_{\alpha\alpha'}(x)G^{<}_{f_1f_2}(x+y)G^{>}_{a_1a_2}(x+y+\omega). \qquad (92)
\end{aligned}
$$

Therefore, now we are able to calculate the impurity spectrum $A^{imp}(\omega)=-\frac{1}{\pi}Im(G^{imp}(\omega))$:

$$
A^{imp}(\omega)=\frac{i}{2\pi}\big(G^{imp,>}_{\beta'\beta}(\omega)-G^{imp,<}_{\beta'\beta}(\omega)\big). \qquad (93)
$$

5.8 Correspondence between equilibrium and non-equilibrium solution at the equilibrium limit

Here, the correspondence between the equilibrium OCA solution and the nonequilibriunm derivation is provided using the fluctuation-dissipation relation (Eq. 31), which is the analytic relation between equilibrium response ($\mathcal{G}^{R,A}$) and correlation functions ($\mathcal{G}^{>,<}$) (Eq. 18 and Table 4). We present the rigorous proof of several examples of the empty bosonic $\Sigma^{>,<}_{b_2b_1}(\omega)$, singly-occupied fermionic $\Sigma^{>,<}_{f_2f_1}(\omega)$, doubly-occupied bosonic $\Sigma^{>,<}_{a_2a_1}(\omega)$, and the impurity Green's function $G^{>,<}_{imp}(\omega)$. This proof validates that our derivation is the true solution of the nonequilibrium Anderson impurity model, which includes the vertex terms (or one-crossing terms) on the Keldysh contour in the real frequency domain.

Table 4: The analytic relation between the response and correlation functions in the equilibrium where $f_{FD}(\omega)(f_{FD}(-\omega))$ is the Fermi-Dirac distribution function.

Pseudo-particle	Physical
$G^<_{f(b)}(\omega) = \pm 2ie^{-\beta\omega} ImG^R_{f(b)}(\omega)$	$G^<_\alpha(\omega) = -i/\pi f_{FD}(\omega) ImG_\alpha(\omega)$
$G^>_{f(b)}(\omega) = 2iImG^R_{f(b)}(\omega)$	$G^>_\alpha(\omega) = i/\pi f_{FD}(-\omega) ImG_\alpha(\omega)$

5.8.1 Correspondence of pseudo-particle self-energy

Because, for the pseudo-particle self-energies (Eq. 72, 74, 79, 81, 86, 88), only the hybridization terms change, the proof for a single type is sufficient for the proof of the whole pseudo-particle self-energies. We choose, therefore, the empty bosonic self-energy. The imaginary part of empty bosonic $\Sigma^R_{b_2b_1}(\omega)$ in the equilibrium is the sum of 4 terms (Eq. 94).[8]

$$\begin{aligned} Im[\Sigma^R_{b_2b_1}(\omega)] = & \int dy f(y) A_{\beta\beta'}(y) \int dx f(x) A_{\alpha\alpha'}(x) \times \\ & \big([Im[G^R_{f_3f_4}(y+\omega)]Re[G^R_{f_1f_2}(x+\omega)]Re[G^R_{a_1a_2}(x+y+\omega)] \\ + & [Re[G^R_{f_3f_4}(y+\omega)]Im[G^R_{f_1f_2}(x+\omega)]Re[G^R_{a_1a_2}(x+y+\omega)] \\ + & [Re[G^R_{f_3f_4}(y+\omega)]Re[G^R_{f_1f_2}(x+\omega)]Im[G^R_{a_1a_2}(x+y+\omega)] \\ - & [Im[G^R_{f_3f_4}(y+\omega)]Im[G^R_{f_1f_2}(x+\omega)]Im[G^R_{a_1a_2}(x+y+\omega)]\big). \end{aligned} \tag{94}$$

Upon the substitution $\Sigma^{<}_{b_2b_1}(\omega) \rightarrow -2ie^{-\beta\omega}Im[G^R_{b_2b_1}(\omega)]$ (in the equilibrium limit) (Table 4),

$$\begin{aligned}
&\int dy - f(y)\Delta_{\beta\beta'}(y)G^R_{f_3f_4}(y+\omega)\int dxf(-x)\Delta_{\alpha\alpha'}(x)2ie^{-\beta(x+\omega)}ImG^R_{f_1f_2}(x+\omega)G^R_{a_1a_2}(x+y+\omega)\\
&+\int dyf(-y)\Delta_{\beta\beta'}(y)G^R_{f_3f_4}(y+\omega)\int dxf(-x)\Delta_{\alpha\alpha'}(x)G^A_{f_1f_2}(x+\omega)-2ie^{-\beta(x+y+\omega)}Im[G^R_{a_1a_2}(x+y+\omega)]\\
&+\int dyf(-y)\Delta_{\beta\beta'}(y)2ie^{-\beta(y+\omega)}ImG_{f_3f_4}(y+\omega)\int dx - f(x)\Delta_{\alpha\alpha'}(x)G^A_{f_1f_2}(x+\omega)G^A_{a_1a_2}(x+y+\omega)\\
&= -2ie^{-\beta\omega}\int dyf(y)\Delta_{\beta\beta'}(y)G^R_{f_3f_4}(y+\omega)\int dxf(x)\Delta_{\alpha\alpha'}(x)ImG^R_{f_1f_2}(x+\omega)G^R_{a_1a_2}(x+y+\omega)\\
&-2ie^{-\beta\omega}\int dyf(y)\Delta_{\beta\beta'}(y)G^R_{f_3f_4}(y+\omega)\int dxf(x)\Delta_{\alpha\alpha'}(x)G^A_{f_1f_2}(x+\omega)Im[G^R_{a_1a_2}(x+y+\omega)]\\
&-2ie^{-\beta\omega}\int dyf(y)\Delta_{\beta\beta'}(y)ImG_{f_3f_4}(y+\omega)\int dxf(x)\Delta_{\alpha\alpha'}(x)G^A_{f_1f_2}(x+\omega)G^A_{a_1a_2}(x+y+\omega),
\end{aligned} \tag{95}$$

where $\Delta_{\alpha\alpha'}(\omega) = -\frac{i}{\pi}\text{Im}[G_{\alpha\alpha'}(\omega)]$, $\mathcal{G}^R_{\alpha\beta} = \mathcal{G}^{A*}_{\beta\alpha}$, and $f(-\omega) = e^{\beta\omega}f(\omega)$. A further expansion of Eq. (95) eliminates the imaginary terms and leads the exact match to the equilibrium solution Eq. (94). This correspondence is also observed for the empty bosonic $\Sigma^{>}_{b_2b_1}(\omega) \rightarrow 2iIm[\Sigma^R_{b_2b_1}(\omega)]$. Basically the same procedure is applied to the rest of pseudo-particle self-energies: $\Sigma^{>,<}_{f_2f_1}(\omega)$ and doubly occupied bosonic $\Sigma^{>,<}_{a_2a_1}(\omega)$.

5.8.2 Correspondence of impurity Green's function

An explicit form of the imaginary part of impurity Green's function $Im[G^{imp}_{\beta'\beta}(\omega)]$ is [8]

$$\begin{aligned}
\text{Im}[G^{imp}_{\beta'\beta}(\omega)] \propto \int dye^{-\beta y}\int dxf(x) \quad &\Delta_{\alpha\alpha'}(x)Im[G^R_{b_1b_2}(y)G^R_{f_1f_2}(x+y)]\\
&\times Im[G^R_{f_3f_4}(y+\omega)G^R_{a_1a_2}(x+y+\omega)]
\end{aligned} \tag{96}$$

$$\begin{aligned}
\text{Im}[G^{imp}_{\beta'\beta}(\omega)] = \frac{1}{e^{\beta\lambda<Q>}f(-\omega)}&\int dye^{-\beta y}\int dxf(x)\Delta_{\alpha\alpha'}(x)\\
\big(ReG^R_{b_1b_2}(y)ImG^R_{f_1f_2}(x+y)]&ReG^R_{f_3f_4}(y+\omega)ImG^R_{a_1a_2}(x+y+\omega)\\
+ReG^R_{b_1b_2}(y)ImG^R_{f_1f_2}(x+y)]&ImG^R_{f_3f_4}(y+\omega)ReG^R_{a_1a_2}(x+y+\omega)\\
+ImG^R_{b_1b_2}(y)ReG^R_{f_1f_2}(x+y)]&ReG^R_{f_3f_4}(y+\omega)ImG^R_{a_1a_2}(x+y+\omega)\\
+ImG^R_{b_1b_2}(y)ReG^R_{f_1f_2}(x+y)]&ImG^R_{f_3f_4}(y+\omega)ReG^R_{a_1a_2}(x+y+\omega)\big).
\end{aligned} \tag{97}$$

Surprisingly enough, applying the fluctuation-dissipation relation to nonequilibrium $G^{imp,<}_{\beta'\beta}(\omega) \rightarrow if(\omega)A_\alpha(\omega)$ and $G^{imp,>}_{\beta'\beta}(\omega) \rightarrow -if(-\omega)A_\alpha(\omega)$ gives rise to the exact match to the equilibrium solution of Eq (96). In conclusion, the whole derivation of Anderson impurity model on Keldysh contour up to OCA has been proved.

5.9 Conclusion

We derived the complete real frequency integral equation for the steady state nonequilibrium Anderson impurity model (AIM) on the Keldysh contour up to the one-crossing approximation (OCA) which includes the vertex diagrams. Because previous studies had been limited to the real-time propagation of the Green's function, the investigation for the low energy regime of the Kondo temperature ($\sim T_K$) was not possible. This is due to the complex nature of the nonequilibrium quantum field theory particularly concerning the high order perturbation diagramms. Now, because the real frequency OCA solution of nonequiblirum AIM is available, the low energy spectrum of the impurity is accesible with high precision through our derivation.[10] Therefore, the future work will be the numerical implementation of the derivation for the model study and for the real system.

Bibliography

[1] Gell-Mann, M.; Low, F. Bound States in Quantum Field Theory. *Phys. Rev.* **1951**, *84*, 350–354.

[2] Feynman, R. P. Space-Time Approach to Quantum Electrodynamics. *Phys. Rev.* **1949**, *76*, 769–789.

[3] Keldysh, L. V. Diagram Technique for Nonequilibrium Processes. *Soviet Phys. JETP* **1965**, *20*, 1018–1026.

[4] Kotliar, G.; Savrasov, S. Y.; Haule, K.; Oudovenko, V. S.; Parcollet, O.; Marianetti, C. A. Electronic Structure Calculations with Dynamical Mean-Field Theory. *Rev. Mod. Phys.* **2006**, *78*, 865–951.

[5] Wingreen, N. S.; Meir, Y. Anderson Model Out of Equilibrium: Noncrossing-Approximation Approach to Transport Through a Quantum Dot. *Phys. Rev. B* **1994**, *49*, 11040–11052.

[6] Coleman, P. New Approach to the Mixed-Valence Problem. *Phys. Rev. B* **1984**, *29*, 3035–3044.

[7] Hettler, M. H.; Kroha, J.; Hershfield, S. Nonequilibrium Dynamics of the Anderson Impurity Model. *Phys. Rev. B* **1998**, *58*, 5649–5664.

[8] Haule, K.; Yee, C.-h.; Kim, K. Dynamical Mean-Field Theory within the Full-Potential Methods: Electronic Structure of $\mathrm{CeIrIn_5}$, $\mathrm{CeCoIn_5}$, and $\mathrm{CeRhIn_5}$. **2010**, 1–30.

[9] Antipov, A. E.; Dong, Q.; Gull, E. Voltage Quench Dynamics of a Kondo System. **2016**, *036801*, 1–6.

[10] Myung, C. W.; Haule, K.; Lee, G.; Kim, K. S. Nonequilibrium Anderson Impurity Model on Keldysh Contour : One-Crossing Approximation. **2018**, (in press).

Acknowledgements

물심양면으로 격려와 지도, 충고와 지원을 아낌없이 해주신 지도교수 김광수 교수님께 깊은 감사를 드립니다. 교수님의 전격적인 지원과 동기부여 덕분에 보람찬 박사학위 과정을 보낼 수 있었습니다. 한결같이 연구에 매진하는 열정과 학문을 향한 끊임없는 도전은 저에게 큰 귀감이 됩니다. `awk`부터 many-body theory까지 필요한 모든 것을 가르쳐주시고 여러 호의를 베풀어 주신 이근식 교수님께 감사를 드립니다. 교수님의 one-to-one 과외 덕분에 정말 많은 것을 배웠습니다. 논문 심사위원으로 참여해주신 민승규 교수님, 물리학과 박노정 교수님, 에너지 공학과 이준희 교수님께 감사의 말씀을 드립니다. I thank Prof. Kristjan Haule for allowing me to visit the group, teaching me details of his impurity solver code, and giving me advices and comments.

2007년 봄 포항에서 시작한 여정이 이리도 돌고돌아 울산에서 매듭짓게 되었습니다. 어쩌면 금방 올 수도 있는 길을 너무 멀리 돌아왔는지 모르겠습니다. 대학원 덕분에 Dunning-Kruger 효과를 절실히 체험했습니다. 제 지식의 수준과 능력의 부족함을 여실히 느끼는 나날들이었습니다.

박사과정 동안 세세하게 가르쳐주고 도와주었던 윤정훈 형과 조우종 이 두 사람에게 특별히 감사한 마음을 전합니다. 두 사람 덕분에 많은 것을 배웠습니다. 또한 윤일승 형, 최성수 형, 유성욱, 이다니엘 형, 이정우 형, Dr. Mohadmed Reza Rezapour, 박영신 박사님, 백승빈 박사님, Dr. Saqib Javaid, Dr. Atanu Jana, Dr. Nannan Li, Dr. Lihua Wang, 이왕근 형, 윤태승, Teymourloei Amir Hajibabei, Saeed Pourasad, 김동연, 하미란, 나영훈, 김준우, 정다솔, Ba qian kai을 포함한 CSM 멤버 모두에게 감사의 말씀을 전합니다. 연구실에서 함께 동고동락하며 의지할 수 있고 같이 고민할 수 있어서 행복한 시간이었습니다. 특히, 아직 학위과정을 밟고 있는 이들에겐 건승을 빕니다.

무엇보다 저를 양육하며 평생을 헌신하신 어머니와 아버지, 누구보다 이 논문을 기다렸을 할아버지와 동생 철우 그리고 가족 모두에게 이 논문을 바칩니다. 김재형 목사님을 비롯한 울산 주나래 교회 식구들에게도 깊은 감사의 말씀을 드립니다. 못난 남편을 만나 매일밤 홀로 잠드는 사랑하는 주현에게 심심한 사과와 애정을 담아 보냅니다. 주현이의 인내와 배려 그리고 이해와 섬김이 있었기에 어려운 박사과정 기간을 견뎌낼 수 있었습니다.

지존자의 은밀한 곳에 거주하며
전능자의 그늘 아래에 사는 자여,
나는 여호와를 향하여 말하기를
그는 나의 피난처요 나의 요새요
내가 의뢰하는 하나님이라 하리니.
(시편 91:1-2)

박사로서 부끄럽지 않게 학자의 혀와 학자의 귀를 구하며 겸손히 살아가도록 노력하겠습니다. 마지막으로 지혜와 지식의 근본이요 아둔한 인생의 선한 목자되신 하나님께 감사드립니다.

"I believe with the Westminster Divines
and their predecessors *ad Infinitum*
That "Man's chief end is to glorify God
and to enjoy Him for ever."
That for this end to every man has been given
a progressively increasing power
of communication with other creatures.
That with his powers his susceptibilities increase.
That happiness and misery must inevitably increase
with increasing power and knowledge.
But the subject is too high.
I will not, however, stop short,
but proceed to intellectual pursuits."

– Maxwell, James Clerk (1851) *The Life of James Clerk Maxwell*

"If I have been enticed into brashness
by the wonderful beauty of your works,
or if I have loved my own glory among men,
while advancing in work destined for your glory,
gently and mercifully pardon me;
and finally, deign graciously to cause
that these demonstrations may lead to your glory
and to the salvation of souls,
and nowhere be an obstacle to that. Amen."

– Kepler, Johannes (1619) *The Harmony of the World*

Curriculum Vitae

CHANG WOO MYUNG (명창우)
cwmyung@unist.ac.kr
chang.w.myung@gmail.com

EDUCATION

Ph.D. Sep. 2014 - Feb. 2019 Physical Chemistry, Ulsan National Institute of Science and Technology (UNIST), Ulsan, Korea.

M.S. Sep. 2012 - Aug. 2014 Pohang University of Science and Technology (POSTECH), Pohang, Korea.

B.S. Mar. 2007 - Aug. 2012 Pohang University of Science and Technology (POSTECH), Pohang, Korea.

PUBLICATIONS

1. Myung, C. W.; Ha, M.; Kim, D. Y.; Rehr, J. J.; Kim, K. S. Theoretical Study of X-ray Absorption Spectroscopy of Heterogeneous Single Atom Catalysts. **2018** (in preparation).

2. Park, Y.;* Jana, A.;* Myung, C. W. ;* Yoon, T. S.; Puchtler, T. J.; Kocher, C. C.; Taylor, R. A.; Kim, K. S. (*equally contributed). Large Enhancement of Optical Quantum Efficiency of MAPbBr$_3$ by Encapsulating Graphene. **2018** (under review).

3. Jana, A.; Myung, C. W.; Kim, K. S. Multiphoton Absorption and Multiexciton Generation in Zero-Dimensional Bulk Material. *Sci. Adv.* **2018** (under review).

4. Myung, C. W., Haule, K.; Lee, G.; Kim, K. S. Nonequilibrium Anderson Impurity Model on Keldysh Contour: One-Crossing Approximation. **2018** (in preparation).

5. Myung, C. W.; Lee, G.; Kim, K. S. Chalcogenide Dependent Vibrational Screening of Exciton in Cu$_2$ZnSnX$_4$ (X=S, Se) Kesterite Solar Cells. **2018** (to be submitted).

6. Myung, C. W.; Lee, G.; Kim, K. S. La-Doped BaSnO$_3$ Electron Transport Layer for Perovskite Solar Cells. *J. Mater. Chem. A* **2018**, *6*, 23071–23077.

7. Yoon, T.;* Kim, G.-H.;* Myung, C. W.;* Kajal, S.; Jeong, J.; Kim, J. W.; Kim, J. Y.; Kim, K. S. (*equally contributed) Ambient-Stable Cubic-Phase Hybrid Perovskite Reaching the Shockley–Queisser Fill Factor Limit via Inorganic Additive-Assisted Process. *ACS Appl. Energy Mater.* **2018**, *1*, 5865.

8. Javaid, S.; Myung, C. W.; Pourasad, S.; Rakshit, B.; Kim, K. S.; Lee, G. A Highly Hydrophobic Fluorographene-Based System as an Interlayer for Electron Transport in Organic-Inorganic Perovskite Solar Cells. *J. Mater. Chem. A* **2018**, *6 (38)*, 18635–18640.

9. Myung, C. W.; Javaid, S.; Kim, K. S.; Lee, G. Rashba-Dresselhaus Effect in Inorganic/Organic Lead Iodide Perovskite Interfaces. *ACS Energy Lett.* **2018**, *3*, 12941300.

10. Tiwari, J. N.; Sultan, S.; Myung, C. W.; Yoon, T.; Li, N.; Ha, M.; Harzandi, A. M.; Park, H. J.; Kim, D. Y.; Chandrasekaran, S. S.; Lee, W. G.; Vij, V.; Kang, H.; Shin, T. J.; Shin, H. S.; Lee, G.; Lee, Z.; Kim, K. S. Multicomponent Electrocatalyst with Ultralow Pt Loading and High Hydrogen Evolution Activity. *Nat. Energy* **2018**, *3 (9)*, 773–782.

11. Myung, C. W.; Yun, J.; Lee, G.; Kim, K. S. A New Perspective on the Role of A-Site Cations in Perovskite Solar Cells. *Adv. Energy Mater.* **2018**, *8 (14)*, 1–7 (inside front cover).

12. Javaid, S.;* Myung, C. W.;* Yun, J.; Lee, G.; Kim, K. S. (*equally contributed) Organic Cation Steered Interfacial Electron Transfer within Organic-Inorganic Perovskite Solar Cells. *J. Mater. Chem. A* 2018, *6 (10)*, 4305–4312 (back cover).

13. Park, B.; Kim, K.; Park, J.; Lim, H.; Lanh, P. T.; Jang, A. R.; Hyun, C.; Myung, C. W.; Park, S.; Kim, J. W.; Kim, K. S.; Shin, H. S.; Lee, G.; Kim, S. H.; Park, C. E.; Kim, J. K. Anomalous Ambipolar Transport of Organic Semiconducting Crystals via Control of Molecular Packing Structures. *ACS Appl. Mater. Interfaces* **2017**, *9 (33)*, 27839–27846.

14. Rezapour, M. R.;* Myung, C. W.;* Yun, J.; Ghassami, A.; Li, N.; Yu, S. U.; Hajibabaei, A.; Park, Y.; Kim, K. S. (*equally contributed) Graphene and Graphene Analogs toward Optical, Electronic, Spintronic, Green-Chemical, Energy-Material, Sensing, and Medical Applications. *ACS Appl. Mater. Interfaces* **2017**, *9 (29)*, 24393–24406.

15. Park, Y.;*, Kim, Y. S.;*, Myung, C. W.;*, Taylor, R. A.; Chan, C. C. S.; Reid, B. P. L.; Puchtler,T. J.; Nicholas, R. J.; Singh, L. T.; Lee, G.; Hwang, C.-C.; Park, C.-Y.; Kim, K. S. (*equally contributed), Two-Dimensional Excitonic Photoluminescence in Graphene on a Cu Surface. *ACS Nano*, **2017**, *11*, 3207-3212.

16. Hyun, C.; Yun, J.; Cho, W. J.; Myung, C. W., Park, J.; Lee, G.; Lee, Z.; Kim, K.; Kim, K. S. Graphene Edges and Beyond: Temperature-Driven Structures and Electromagnetic Properties. *ACS Nano*, **2015**, *9*, 4669-4674.